THE UTILITY OF SYNTHETIC APERTURE RADAR (SAR) INTERFEROMETRY IN MONITORING SINKHOLE SUBSIDENCE

By

Rana Abdulla Al-Fares

A Dissertation Presented to the
FACULTY OF THE GRADUATE SCHOOL
UNIVERSITY OF SOUTHERN CALIFORNIA
In Partial Fulfillment of the
Requirements for the Degree
DOCTOR OF PHILOSOPHY
(CIVIL ENGINEERING)

May 2004

INFORMATION TO USERS

The quality of this reproduction is dependent upon the quality of the copy submitted. Broken or indistinct print, colored or poor quality illustrations and photographs, print bleed-through, substandard margins, and improper alignment can adversely affect reproduction.

In the unlikely event that the author did not send a complete manuscript and there are missing pages, these will be noted. Also, if unauthorized copyright material had to be removed, a note will indicate the deletion.

ProQuest Information and Learning Company
300 North Zeeb Road
P.O. Box 1346
Ann Arbor, MI 48106-1346

Dedication

To my parents whom continuously surrounded me with love and pervasive encouragement

To my siblings whom provided constant support and unwavering confidence

To my friends whom infinitely supported me and stood by me in spite of all the difficulties

Acknowledgments

I would like to offer my deepest gratitude to the creator of heaven and earth, God all mighty, the most gracious, the most merciful for providing me with the strength and will to undertake this task.

I would like to express my deepest appreciation and profound gratitude to my academic advisor and dissertation committee chair, Dr. Jean-Pierre Bardet, for his support, advice, and patience throughout the course of this research and my graduate studies at University of Southern California.

I would also like to offer my humble thanks to Dr. Susan Owen, from the Earth Science department at USC, for her valuable consultation during the course of this research dedicating long hours in spite of her busy schedule. Professor Owen was also kind to provide me with the raw SAR data of the Grabens region of Canyonlands National Park used in the interferogram example discussed in chapter 4 of this study and gave me the permission to use the earth science network to do the processing needed using ROI_PAC, an interferometric software developed by JPL and installed on the Earth Science Department machines.

I am also grateful to Mr. Scott Marsic, a graduate student in the Earth Science Department, whom was very patient and helpful in providing me with instructions and guided me through the process of generating an interferogram.

I would also like to extend my sincere gratitude to other members of my advisory committee, Dr. Carter Wellford, Dr. George Chillingarian and Dr. Geoffrey Martin for their valuable time, active discussion and helpful suggestions.

I would specially like to express my deepest appreciation to Mrs. Nora Wiik, at the European Space Agency, and Mrs. Marina Iadicola at Eurimage Inc., for their helpful suggestions and patience during data ordering stage.

I would like to acknowledge Kuwait University, for giving me the opportunity to pursue my graduate studies and funding the case study illustrated in chapter 7 of this dissertation.

Finally, very special thanks go to my family and friends whom continues support and faith in me kept my determination going.

Table of Contents

List of Tables

List of Figures

Abstract

Synthetic Aperture Radar (SAR) interferometry, a newly progressed technique capable of detecting very small ground surface elevation changes, is proposed to detect and monitor sinkholes subsidence susceptibility over large Karstic areas. This technique, which was proposed by researchers in the area of geophysical studies in 1989, uses (SAR) images to measure very small (1cm or less) surface motion over large areas with good spatial resolution (tens of meters). The advanced method has been used in the studies of earthquakes and other natural phenomenon and has shown promising results.

The effectiveness of the remotely sensed technique in determining the damage caused by sinkholes is assessed by using a simplified model approximated by the normal probability (Gaussian) distribution theory proposed by researchers in 1969 to study the mechanism of the resulting ground surface subsidence, estimate the order of magnitude of such settlement and finally determine whether these settlements are sufficiently large to be detected by InSAR.

A specific purpose database, including both collapse and subsidence sinkholes, was developed to store and organize all the important information relative to different case histories. This information was used to further investigate the relevance of SAR interferometry in studying the phenomenon.

The relevance of the proposed technique was further investigated by utilizing three European Remote Sensing (ERS) Synthetic Aperture Radar (SAR) images encompassing an almost 5-year period of observation (1992-1997), three successful

interferograms with short perpendicular baseline (<100 meters) from a descending orbital trajectory have been produced. Analysis of these interferograms indicate a relative regional subsidence of up to 0.5 cm/year within the Devil's Throat Sinkhole area, located in the Gold Butte district of Clark County in the Southeast corner of Nevada. Observations of deformation along profiles constructed on the produced interferograms also show a steep gradient in displacement rates occurring very close to the area where the Devil's Throat Sinkhole exists.

The demonstration of the technique in the Devil's Throat area, applied using data from the European Space Agency's ERS systems, has shown promising and unique results. These results demonstrate the effectiveness of the technique in studying small-scale ground deformations over large Karstic areas.

1. Introduction

1.1. Research background

Karst, a distinctive topography in which the landscape is largely shaped by the dissolving action of water on Carbonate bedrock surfaces, primarily limestone and dolomite, and occurring over many thousands of years results in unusual surface and subsurface features (see Figures 1.1 and 1.2). Karst topography is usually irregular due to the solution activity of acidic surface and groundwater, which dissolve the carbonate rocks forming cavities and allowing surficial sediments to collapse or subside (Lane, 1986).

Sinkholes, the most common and most easily recognized surface features of Karst topography, are defined as or generally refer to an area of localized land surface subsidence or collapse, due to Karst processes, which result in a closed hollow of moderated dimensions (Beck, 1984). Collapse could occur in bedrock or in the material overlaying the bedrock and can be divided into two different categories depending on the causes of occurrence. Induced sinkholes are those sinkholes caused or accelerated by human activities such as pumpage from wells, irrigation, excavating, dewatering, blasting, or even weight of building. Whereas natural sinkholes are those caused by nature, for example rainfall, where CO_2 in the atmosphere is dissolved in rainwater forming Carbonic acid. The formed Carbonic acid hits the ground exploiting cracks or crevices in the rock over long periods of time dissolving the bedrock and forming cavities, which lead to either sediment collapse or subsidence.

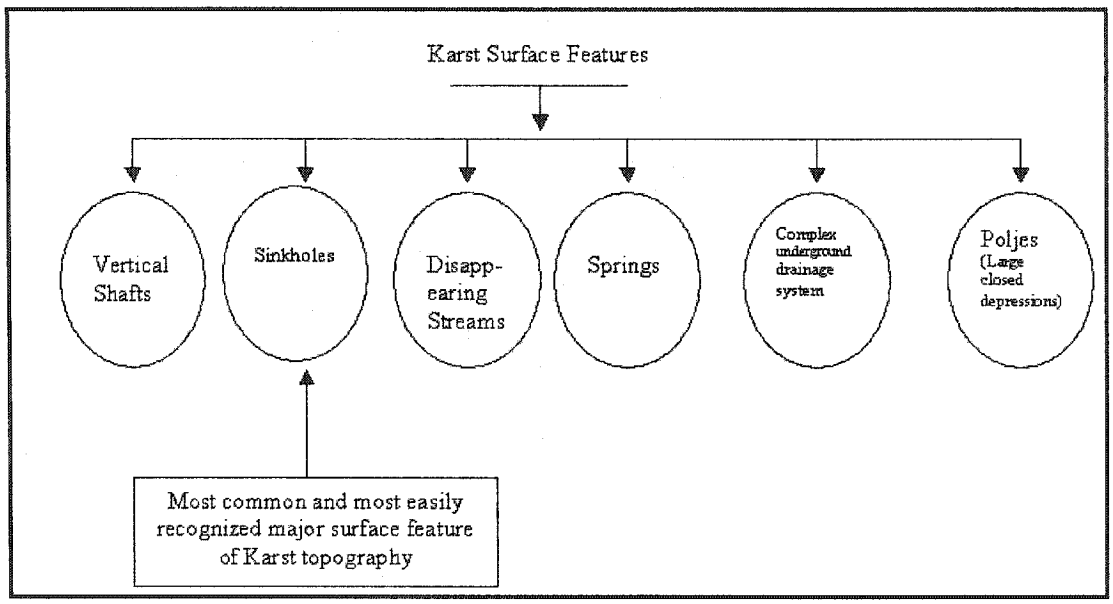

Figure 1.1: Surface landforms in Karst regions

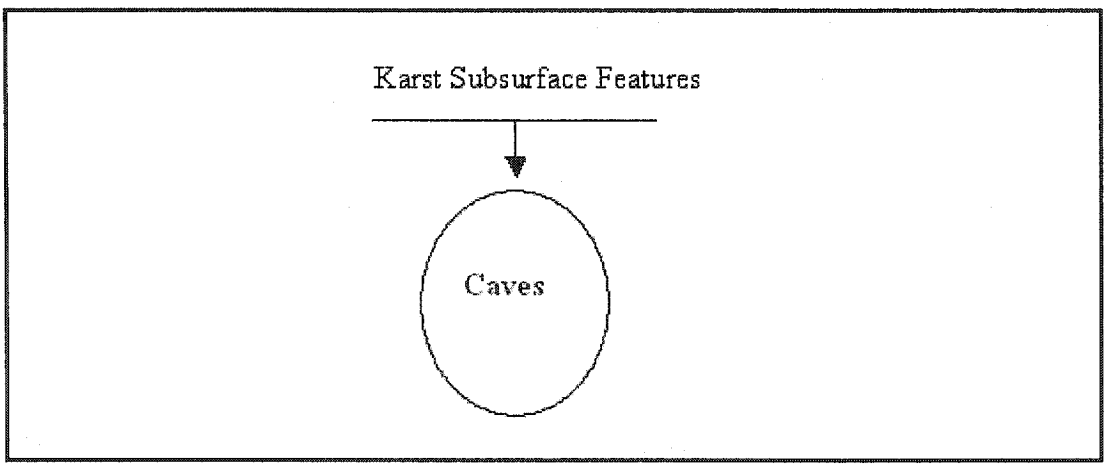

Figure 1.2: Subsurface landforms in Karst regions

Sinkholes are usually accompanied by noticeable signs such as slumping or sagging, structural failure as in Figure 1.3, ponding as in Figure 1.4, vegetation stress and turbidity in well water leading to its contamination. The instability of Karst has caused great damage to roads, buildings, airports and lifelines all over the world and is responsible for millions of dollars of damage to public and private property every year. Sinkholes in particular are continuously unstable, unexpected and are commonly accompanied with not only significant property and environmental damage but also pose a serious threat to human lives. Large and even deadly sinkholes have been reported in different parts of the world (see for example Al-Rifaiy (1990); Jammal (1994); Hollingshead (1984); Shouyue (1984); Brink (1984); and Swanson and Larson (2000)). Newton (1987) reported that the cost of damage and measures to protect structures against additional or potential sinkhole collapse has been significant and that costs reported for a limited number of sites between 1971 and 1980 in the United States only mounted to around $170 million. In 1993, it was reported that these significant economic consequences had grown to $240 millions/year in damages and more than $280 millions/year for coping with phenomenon in the USA only. Limestones and dolomite constitute about 20 percent of all sedimentary rocks (Gilluly, et al. 1959), and 5 to 10 percent of the earth's land surface is karstic (Jackson, 1982), thus Karst occur in many parts of the world which makes it a worldwide threat that should be taken seriously. When no engineering countermeasures are employed, sinkholes continue to cause tremendous damage and pose serious threats to human lives.

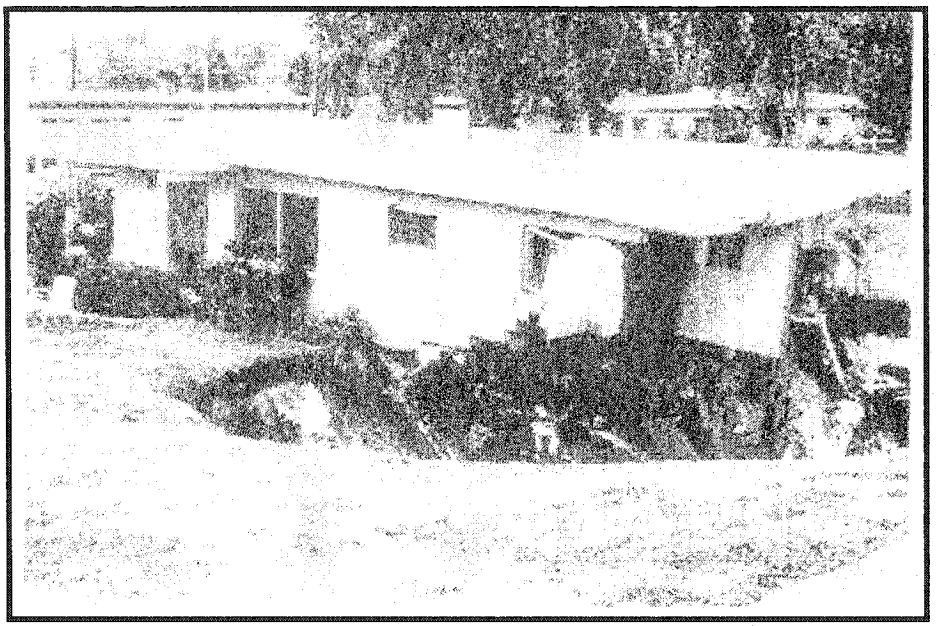

Figure 1.3: Structural failure caused by collapse sinkholes
(Source: After Sowers, 1996)

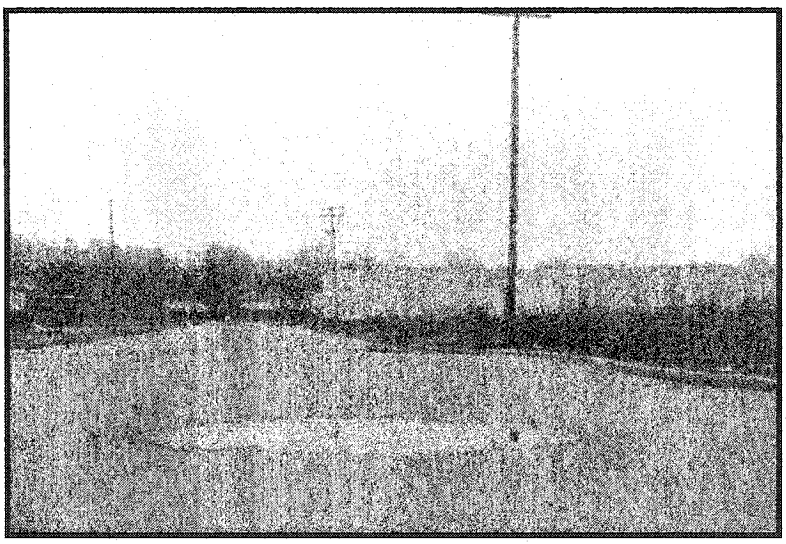

Figure 1.4: Ponding of water in depression
(Source: After Newton 1987)

The study of this worldwide phenomenon is very important as it helps in understanding the events that lead to it and aids in the design to prevent or at least minimize the outcomes of future collapses.

Existing studies of sinkhole hazards have traditionally been the province of civil engineers, geologists, and hydrologists accustomed to working at local scales (Whitman and Gubbels 1999). A new era in the study of sinkhole hazard has started with the development of remotely sensed data sets and computer-based techniques, during the 1980's and 1990's, opening the opportunity for more synoptic studies of the phenomenon; an overview of previous sinkhole studies will follow in chapter 2.

1.2. Research objectives

The aim of this research is to apply Synthetic Aperture Radar (SAR) techniques (Zebker and Goldstein, 1986) to determine the surface deformation in Karstic regions and demonstrates the utility of SAR interferometry for investigating these deformations. Synthetic Aperture Radar (SAR), an imaging radar system, is one of the most advanced engineering inventions of the twentieth century (Soumekh, 1999). SAR images offer a large scale, fine resolution data sets to obtain information about the rate and extent of subsidence in a particular area.

The temporal coverage of SAR images (1992-1997) provides a great tool to monitor and accurately measure the rate of subsidence in areas where sinkholes occur. These 100x 100 km images are made of pixels, with each pixel covering a 30x30 meter area.

This type of satellite had overcome previous satellite remote sensing methods limitations by providing information collected at nighttime with the ability to operate generally independent of weather conditions, and is not even affected by cloud cover or haze (Soumekh, 1999; and Hanssen, 2001). One can only imagine the possible far-reaching scientific, technical, and societal beneficial outcomes of using such a method for studying and maybe identifying areas that are prone to future collapses or subsidence. The methodology and principals of interferometry will be thoroughly explained in chapter 4 of this dissertation.

The primary objectives of the research are:

1- To construct a database of sinkhole case histories, from all around the world, and determine whether these sinkhole dimensions meets the minimum radar resolution requirements.

2- To determine the minimum extent of deformation area that InSAR can detect by conducting a feasibility study that investigates the affects of an underground circular cavity on the ground surface. This study will determine both the minimum cavity diameter and depth below ground surface causing a settlement trough that can be distinguished by radars.

3- Finally, to use differential interferometry techniques to produce interferograms of subsidence, which will involve processing of raw SAR data provided by the European Space Agency to generate Single Look Complex (SLC) SAR images, which are later, used to generate an interferogram that is analyzed to determine surface deformations. In this step, an interferometic

software and data will be used to generate a Synthetic Aperture Radar (SAR) interferogram of an area, were a sinkhole has occurred, to assess the effectiveness of the technique in detecting very small ground surface fluctuations.

1.3. Research outline

This dissertation is organized into 8 chapters. Chapter 1 introduces the research by discussing the research background followed by the research objectives and finally a brief outline of this dissertation. Chapter 2 includes an overview of the reviewed literature and also presents a summary of the previous sinkhole studies. Chapter 3 of this dissertation presents and analysis a subsidence and collapse case histories database developed mainly for research purpose that is later used (Chapter 5) to investigate the relevance of the newly developed technique in studying small-scale ground surface deformations. Chapter 4 will start by providing some justification for the need of using newly developed techniques for studying small-scale ground surface deformations and continues with an overview of the proposed methods past studies, concepts, principals and methodology. Chapter 4 will also include a list of most available interferometric software that can be used for such purpose. The package chosen for interferometric processing in this research along with an example of a generated interferogram, in an area where deformation has occurred, using the chosen software will also be presented in chapter 4. In chapter 5, the conducted feasibility study that investigates the affects of an underground circular cavity on the ground surface is presented. This study determines both the minimum cavity

diameter and depth below ground surface causing a settlement trough that can be distinguished by this technique.

Chapter 6 explains in details the algorithms and procedures implemented in ROI_PAC, the Repeat orbit Interferometry Package developed at JPL and Caltech and used in this research. Chapter 7 presents the implementation of this newly developed technique where interferograms of a subsidence case study, in an area where a sinkhole already exists, are generated and analyzed. Finally, chapter 8 presents the research summary and conclusion and also sketches the plan for future work.

2. Literature review

2.1. Overview

The occurrence of subsidence and sinkholes are reported, studied and documented in areas underlain by carbonate rocks, such as limestone and dolomite, all over the world each year. Subsurface cavities range in size from the small pore spaces between soil or rock particles, to large cavernous room within solid rock (Besnon and La Fountain, 1984).

In order to understand sinkholes and be able to study and detect their occurrence, one should first be able to distinguish the different types and to understand the processes that form them. Sinkholes or dolines, another term used in geologic research, can be divided into three different types depending on what causes them as can be seen in Figure 2.1.

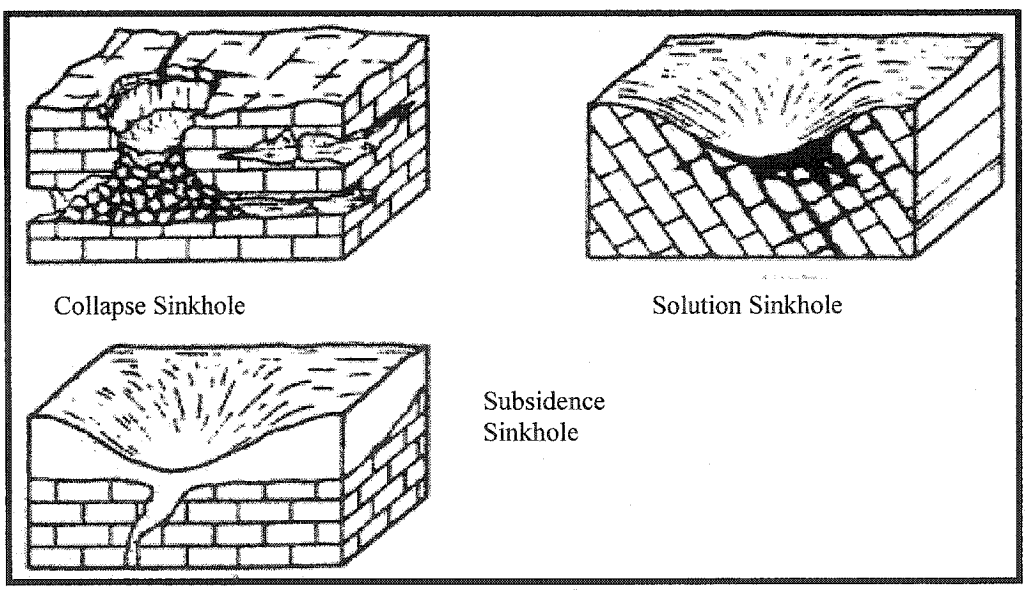

Figure 2.1: Block Diagram of collapse, solution and subsidence sinkholes (Source: Modified from Jennings, 1971)

Beck (1984) gave a simple and detailed explanation of each type as follows: One type of karstic surface depression is that caused purely by bedrock solution, a solution doline or solution sinkhole, these are due primarily to pronounced surface solution of the karst bedrock around some favorable point such as a joint intersection (Jennings, 1971). This type of sinkholes, which is not considered an engineering problem, may be related to groundwater pollution, foundation settling or cracking but not collapse as they are slow and occur gradually.

The second type of sinkholes occur due to the collapse of the roof of a bedrock cavern producing a steep sided, bedrock walled hole possibly widening into interconnected cave passages at depth and thus termed collapse sinkholes.

The third type of sinkholes, as stated by Beck, is termed raveling or subsidence sinkholes. This type represents the vast majority of damaging sinkholes and is described by Jennings (1971) as: "where superficial deposits or thick residual soils overlie karst rock, doline can develop through spasmodic subsidence and more continuous piping of these materials into widened joints and solution pipes in the bedrock beneath". This type of sinkholes occurs in a variety of sizes and shapes and usually produces cylindrical holes that are weathered into conical or bowl-shaped depression.

Although Sweeting (1973) stated that collapse of limestones is fairly frequent phenomenon, despite the fact that it is not often actually recorded, Ogden (1984) argues that in spite that the term sinkhole is defined by many geologist as a circular depression found primarily in carbonate rocks and generally thought to be a result of

collapse, most sinkholes are in fact primarily formed by slow preferential dissolution of rock along fractures or by slow subsidence due to piping of a surface cover, and thus making it the most damaging type of sinkholes. Although most factors involved in causing the occurrence of sinkholes are considered the same, they can be divided into two different categories known as induced and natural. Newton (1984), Ogden (1984) and many other researchers have identified induced sinkholes as those caused or accelerated by human activities, whereas natural sinkholes are those caused by the solutional enlargements of subsurface openings in carbonate rocks by water over thousands of years without the interference of man's activities. Natural sinkhole are the product of a process that can span many thousands of years which makes their formation under natural conditions during a man's lifetime relatively rare. In contrast, induced sinkholes are considered abundant as the time frame could be reduced to days or even hours by human activities. In a cause of collapse study by Benson and La Fountain in 1984, data of 96 cases of collapse recorded over a five-year period were obtained from the Florida Department of Transportation. These data were analyzed and the result reported as the key point of this study was that within the lifetime of a manmade structure, 100 years or less, the solution of rock and even the mechanical erosion of rock have little to do with the final cause of collapse, furthermore, factors contributing to collapse are not necessarily singular. One can conclude that changes made to the natural environment by man's activities over the short term are by far the most significant factor in forming and triggering sinkholes.

Benson and La Fountain (1984) also reported that though many variables contribute to the ultimate cause of collapses, a singular event usually acts as the final triggering mechanism.

Lamoreaux (1984) identified heavy rain, large seasonal fluctuation in water table and other changes in the hydrology regime affecting residuum stability to be the main factors triggering the formation and development of natural sinkholes. On the other hand, most, if not all, reviewed literature on sinkhole development agreed on dividing the induced factors triggering sinkholes into two categories, pumpage from wells and construction activities. Ground water withdrawal causes decline in water table level and thus trigger sinkholes due to either loss of buoyant support, erosion caused by the increase in velocity of ground water movement, water level fluctuation or increase of recharge, piping, which could lead to large-scale catastrophic collapse as reported by Ogden (1984). Construction activities such as excavating, dewatering, mining, heavy equipment traffic, blasting and even altering natural drainage patterns could act as triggering factors and accelerate or even cause the formation of new sinkholes. These activities cause or accelerate the occurrence of sinkholes as reported by Newton (1984) due to either piping, in cases where water table level is below bedrock, saturation caused by leakage, where loss of cohesion and loading is caused by additional water impounding or simply the emplacement of load over thinned roofs of existing cavities for example. Sinkholes occur whenever vertical permeability makes them possible.

Permeability is a measure of a rock's ability to allow fluid to move through its pore spaces, so the greater the permeability, the more likely sinks are to develop (Littlefield et al., 1984).

Many examples of sinkholes were reported and documented throughout the world. One of the most famous sinkholes reported, because of its immense size, is the Winter Park sinkhole that developed in Florida in 1981. The sinkhole as reported by Jammal (1984), had developed as a conical hole in overburden and was about 106 meters (348 feet) in diameter and 30 meters (98 feet) deep (Figure 2.2). A resident of a house, subsequently lost in the hole, mentioned hearing swishing noise and noted that a large sycamore tree disappeared into a hole. Streets, utilities, recreational facilities, one house, several businesses, and several cars were destroyed and damaged as a result of the formation of the sinkhole (Figure 2.3). Jammal investigated the sinkhole for ten months and concluded that although the Winter Park sinkhole formed rapidly, it was formed as a result of a long-term erosion and raveling of overburden material into cavernous limestone, not a roof collapse in limestone. It was Jammal's opinion that the sinkhole had been forming over long-time period, and that formation was accentuated over a period of about 50 years, resulting from a progressive decline of the piezometric level of the Floridian aquifer due to extended below average rainfall and early pumping of wells (Jammal 1984).

Another example of a catastrophic sinkhole, causing loss in human lives and damage to property, is the one that was reported by Brink (1984).

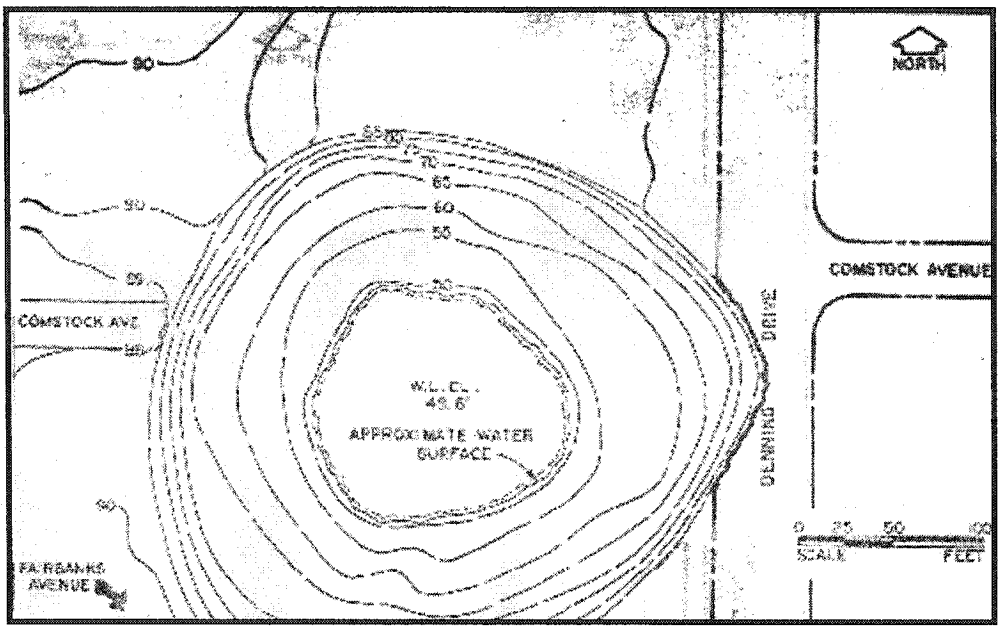

Figure 2.2: Topography of Winter Park sinkhole
(Source: After Jammal, 1984)

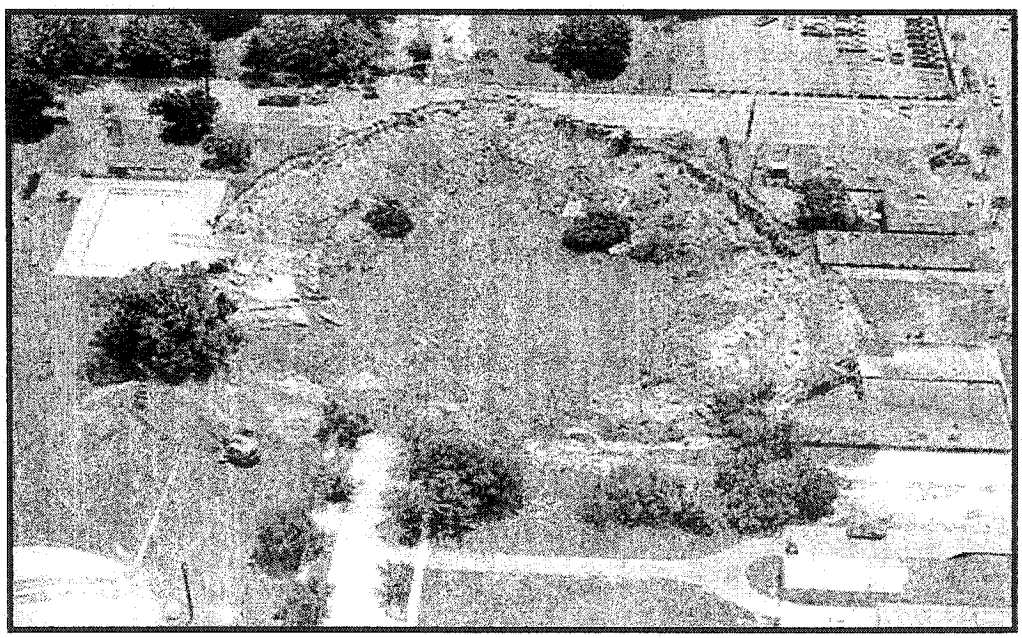

Figure 2.3: Damage caused by Winter Park sinkhole
(Source: Photo by Phil Eschbach, 1981)

This sinkhole occurred in the Transvaal Province of South Africa in 1962 where Carbonate rocks occupy six thousand square miles of the Province. The sinkhole that occurred in the area, where one of the richest gold mines in the world situated, swallowed a three-story crusher plant building and none of the twenty-nine occupants of the building were seen again.

The study of this induced sinkhole showed that the development was accelerated by the mining activities in the area where water table has been lowered through the dolomites in order to facilitate sinking of shafts down to the gold-bearing ores (Brink, 1984).

Kastning (1989) reported that Karstic landforms, such as sinkholes and solutionally widened fractures, in many cases form easily recognizable patterns including lineaments and dendritic networks. Specific features related to topographical, geological and hydro geological conditions could help in identifying the formation of sinkholes, thus its important to include careful mapping of topography in relation to exposed beds, lithological properties of beds containing sinkholes and mapping of joints and other fractures in the investigating the development of this phenomenon. Benson and La Fountain (1984) identified the three key methods that may be used in subsurface investigations as follows:

1. Direct sampling methods such as drilling
2. Indirect methods such as remote sensing and geophysics
3. Statistical methods

Before choosing the appropriate method of investigation it is important to fully understand the methods and how to apply them, know the strengths and weaknesses of each method, be familiar with the tools and budget available and finally understand how desired results are produced. An overview of the key methods will follow, explaining each in details, giving examples of previous reported studies as well as documented results.

2.2. Overview of previous sinkhole studies

The investigation of sinkholes development should include careful mapping of the topography, determination of lithologic properties of the area affected and mapping of the joints and other fracture in caves or sinkhole walls.

Although most Karst forming processes take place underground and out of sight, it is still possible to study them (Lane, 1986). Warner (1984) further reported that in spite that there may be no outcrops present, nor other signs of such fracture, areas with such sinkhole potential may be perfectly stable until man's activities interfere with the balance. Intensive research effort on the phenomenon was undertaken and currently underway. Based on field and experimental studies, several methods have been proposed for the investigation and study of sinkholes and are classified to direct, indirect, and statistical methods. In the remainder of this section, examples of all three classifications will be reviewed and discussed.

2.2.1. Direct sampling methods

This category includes all methods in which the soil and rock are examined directly by coring, drilling, penetration testing or other methods (Wagener and Day, 1984). Lane (1986) reported that until mid 1980's, direct methods were the only possible methods to study Karst and understand the process of their formation. Drilling is considered one of the oldest and most straightforward approaches to evaluating and studying sinkholes where holes are drilled to deep depths with an objective to locate cavities (Figure 2.4). If cavities were found in an area, they were either bypassed using piles supported by bedrock or sealed by grouting, a mixture of soil, cement and water.

This hindsight approach can be used to study the area of interest and understand what happened only after collapse has occurred. This investigating approach has limited predictive capability as even though in some cases, high-density boring programs are carried out, cavities can often escape detection, as ability to locate the fracture systems that contribute to the instability of a terrain underlain by cavities is not always easy to identify. Using this method, one cannot say with any degree of certainty where or even when the next sinkhole will form. In spite of its limited predictive capability, this approach as reported by Lane (1986) is still the accepted engineering standard for assessing a site's foundation qualification. The number, locations, and depths of test holes are specified depending on the expected types and depths of soil and bedrock, size of building, and type of proposed foundations (Lane, 1986).

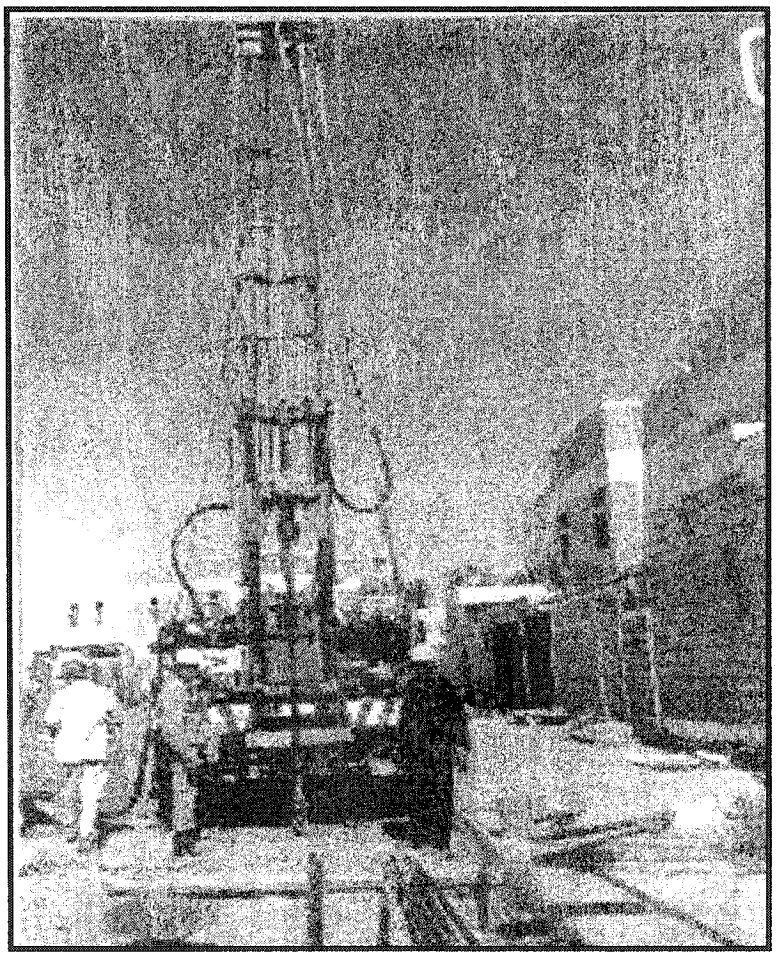

Figure 2.4: Drilling in progress
(Source: After Al-Mutairi et al., 1998)

Drilling has been used in studying and investigating sinkholes worldwide. For instance, Al-Mutairi et al. (1998) reported that a geotechnical investigation consisted of drilling boreholes to depths of between 40 and 83 meters well within the underlying limestone bedrock was carried out in Al-Dhahar area in Kuwait were the area has experienced several collapses. The location of boreholes were carefully selected to cover zones carrying different sinkhole potential risk factors, which were assigned after reviewing the microgravity contour maps that indicated the area of possible existence of underground cavities within the limestone and the overlying soil (Al-Mutairi et al., 1998). It was reported that incidents where there was a loss of water circulation or rapid drop downs of drill rods occurred and were considered as an indicator of the existence of fracture and cavities within the bedrock.

These assumptions were later on confirmed by lowering video cameras inside selected boreholes. Samples of boreholes collected showing highly weathered limestone are shown in Figure 2.5.

Direct sampling methods are considered somehow expensive, slow, and have limited predictive capabilities if compared to other available methods. Apart from the fact that they provide point information with a relatively high degree of confidence, if used alone, direct sampling methods could affect the accuracy of a site investigation. This approach could be combined with other methods providing aerial coverage to better understand and study the phenomenon.

2.2.2. Indirect methods- Remote sensing

2.2.2.1. Geophysical methods

The most definitive means other than an expensive drilling program for locating fractures, sinkholes, and caves is to utilize shallow geophysical techniques, which should only be used for general guidance purposes to indicate the presence or absence of natural cavities across an area rather than as an absolute survey of cavities present at a site (Fischer et al., 1989). Several geophysical techniques are available; each suited to a specific setting, and is attractive to be used as a starting point of an investigation as they provide aerial coverage with reasonable cost. Lane (1986) reported that some geophysical methods operate on the principle of detecting and monitoring changes in natural properties of the earth, such as microgravity surveys; others rely on monitoring changes in man-induced signals into the soil or bedrock, such as ground penetrating radar, sound waves, and electrical currents.

Regardless of what method used, the main objective of using such methods rely on their usefulness in detecting and evaluating any underground anomalies that may help in identifying and locating subsurface cavities. Following is an overview of the four most common geophysical techniques that have been successfully used in studying the phenomenon.

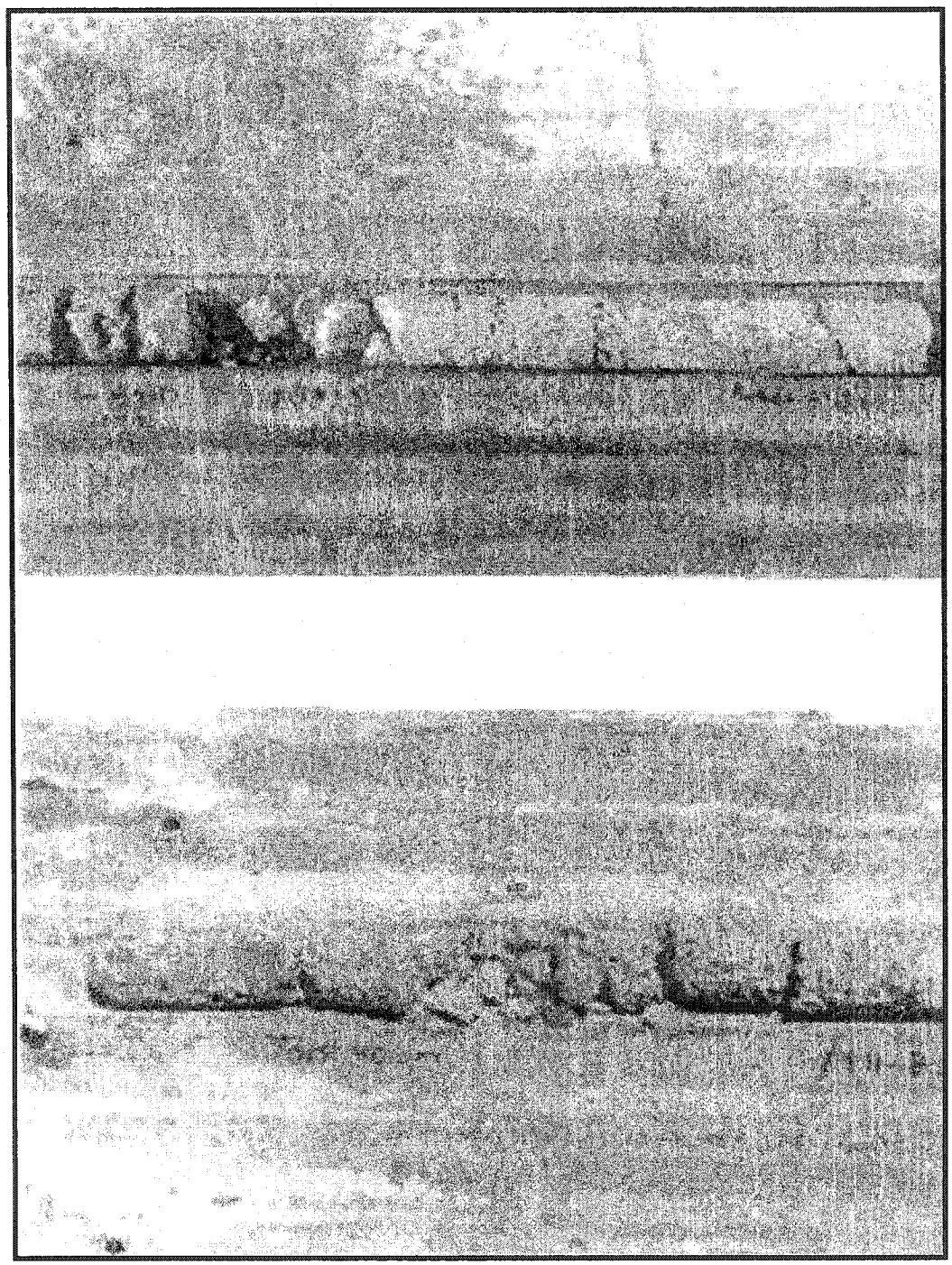

Figure 2.5: Samples of highly weathered and porous Limestone
(Source: After Al-Mutairi et al., 1998)

2.2.2.1.1. Microgravity surveys

The microgravity survey measures the changes in the earth's gravitational field due to local variations in the density of subsurface strata. Extremely small variations in the gravitational acceleration with great accuracy can be measured using modern gravimeter such as LaCoste and Romberg Model D. Latitude, elevation, topography of the surrounding terrain, tidal movements and lateral changes in the density distribution of the subsurface region can all affect the values of measured gravity. Nevertheless, eliminating the large variations due to these factors is possible and thus obtaining, with great deal of accuracy, the net effect due to density variations associated with subsurface formations such as sinkholes. Ogden (1986) has reported that the continued corrections for instrument drift, elevation and terrain cause gravity surveys to be tedious; however, their effectiveness can often outweigh the time constraints involved.

Data acquired in the field can be used to produce residual Bouguer gravity maps as can be seen in Figure 2.6. Interpretation of these maps is based on the measured Bouguer values minus the regional gravity gradient. A negative residual Bouguer gravity anomaly signifies a mass deficiency beneath a particular area, which could be considered as an indicative of an air-filled or partially filled cavity at depth.

One should keep in mind that these techniques are unable to distinguish between small features close to the surface and large features at depth, Moreover, its is useful in locating cavities, but as Ogden (1986) reported, difficult to be used in determining the depth or size of the cavities observed. Thus all anomalies detected by

microgravity techniques should be further investigated using other available methods such as drilling to obtain conclusions as to their significance. Many researchers have shown that microgravity techniques are useful in locating cavities (Al-Mutairi, 1998; Fischer et al., 1989; and Ogden, 1986) as they have been successfully utilized in delineating negative anomalies such as filled sinkholes and cave passages.

The main advantages of this technique relies in the minimal disturbance it cause to the investigated area and its inhabitants, its non-destructiveness, and the fact that it requires a small crew to implement it.

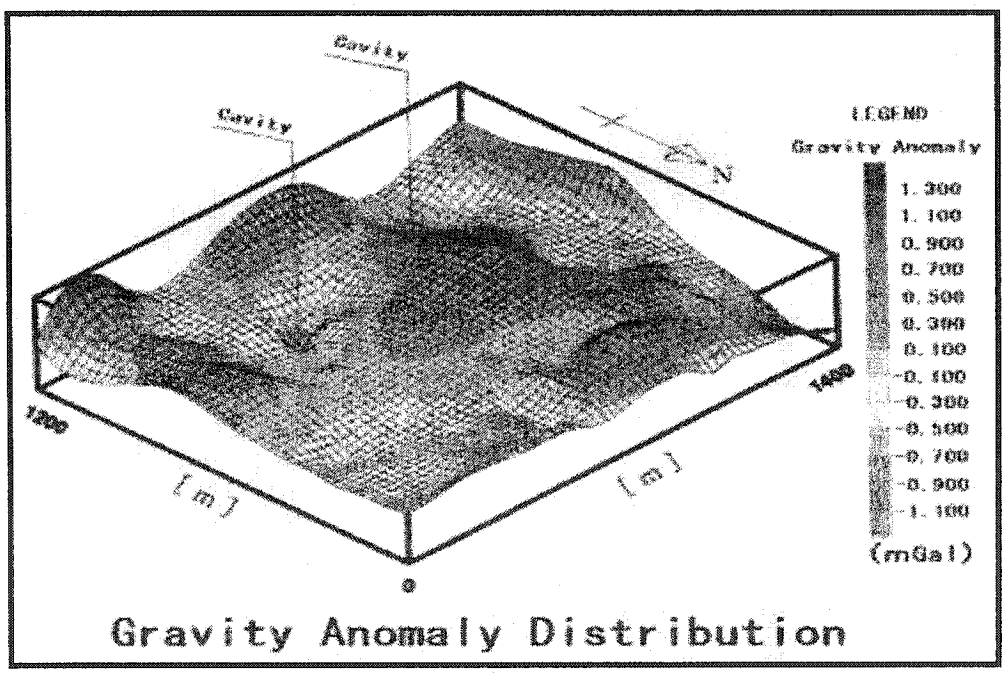

Figure 2.6: Final gravity anomaly map corresponding to the underground density anomaly distribution
(Source: After OYO Corporation, 2000)

2.2.2.1.2. Electrical resistivity methods

Electrical resistivity techniques are generally used to measure the natural resistivity of soil, rocks, and groundwater thus; are often used for detecting variations in composition of the overburden or bedrock and detecting the existence of underground voids. This technique as reported by many researchers (Wagener and Day, 1984; and Lane, 1986) uses arrays of electrodes in different configurations that are set out along traverse lines across the site being investigated as can be seen in Figure 2.7. One pair of electrodes injects an electrical current into the ground generating a measurable voltage field between its self and a second pair of electrodes. Figure 2.8 shows a map constructed from data collected by a resistivity survey, where each dot represents a survey station and the contour lines representing the relative resistivity changes over the area being investigated and thus confirm the existence of subsurface cavities. The main advantages of these methods are their low costs and ease of operation. On the other hand, they can be time consuming, as each station has to be set up readings taken before one can move to the next station. Unfortunately, Werner (1984) reported that electrical resistivity methods couldn't be used where there are buried pipes, cables, or where high current or high-voltage power lines exist in the vicinity nor in paved areas such as parking and roads as they tend to produce incorrect results.

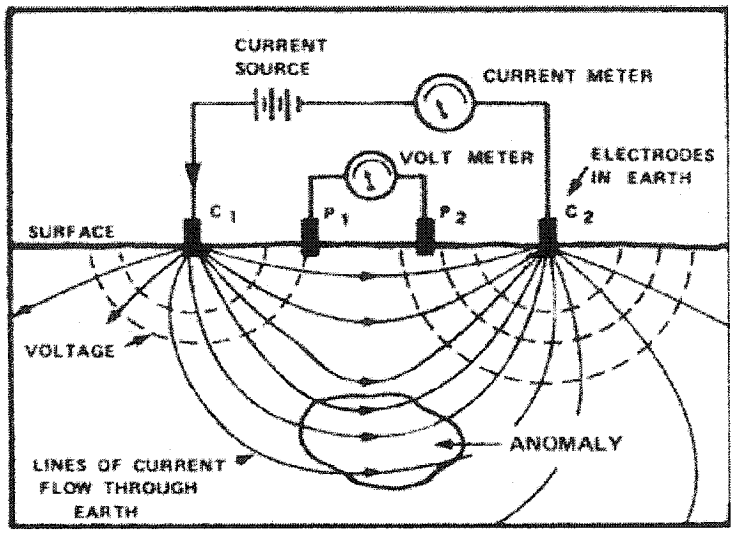

Figure 2.7: Basic resistivity measuring configuration
(Source: After Lane, 1986)

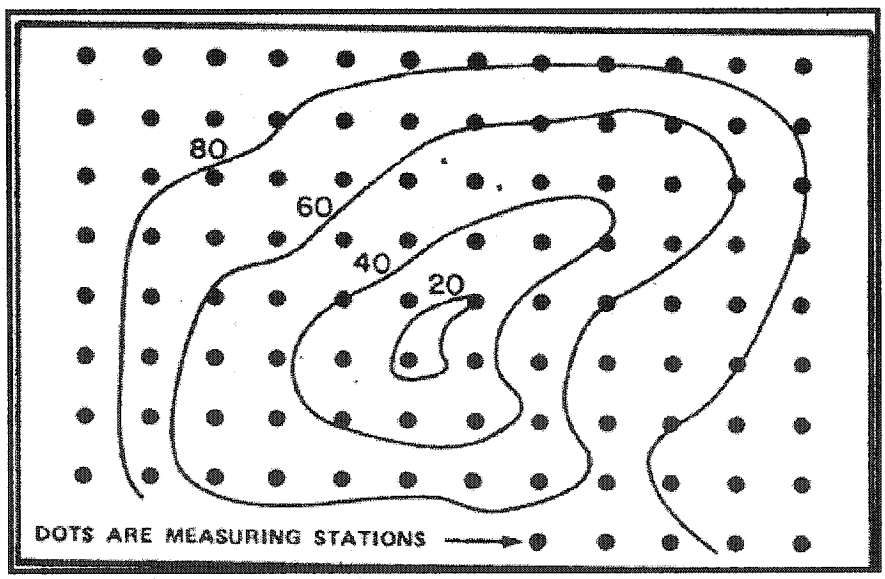

Figure 2.8: A map constructed from data collected by a resistivity survey
(Source: After Lane, 1986)

2.2.2.1.3. Ground penetration radar (GPR)

GPR is a contemporary technique widely used in the investigation of sinkholes as it provides unique cavity detection capabilities by obtaining continuous subsurface information at rapid traverse speeds, and thus is effective for both reconnaissance and detailed site investigations as reported by Benson and La Fountain (1984). This technique as shown in Figure 2.9, uses high frequency electromagnetic radiation and produces graphic profiles of subsurface conditions such as the configuration of strata, water table, cavities, buried pipes, and other subsurface features by processing the reflected energy waves (Lane, 1986). Benson and La Fountain (1984) reported that this technique provides the highest resolution of all surface geophysical methods and that depths of one to fifteen meters or more may be obtained, however, the depth of penetration is site and soil conditions dependent. GPR was used to study sinkhole formation on interstate highway I-78 in western New Jersey and was successfully able to locate subsurface cavities as can be seen in Figure 2.10. The Figure shows a GPR scan showing a new sink near surface below the shoulder of I-78.

The main advantages of this technique are its continuous nature of operation as the antenna is moved slowly across the ground surface, mobility of equipment that makes total site coverage economically feasible, and the on spot analysis of data using picture like radar presentations (Lane, 1986). On the other hand, since this technique uses electrical energy, it can be severely limited by local condition such as soil moisture.

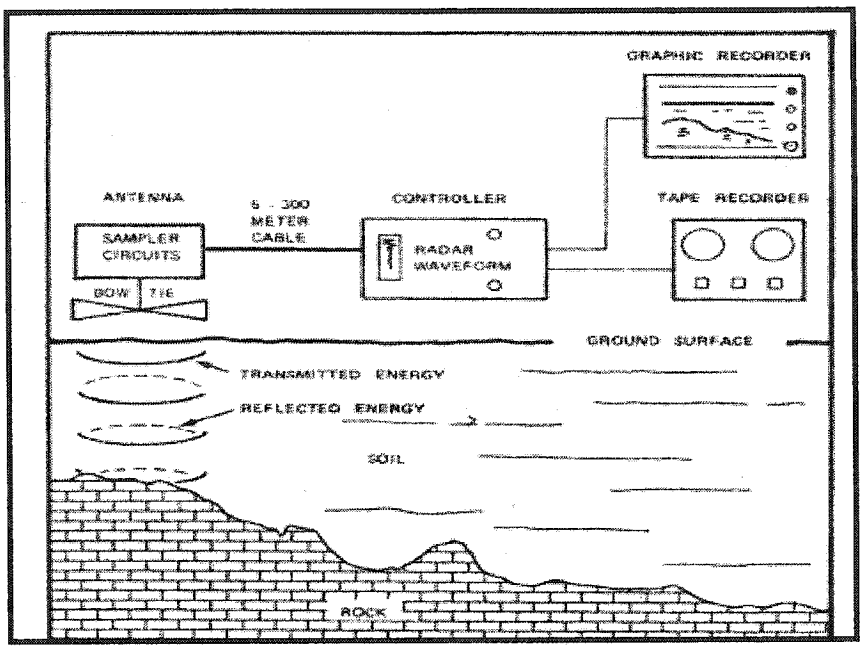

Figure 2.9: Block diagram of ground penetrating radar system
Radar waves are reflected from soil/rock interface, electronically processed, and then recorded on tape and graphically
(Source: After Lane, 1986)

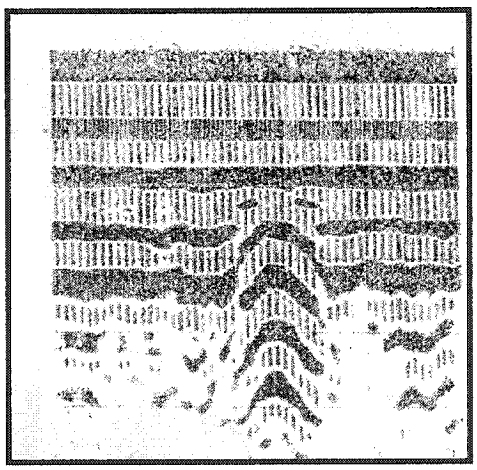

Figure 2.10: GPR scan made in 1993 showing new sinkholes near surface
(Source: After Mellett and Maccarillo, 1995)

2.2.2.1.4. Seismic refraction

Lane (1986) reports that this technique transmits seismic energy waves into the subsurface to determine the depth to and thickness of rock strata, depth to the water table, and anomalous features such as cavities (Figure 2.11). Transmitted waves, traveling at different velocities in different density materials, are refracted and reflected at the interfaces between different composition strata and thus detected by an array of microphone sensors located on topsoil.

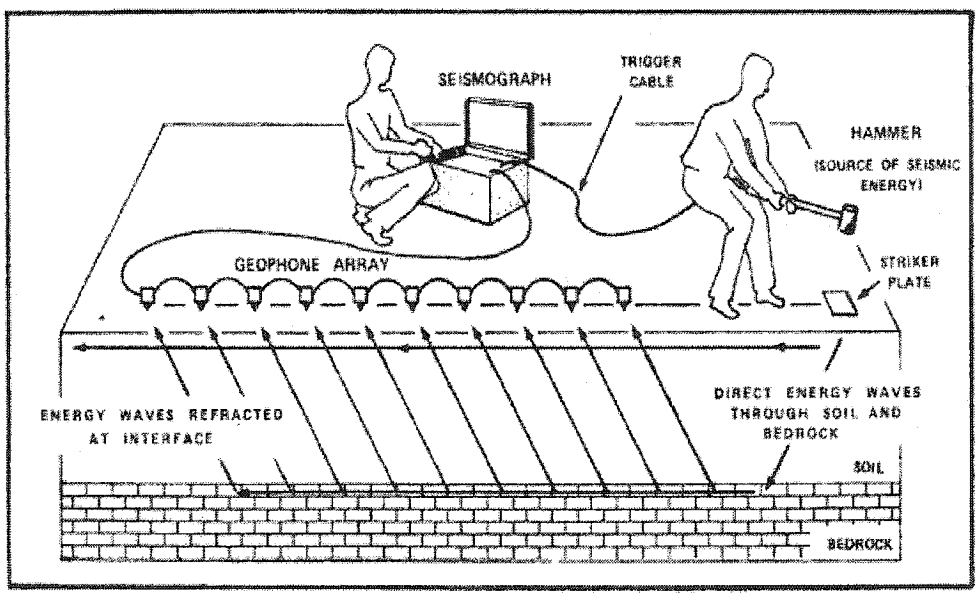

Figure 2.11: Field layout of a 12-channel seismograph showing the path of direct and reflected seismic waves in a two layer soil/rock strata
(Source: After Lane, 1986)

These reflected signals are then electronically processed producing subsurface features indicative patterns (Figure 2.12). Although the amount of energy transmitted limits the depths to which this technique is effective, transmitting large energy can penetrate deeper strata. The only weakness this technique suffers from is its sensitivity to extraneous vibrations especially when used in urban areas.

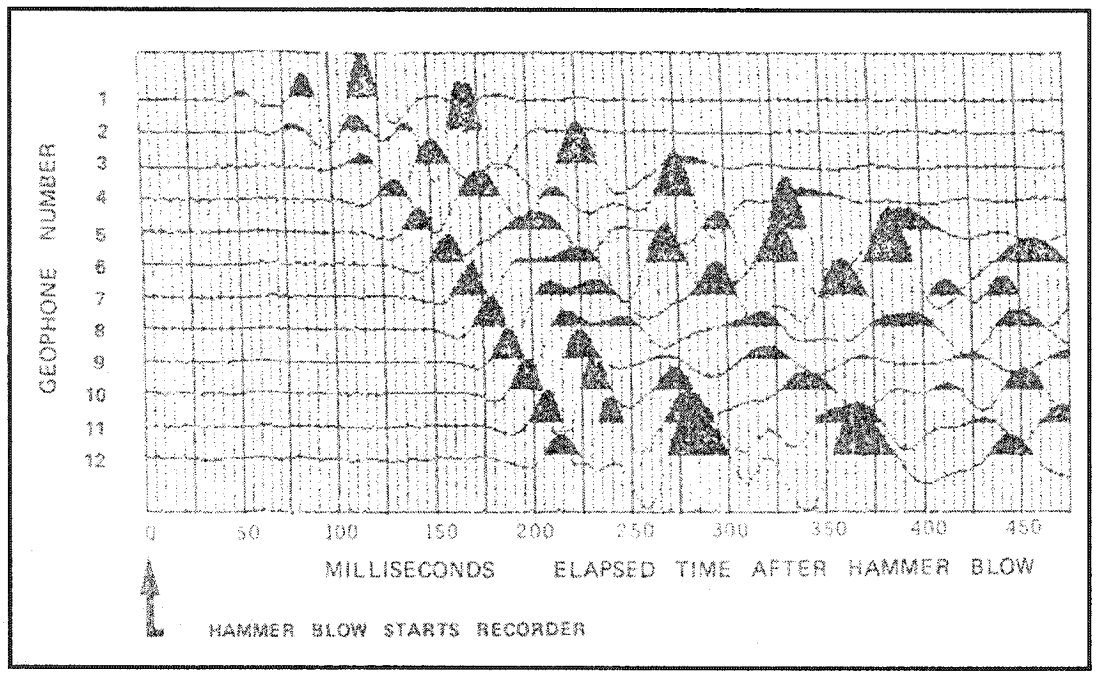

Figure 2.12: Recording from a 12-channel seismograph
(Source: After Lane, 1986)

2.2.2.2. Aerial photography

Conventional aerial photographs are black and white pictures of a terrain taken with special cameras mounted in airplanes. Color aerial photos can also be taken using films sensitive to different portions of the electromagnetic spectrum, recording light across the entire visible spectrum. Black and white photos are preferred as they show fine details and features of landscape. Lane (1986) reports that because of aerial photography's high altitude point of view, surface features can be easily observed over a wide area, including topography, vegetation, and geomorphology. Trained observers using surface features on these photos can provide information about subsurface conditions such as cavities that could not be noticeable from the ground. Lane (1986) further reports that Karst usually has a controlling influence on local groundwater, such as flow patterns, recharge, and discharge areas and thus anything that reflects groundwater conditions may be a clue to the existence of Karst. Figure 2.13 shows an aerial photo showing numerous sinkholes in an area west coast of Florida where major collapses have occurred and large cavities of up to 100 meters in diameter were found.

2.2.2.3. Satellite imagery

Satellite imagery is a newly developed technique used in the study of sinkholes utilizing unmanned, earth-orbiting satellites carrying automatic television like sensors. With each orbit, satellite sensors transmits signals and records the backscatter and stores the information in order to transmit them to tracking stations on earth.

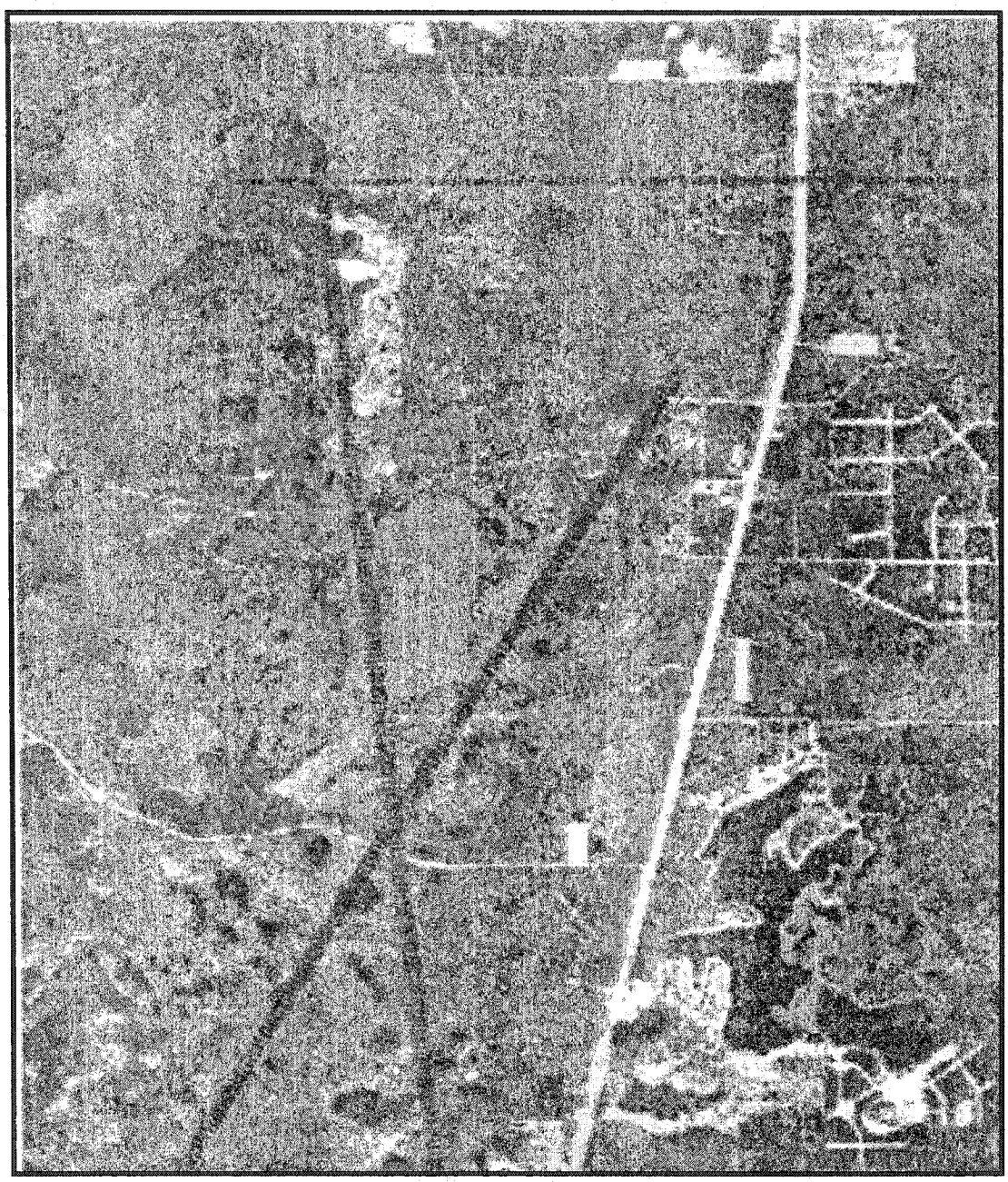

Figure 2.13: Aerial photo from an area West Coast of Florida
(Source: After: Benson and La Fountain, 1984)

This information when processed by computers generates images that are pretty similar to aerial photos but are not true photographs. This high altitude and speed technique when compared to aerial photography surveys of the same area, can cover much more territory and in less time. In spite of its aerial coverage and less required time, this technique can only identify large ground features due to its resolution. Chapter 4 of this dissertation will explain this technique in more detail, whereas chapter 5 will determine the feasibility of using such a technique in investigating and studying sinkholes.

2.2.3. Statistical methods

Sinkhole collapses and subsidences usually affect large areas and thus should be treated using different approaches than that of localized problems. Benson and La Fountain (1984) reported that assessing regional problems to maintain reasonable levels of accuracy in an investigation or mapping program depends heavily upon the integration of information from many sources to provide an overview of conditions that can be thought of as a statistical database. Generating regional probability maps using regional data such as geologic and hydrologic information, aerial photo interpretation, and even records of recent collapses can identify areas susceptible to collapse.

These methods have been used by several researches all around the world and have produces promising results. One such study is the use of geographical information systems (GIS) techniques to visualize large-scale patterns of sinkhole distribution in order to conduct statistical tests of hypotheses about their formation.

2.2.3.1. Brief review of GIS

Geographical information system (GIS) is a computer-based tool consisting of a collection of computer software and hardware that can be used to visualize, manipulate, analyze, and display data tied to spatial locations. These newly developed systems are widely used in a wide range of public and private enterprises as a tool for explaining events, predicting outcomes, and planning strategies. The key feature that distinguishes GIS from other information systems is its ability to integrate common database operations such as query and statistical analysis with the unique visualization and geographic analysis benefits offered by maps. In these systems, the geometric location of a feature is stored along with attribute information describing what each feature represents. Either vector or raster data structure is used to store location information with corresponding attribute stored in a set of tables geographically related to the features they describe. For a better understanding of GIS, one can refer to a book titled Principles of geographic information systems by Peters Burrough and Rachael McDonnell.

Gao et al. (2001) used GIS software to sort and visualize locations of sinkholes, generating a probability map of Winona county in Southern Minnesota based on sinkhole distribution, bedrock geology, depth to bedrock and other factors with results showing that sinkholes are strongly clustered. Whitman and Gubbels also used GIS technology to investigate the spatial relationships between hydro geological factors and sinkhole formation near Orlando, Florida.

The level of site assessment undertaken should be a function of the known susceptibility of the site to subsidence; the critical nature of construction, the level of probability or confidence desired by the investigation, and the overall project economics (Benson and La Fountain, 1984).

In this research, satellite imagery methods will be taken into consideration and will be further studied to determine the utility of using such an approach in studying sinkholes. More specifically, a newly developed technique, Synthetic Aperture Radar (SAR) Interferometry, will be explained in details and later be used to detect very small ground surface fluctuations. If proved successful, this technique will be used to detect small ground surface motions due to the existence of sinkholes and thus assess its effectiveness in studying the phenomenon.

3. Sinkhole database development

3.1. Overview

In this study, a particular purpose database is developed to store and organize all the information related to collapse or subsidence sinkhole occurrence. The concept of relational data model that was introduced by E.F. Codd of IBM San Jose Research Laboratory in the late 1960's (Codd, 1970) is used to design the database along with Microsoft Access, the Relational Database Management System (RDBMS) chosen to develop the database due to its availability on most computers. The concept of relational databases uses the theory of a mathematical relation as its basic building block and has its theoretical basis in set theory and first order predicate logic (Elmasri and Navathe 2000). A relational database consists of a collection of tables, each of which is assigned a unique name with each row representing a relationship among a set of values (Silberschatz et al., 2002).

It is important in the design of the database to organize the data within each task-oriented database to make the performance of the database efficient. The database structure, which includes data sources, flows, transactions, and updates, should be carefully designed to achieve that task. The use of relational database management tools could help control many potential problems associated with database design and applications. A careful design would result in a good database relationship and thus reduce data redundancy, avoid inconsistencies, and maintain data integrity efficiently.

A large number of data from several collapse and subsidence sinkhole case histories are available in different sources (Steiner, 1975; LaMoreaux, 1984; and Al-Mutaiti et al., 1998). Large sinkhole occurrences such as the 1984 Winter Park sinkhole in Orlando, Florida (Schmidt and Scott, 1984; Jammal, 1984; and Lane, 1986), the 1970 Transvaal sinkhole in South Africa (Brink, 1984; and Wagner and Day, 1984), and Big Sink sinkhole in Shelby, Alabama (LaMoreaux, 1984) provide great amount of data on sinkhole occurrences that can be used in studying the phenomenon and thus gives a great opportunity to evaluate the engineering effects of sinkhole occurrences in urban areas which plays a big rule in predicting future collapses and subsidence.

The collapse and subsidence sinkhole database includes three interrelated tables, sinkholes worldwide, reference list, and references. The first table, sinkholes worldwide, includes important sinkhole information such as the country where the sinkhole occurred, the name of the sinkhole, if any, the date of occurrence, shape of sinkhole, sinkhole dimensions, causes, first signs, and initial treatment carried out at the site. The second table, reference list, serves as a tool relating each sinkhole with the reference used as a source of information for it in the reference table. The last table, references, includes detailed information of the references used in collecting the data listed in sinkhole worldwide table such as the authors name, reference title, material type, publisher and other important information that will help in easily locating the reference if needed.

Up to this date, data of about 82 sinkholes spread worldwide were collected and input into the database, some fields were left blank due to lack of sufficient information. Figure 3.1 shows the preliminary relationships for the collapse and subsidence sinkholes database.

3.2. Results

A relational sinkhole database was developed in Microsoft Access for structuring the large amount of data on collapse and subsidence sinkholes. This database included all the important information collected for each incident and thus can be used to further investigate and understand the phenomenon. The database included collapse and subsidence sinkhole information gathered from 82 sinkhole incidents that occurred in different parts of the world, some of which caused losses in human lives, others that were very large is size causing a great amount of damage to structures and life lines. Data of gigantic collapses such as the Winter Park sinkhole that occurred in Orlando, Florida in 1981 with diameter ranging up to 106 meters, the 400-meter diameter Tianqum cave sinkhole that occurred in Sichuan, China, and other deadly sinkholes such as the 100-meter diameter sinkhole that occurred in Transvaal, South Africa in 1970, are included in the database. Figure 3.2 shows a snap shot of the developed database showing the sinkholes worldwide table.

Although subsidence sinkholes occur more often, they were rarely documented. However, surface collapse sinkholes are better documented and references were easier to locate. The database contained 89% surface collapse sinkholes and only 11% subsidence or raveling sinkholes as can be seen in Figure 3.3.

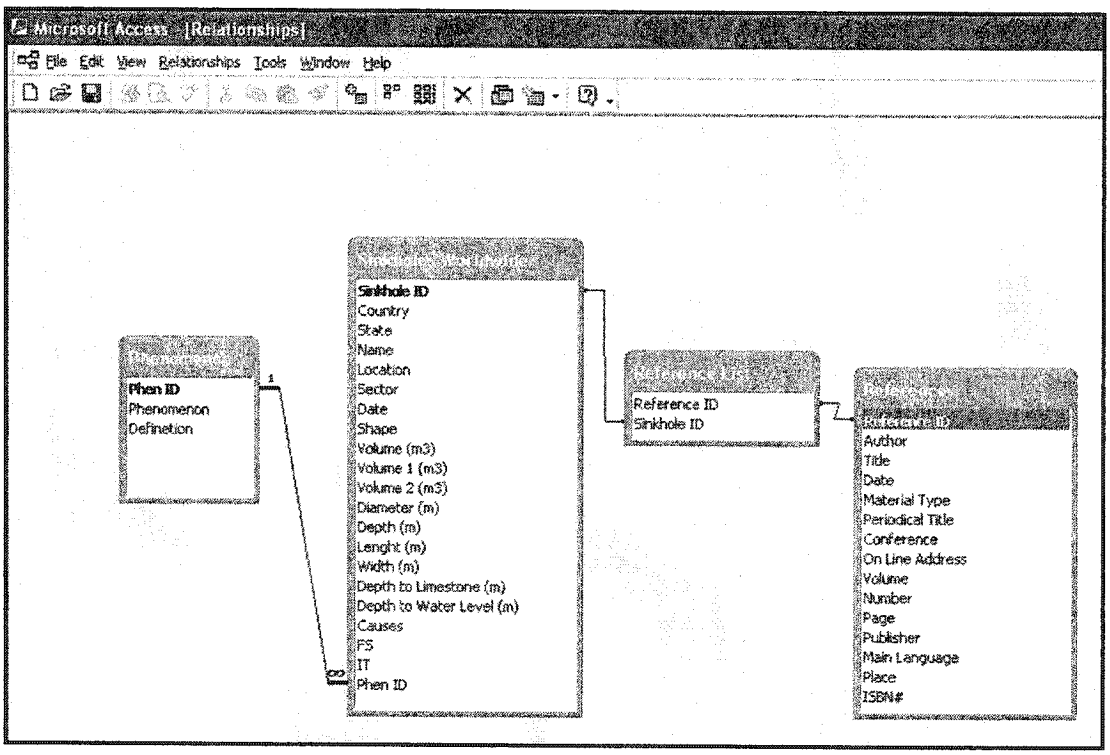

Figure 3.1: The preliminary relationships for the collapse and subsidence sinkholes database

File Edit View Insert Format Records Tools Window Help

Sinkhole ID	Country	State	Name	Location	Date	Shape	Volume (m3)
23	USA	Florida		Dover	1/22/1977	non-circular	1.296
24	USA	Florida		Dover	1/22/1977	non-circular	21.6
25	USA	Florida	Teague	Gainesville			
26	USA	Minnesota		Altura	4/27/1976		
27	USA	Minnesota		Altura	5/7/1976	Circular	
28	USA	North Carolina		Sunny Point	12/1/1976	Circular	
29	USA	Maryland		Westminster	3/31/1994	Non-circular	225.113
30	USA	Maryland	Route 31	Central Maryland	4/30/1994	Circular	
31	USA	California		San Francisco	12/14/1995		
32	USA	California	Embarcadero	San Francisco	3/14/1990	Non-Circular	33.43
33	USA	Mechigan		West Pit	10/14/1979	Circular	
34	USA	Mechigan		West Pit	8/31/1979	Circular	
35	USA	Mechigan		West Pit	10/19/1979	Circular	
36	USA	Mechigan		West Pit	7/15/1983	Circular	
37	USA	New Jersey	Thomas st. sinkhole	Phillipsburg	6/16/1983	Non-Circular	0.774
38	USA	North Carolina		Pender Co.	8/29/1983	Circular	
39	USA	North Carolina		Pender Co.	8/29/1983	Circular	
40	USA	North Carolina		Pender Co.	8/29/1983	Circular	
41	Kuwait	Al-Ahmadi		Al-Dhahar	7/6/1965	Circular	
42	Kuwait	Al-Ahmadi		Al-Dhahar	4/17/1988	Circular	
43	Kuwait	Al-Ahmadi		Al-Dhahar	4/21/1988	Circular	
44	Kuwait	Al-Ahmadi		Al-Dhahar	10/31/1988	Circular	
45	Kuwait	Al-Ahmadi		Al-Dhahar	6/8/1989	non-Circular	150
46	China	Hunan	Bifang Copper mine Sinkhc	Bifang		Circular	
47	China	Sichuan	Tianqum cave sinkhole	Xingwen		Circular	
48	Pakistan		Tarbela dam sinkhole	Tarbela	8/1/1974	Circular	

Figure 3.2: A snap shot of the developed database showing the sinkholes worldwide table

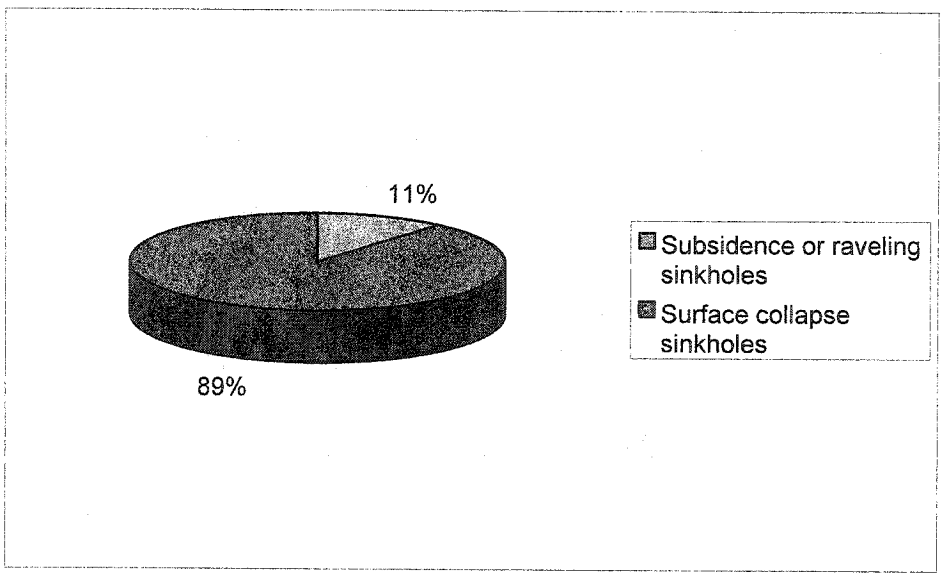

Figure 3.3: Distribution of sinkholes by type

Sinkholes were divided into two types according to shape; they were either circular or non-circular, which included all irregular shaped sinkholes. The database consisted of 63% circular, 28% non-circular and 9% indeterminate sinkholes. The sinkholes ranged in depth from a minimum of 0.2 meters to a maximum of 176 meters with a mean equal to 14 meters and a standard deviation of 25 meters.

The Tianqum cave circular sinkhole in China had the largest diameter (400 meters) in the database while a sinkhole in Georgia; USA had the smallest diameter (1 meter). The mean sinkhole diameter was 37 meters with a standard deviation of 65 meters.

The mean length and width of non-circular sinkholes were 35 meters and 15 meters respectively with a standard deviation of 36 meters and 30 meters. The largest non-circular sinkhole was the one that occurred in Alabama, USA in 1972 with a length of 140 meters and a width of 115 meters. The depth to limestone ranged between 2 to 215 meters with a mean equal to 38 meters and a standard deviation of 48 meters, while the depth to water level had a minimum of 1.5 meters and maximum of 122 meters with mean equal to 22 meters and a standard deviation of 27 meters. The database included case histories that occurred between 1960 and 2001. In most cases, sinkholes occurrence dates were well documented (Figure 3.4).

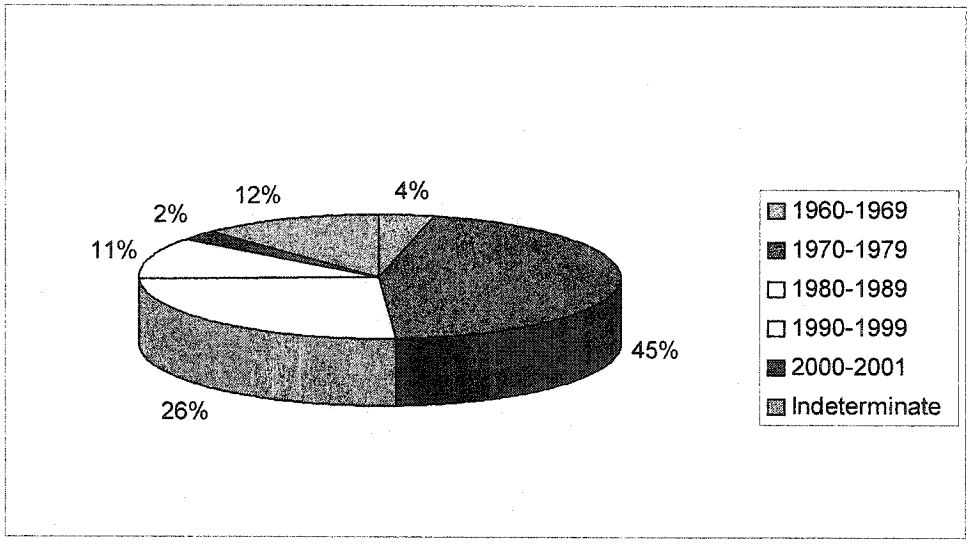

Figure 3.4: Percentage of sinkholes by year of occurrence

4. Methodology

4.1. SAR interferometry

The main objective of this proposal in to propose a method for detecting and monitoring sinkholes and subsidence susceptibility over large Karstic areas using the small ground surface elevation changes that can be detected by the newly progressed Synthetic Aperture Radar (SAR) interferometry technique. Within a decade, imaging radar interferometry has matured to a widely used geodetic technique for measuring the topography and deformation of the earth (Hanssen, 2001). Interferograms, which are generated from the phase difference of two radar images acquired either by two different antennas or using repeated acquisitions (Zebker et al., 1994; and Hanssen, 2001), are able to detect small deformations in the ground surface elevation over large areas with very high accuracy (1cm or less). Interferometry, an idea that was based on the wave front concept developed by Christiaan Huygens in 1690 as stated by Hanssen, underwent a spectacular increasing array of applications in the field of geophysics since the late 80's. These applications can be categorized in roughly four disciplines (Hanssen, 2001):

1. Topographic mapping with a relative accuracy of 10-50m
2. Deformation mapping with mm-cm accuracy
3. Thematic mapping based on change detection
4. Atmospheric delay mapping with mm-cm accuracy in terms of the excess path length

The formation of sudden collapses and subsidence due to the instability of Karst has caused tremendous losses in both human lives and structures all around the world. One can only imagine the possible far-reaching scientific, technical and societal beneficial outcomes of using such a method for studying and maybe identifying areas that are prone to future collapses or subsidence. A thorough understanding of the principles of the technique is vital at this stage and is also important particularly for the analysis, interpretation, and handling of the interferometric data. This chapter reviews the basic concepts of SAR interferometry starting with an explanation of Synthetic Aperture Radar (SAR) in general followed by a review of past SAR missions, and a short description of the basic components of a typical SAR instrument. A major part of this chapter focuses on SAR interferometry processing, it self, by reviewing past work and discussing the methodology and principals of interferometry. Phase observations, topographic height, and surface deformation will also be discussed.

4.2. Synthetic aperture radar

Radio detecting and ranging (radar) refers to a technique and an instrument that emits electromagnetic pulses in the radio and microwave regime, as can be seen in Figure 4.1, and detects the reflections of these pulses from objects in its line of sight (Hanssen, 2001), see Figure 4.2. The techniques use both two-way travel time of the pulses and backscatter intensity in determining the distance to the detected object and inferring physical quantities representatively. Physical quantities such as the size or surface roughness of the detected object can be inferred (Figure 4.3).

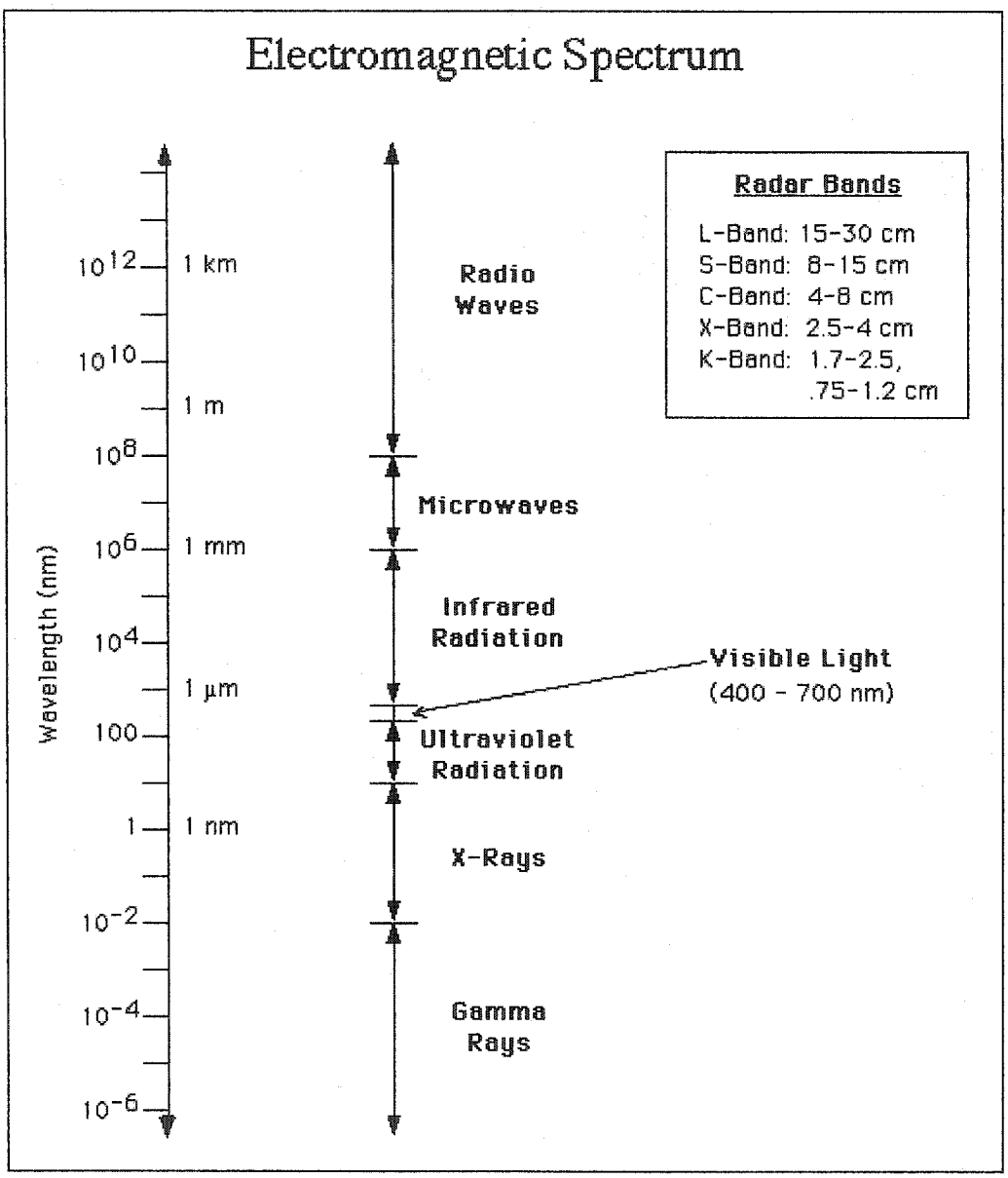

Figure 4.1: Electromagnetic spectrum and radar bands
(Source: After Alaska SAR Facility, 1996)

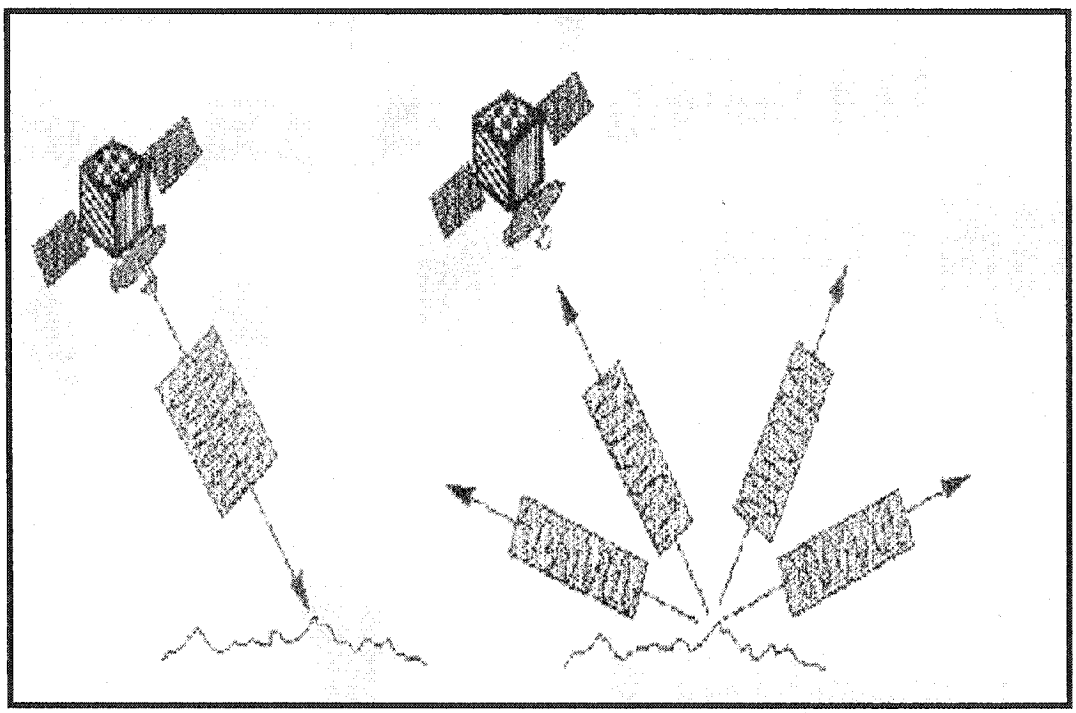

Figure 4.2: Radar transmits a pulse and measures reflected echo (backscatter)
(Source: After Freeman, 2000)

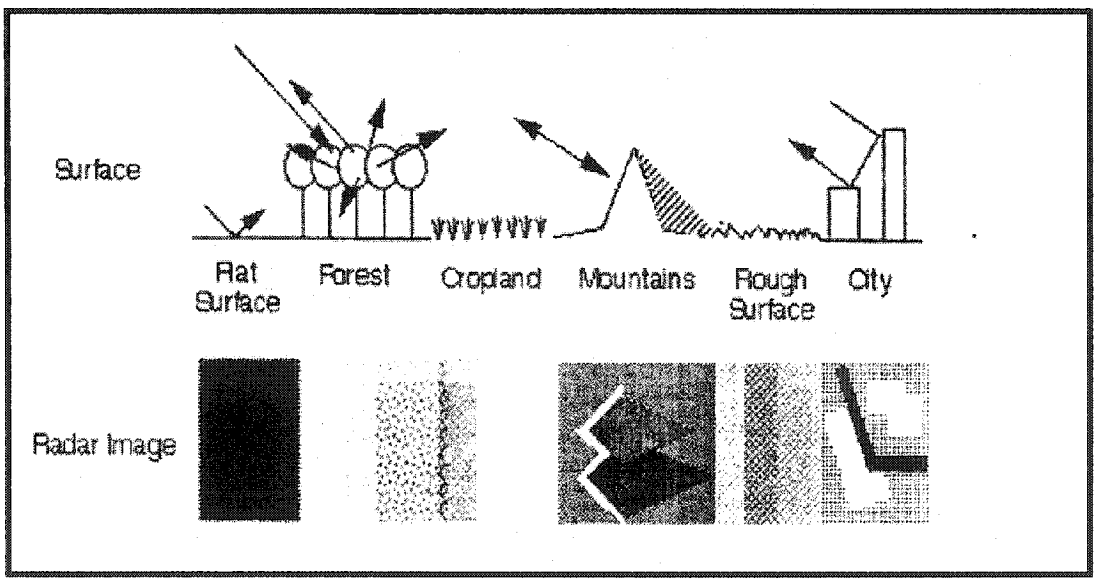

Figure 4.3: Imaging different types of surface with radar
(Source: After Freeman, 2000)

Synthetic Aperture Radar (SAR), an imaging radar system, is one of the most advanced engineering inventions of the twentieth century (Soumekh, 1999). In 1951 an invention in radar by Carl Wiley followed by developments at the universities of Illinois and Michigan in the late 50's and early 60's revolutionized the way of the construction of human-made vision systems and culminated in the concept of the synthetic aperture radar (Soumekh, 1999; and Hanssen, 2001). The basic idea behind SAR, as Soumekh stated, is to synthesize the effect of large-aperture physical radar, whose construction is considered infeasible. This large-aperture physical radar is synthesized by combining the information of many received pulse returns within the synthetic antenna length, which is created by using a moving antenna (Figure 4.4). This process leads to a really large increase in azimuth resolution as can be seen in Figure 4.5. The key factor for these advances is the coherent radar, where phase thats behavior needs to be stable within the period of sending and receiving the signal, as well as amplitude are received and preserved for later processing (Hanssen, 2001).

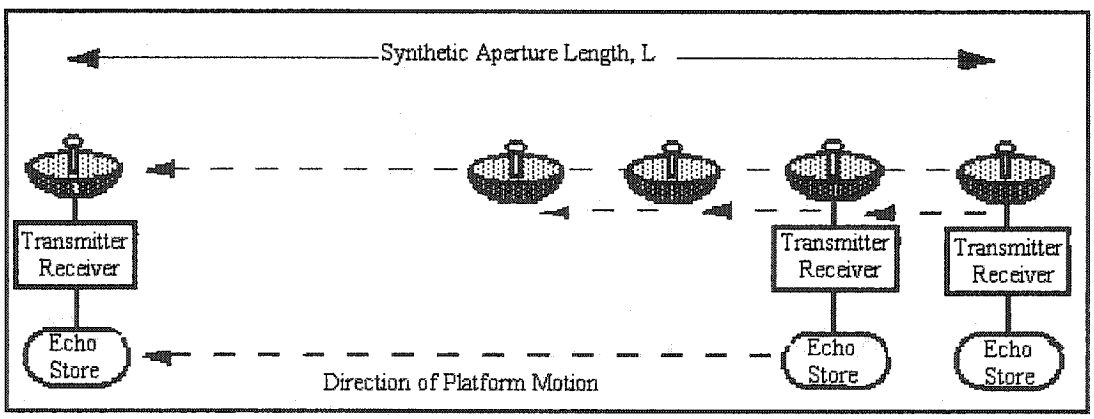

Figure 4.4: Constructing a synthetic Aperture Radar
(Source: After Freeman, 2000)

The coherent deformation of the earth's surface within the radar's swath can be observed as a fraction of the radar's wavelength, resulting in a sub-cm ranging accuracies in the radar line-of-sight (Hanssen, 2001).

This outstanding imaging radar invention, which operates in the microwave region of the electromagnetic spectrum that provides improved signal penetration, decreased attenuation and especially that of atmosphere, was able to overcome previous satellite remote sensing method's limitations. The improvement lies in the fact that the active radar observations can be collected at nighttime, can operate generally independent of weather conditions, and is not affected by cloud cover or haze (Soumekh, 1999; and Hanssen, 2001).

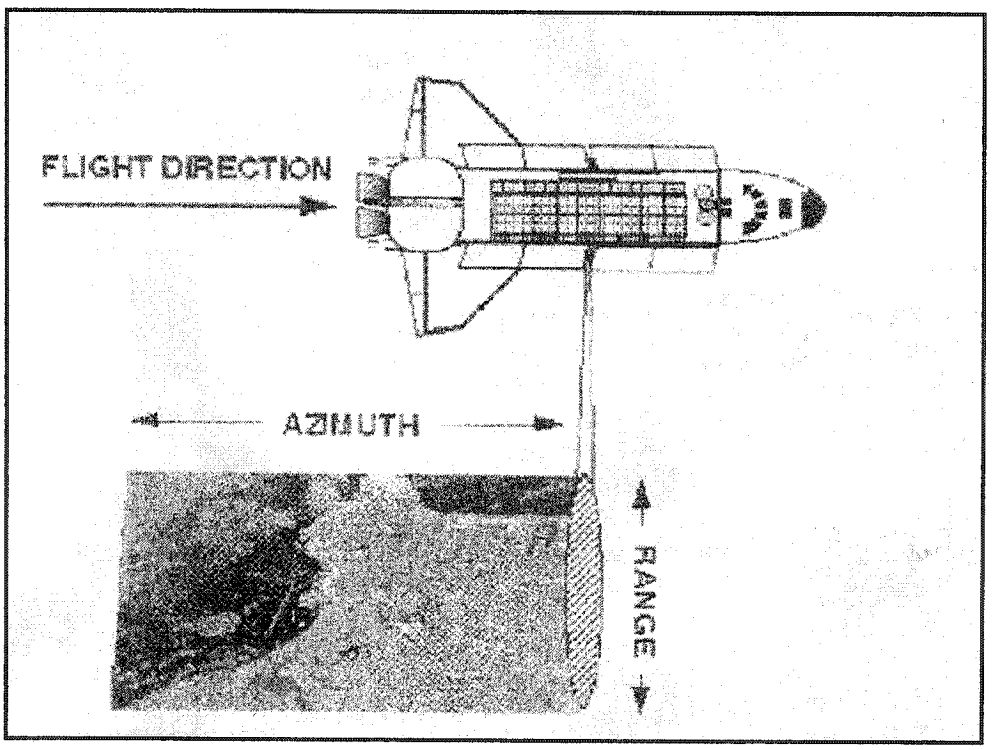

Figure 4.5: Building up a radar image using the motion of the platform (Source: After Freeman, 2000)

4.3. Review of past SAR missions

Starting from 1981 and due to the success of tests performed on mainly airborne SAR systems, many space shuttle missions carried Synthetic Aperture Radars on board (Table 4.1). One such outstanding result was that of the L-band SAR system on board of Seasat satellite that was launched mid 1978 for ocean studies, a mission that resulted in splendid SAR imagery and thus enabled SAR systems to be included in many future satellites (Elachi et al., 1982; and Hanssen, 2001).

Satellite	λ (cm)	Incidence Angle (degree)	Look Angle θ (degree)	Hsat (km)	Repetition Cycle (days)	Polarization	Bandwidth, BR Δf (MHz)	Frequency, f0 (GHz)	Width of antenna, Wa (m)	Length of antenna, La (m)	Effective Range Resolution, δr (m)	Effective Azimuth Resolution, δa (m)
SEASAT	23.5	23	20-26	800	3	HH	19	1.275 (L-Band)	2.2	10.7	7.88	5.4
SIR-B	23.5	15-64	15-64	235	8.3	HH	12	1.282 (L-Band)	2.16	10.7	12.5	5.4
SIR-C	23.5, 5.8, 3.1	15-45	15-45	225	1	HH-VH-HV-VV	10,20,30	1.24 (L-Band) 5.285 (C-Band) 9.6 (X-Band)	3.7	12	12,7.5,5	6
ALMAZ	10.0	30-60	30-60	300	-	HH	Uncoded	3.00 (S-Band)			10-30	
ERS-1	5.66	23	21-26	790	3,35,168	VV	15.55	5.3 (C-Band)	1	10	9.6	5
ERS-2	5.66	23	21-26	790	35	VV	15.55	5.3 (C-Band)	1	10	9.6	5
JERS-1	23.5	39	26-41	568	44	HH	15	1.275 (L-Band)	2.4	11.9	10	6
RADARSAT	5.66	20-49	20-49	792	24	HH	11.6,17.3, 30	5.3 (C-Band)	1.5	15	13,8.66,5	7.5
SRTM	5.66, 3.1	52	52	233	35	HH-VV	9.5	5.3 (C-Band) 9.6 (X-Band)	4	12	15.77	6
ALOS (PALSAR)	23.6	8-60	8-60	700	45	HH-VV-HH-HV-VV-VH	28,14	1.270 (L-Band)	3	9	5.4, 10.7	4.5
ENVISAT	5.66	20-50	20-50	800	35	HH-VH-HV-VV	14	5.3 (C-Band)	4	10	10.7	5

Table 4.1: List of satellite SAR missions with their most important design parameters

One of the first instruments used was the SIR-A, a shuttle imaging radar (SIR) laboratory L-band system, which operated for 2.5 years and provided spectacular data recorded analogously on tapes. SIR-B, an improved version of SIR-A, orbited the earth in 1984 with the ability to steer its antenna mechanically achieving different look angles with full digital data recording (Hanssen, 2001).

The former Soviet Union launched the first S-band SAR system, Cosmos-1870 in 1987 followed by another SAR system, ALMAZ-1, which was launched in 1991. Both systems operated for a period close to two years. ERS-1, the first SAR European remote sensing satellite, and ERS-2 were launched by the European Space Agency (ESA) in 1991 and 1995 representatively. ERS-1, the five year life satellite kept operating for nine years and thus enabled a so-called "tandem-mode", which is the operation of two satellites at the same time and orbit, when it kept operating for nine months following ERS-2 in the same orbit (Hanssen, 2001).

The L-band Japanese Earth-Resources Satellite (JERS) was launched in 1992 and operated for almost six years resulting in acquisitions better suited for repeat-pass interferometric applications.

SIR-C/X-SAR, a combined system developed in 1994 by NASA's Jet Propulsion Laboratory (JPL), the German Aerospace Center (DLR), and the Italian Space Agency (ASI) orbited the earth in different seasons to detect seasonal differences in the generated images under three different frequencies, an L-band, C-band, and X-band. This combination of different frequencies extended and improved the interpretation of the data significantly (Lanari et al., 1996; and Cotelli et al., 1996).

In 1995, Rdarsat, a SAR satellite system with ScanSAR mode, a system that can acquire wide swaths, was launched by the Canadian SPACE agency (CSA) with limited orbit control and maintenance and thus restricted its interferometric capabilities. One recent SAR satellite mission, Shuttle Radar Topography Mission (SRTM), was launched in 2000 using single pass configuration with two antennas. This system was able to overcome some previous repeat pass mission problems related to topography mapping (Hanssen, 2001). The European Space Agency (ESA) launched the most recent SAR satellite mission, EnviSAT, in March of 2002, a polar-orbiting earth observation satellite that provides measurements of the atmosphere, ocean, land, and ice. This satellite has an ambitious and innovative payload to insure the continuity of the data measurements of ESA's satellites ERS-1 and ERS-2.

4.4. SAR components

The block diagram in Figures 4.6 shows the basic SAR system configuration, while Figure 4.7 defines the nomenclature used in SAR systems.

A transmitter generates a periodic RF waveform, which could either be a simple sequence of short pulses, or has rather more complicated structure. An antenna is used to both radiate the RF waveforms as EM wave and receive the reflected waves as well. Each SAR system also includes a receiver, which is used to detect and amplify the reflected signal emerging from the antenna. A signal storage matrix capable of preserving the time delay structure for each reflected pulse is used, where this information is required to provide range resolution.

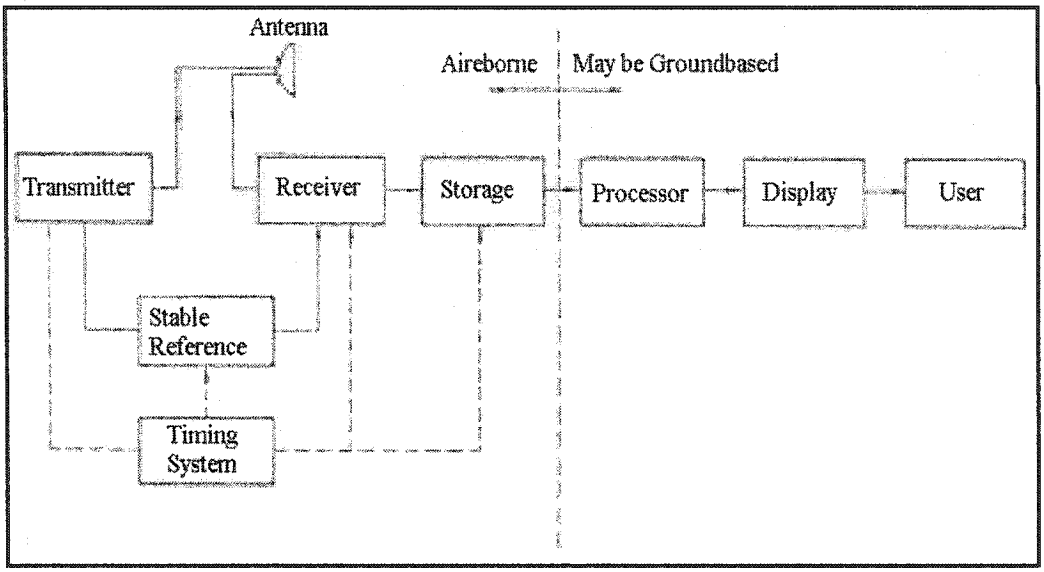

Figure 4.6: Basic SAR functional diagram
(Source: After Reeves, 1975)

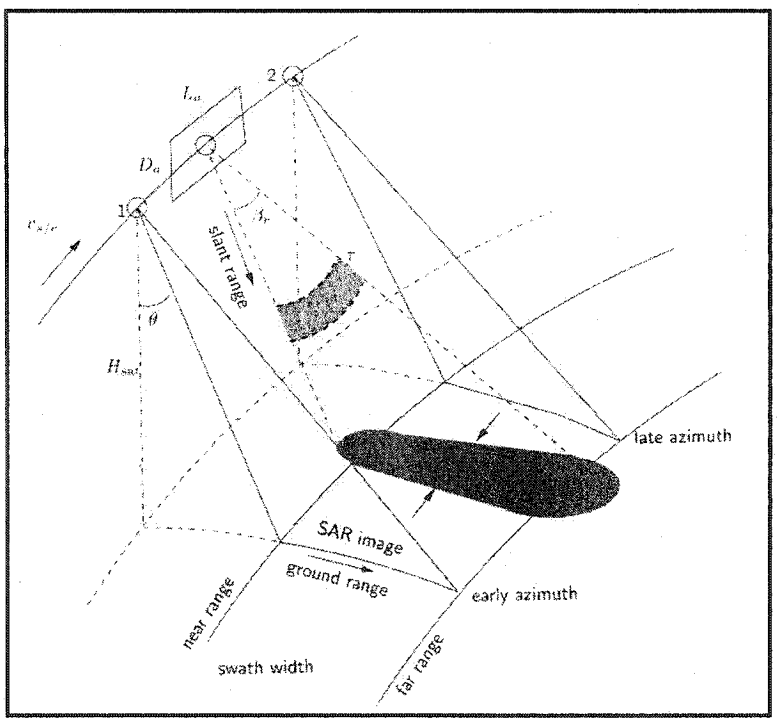

Figure 4.7: Nomenclature for SAR
(Source: After Hanssen, 2001)

This storage matrix must also be capable of storing a sequence of reflected pulses sufficiently to permit adequately long synthetic arrays to be performed (Reeves, 1975). A SAR system also includes a signal processor, which can accept signals from the storage matrix and affect the required processing without causing loss of range-dimension structure. A display device is also needed to present the output of the signal processor to the user.

Finally, each SAR system includes a timing system, which is required to synchronize the functions of all the other elements of the system. The above-mentioned basic SAR system elements are all interconnected as can be seen in Figure 4.6. Although all SAR system components can be found in the aircraft or spaceship, both the processor and display unit are usually ground based. The following sections explain in more details the calculations used in SAR system components.

4.4.1. Emitter

Echoes from each short, high-energy microwave pulses emitted by radars to the earth are recorded. A pulse is triggered and transmitted by the control systems. Shape of the pulse, amplitude and modulation characteristics can be written for the i^{th} pulse (Henderson and Lewis, 1998):

$$P_T^{1/2}\, p(t)\sin(\omega_0 + \varphi_i^T) \tag{4.1}$$

Where,

$P_T^{1/2}$ = Peak power of transmitted pulse

p (t)= amplitude weighting of pulse, including envelope and pulse modulation

ω_0 = Radar carrier frequency (radians/sec)= $2\pi f_0$ where $\lambda f_0 = c$ is the speed of light

And φ_i^T = reference phase of the transmitted signal.

4.4.2. Receiver

The antenna transmits an electromagnetic (EM) field that radiates and illuminates the scene and re-radiates towards the radar following a simple function of Γ, of the incident field and can be expressed as (Henderson and Lewis, 1998):

$$E_B = \Gamma(R, \varphi)\, E_I \tag{4.2}$$

Where, E_I = The incident field

E_B = The backscattered field

R, φ = The range and azimuth from the radar position

The magnitude of Γ represents the efficiency of the field reflection whereas the phase of Γ represents the phase shift during reflection.

Both the extremely weak EM field (10^{-11} orders of magnitude smaller than the energy of the emitted pulse) and the signal reaching the receiver have to be amplified to produce a more useful level and separated from the background noise representatively (Henderson and Lewis, 1998).

4.4.3. Demodulator

Demodulation, a simple frequency shift, is an important process where carrier frequency is removed as the information of interest lies in the envelope and phase of the received signal rather than the carrier frequency itself. In this process, the received signal is multiplied by a carefully controlled sinusoidal signal resulting in

the creation of two versions of receiver output (Henderson and Lewis, 1998). The first version is centered at the receiver carrier and demodulator frequency whereas the second version is centered at their difference frequency (Henderson and Lewis, 1998). The signal component centered at the difference frequency is the only one selected by the demodulator. Quadrature demodulation is usually used as a modulation method (Henderson and Lewis, 1998).

4.5. SAR interferometry

One capability that remained out of reach for radar is the measurements of angles. This limitation was overcome by interferometry, an idea of using phase information of two SAR images acquired either by two different antennas or using repeated acquisitions (Figure 4.8). This simple idea made obtaining distances as well as angular measurements by a SAR system possible. Single-pass or repeat pass interferometric configurations, which will be explained later in this section, can be used as stated by Hanssen (2001), where the former configuration uses two physical antennas to collect the radar echoes and generate elevation observations with accuracies in the order of 6 meters for space borne sensors, whereas the later configuration uses two radar images that are acquired by a single antenna revisiting the area after a specific time interval and thus observe dynamic processes. The use of the phase measurements (multiplicative interferometry) enabled the observation of relative distances as a fraction of the radar wavelength, and the difference in the sensor locations enabled the observation of angular differences, necessary for topographic mapping (Hanssen, 2001).

Interferometry can be divided into two distinct types, additive and multiplicative as can be seen in Figure 4.9. Additive interferometry signals (amplitude fringes) are obtained by the coherent summing of the amplitudes of two input signals, whereas multiplicative interferometry interferometric phase is obtained by coherent cross-multiplication of the two input signals.

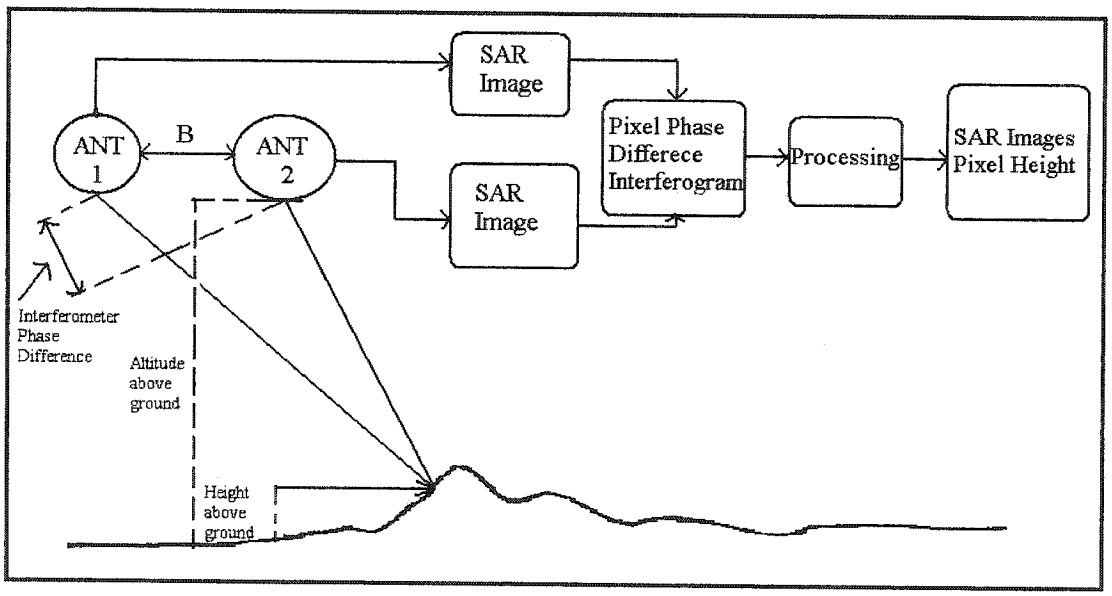

Figure 4.8: The basic imaging geometry with image processing for SAR Interferometry
(Source: Modified after Shields, 1997)

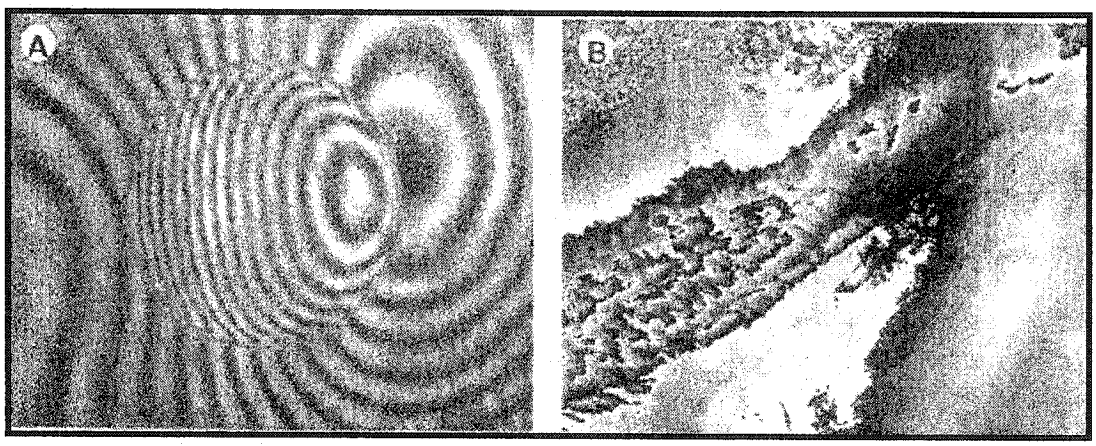

Figure 4.9: The two types of interferometry. (A) Additive interferometry (Amplitude fringes) of fluid thickness observed by laser illumination (Courtesy M. Decre, Philips Research Laboratories). (B) Multiplicative interferometry (Phase fringes) for topographic mapping.
(Source: After Hanssen, 2001)

Additive interferometry suffers from a couple of disadvantages in the sense that it is considered impossible to determine whether the interferometric signal is increasing or decreasing, moreover, the accuracy is only a fraction of the amplitude cycle and thus is often not very accurate. On the other hand, multiplicative interferometry gives more accurate results, as the determination of the fraction of the phase cycle is considered somehow easier.

4.5.1. Methods for acquiring SAR interferometry data

Three methods are available and can be used for gathering SAR Interferometry data; across track interferometry, along track interferometry, and repeat pass interferometry. Each method is developed to capitalize on the strengths of the sensor as well as the application for which the data is acquired (Shields, 1997).

The first method, across track interferometry, uses two antennas mounted on an aircraft in a position perpendicular to the flight path allowing the sensors to gather information on the height of targets (Figure 4.10). Using this method allows the capturing of data in a single pass due to the availability of two antennas on the aircraft, where the first antenna sends and receives signals where as the second antenna is used to receive data only. A distance referred as the baseline, which has a great affect on the SAR performance, separates the two antennas. This distance should carefully be calculated as too long baselines results in uncorrelated return wavelengths. The length of baseline also affects the interferometric scale factor, which defines the amount of phase shift for a given height (Shields, 1997).

This method of SAR Interferometry data acquisition is suitable for the creation of Digital Elevation Models (DEM) and topographic mapping.

Along track interferometry, another method used for acquiring SAR interferometry data, is similar to across track interferometry method in the sense that it requires two antennas mounted on an aircraft. However, this method of data acquisition requires the antennas to be mounted in a position parallel to the flight path direction as can be seen in Figure 4.11. This position enables the sensors to acquire horizontal data, which are very useful for velocity measurements. Across track and along track interferometry can also be referred to as single pass interferometry.

Repeat pass interferometry, the third and most recent technique available for SAR interferometry data acquisition, adopts a single antenna and thus is suitable for mounting on satellites and space shuttles. As apposed to the two previously interferemetric data acquisition methods, where multiple images are acquired from the same wavelength, this method capture images of the area at differing times or slightly different incident angles. Here, the baseline is referred to the difference in the satellite positions. Data acquired using repeat pass interferometry are considered ideal for use in measuring land deformation and change detection. The geometry of repeat pass interferometry is illustrated in Figure 4.12 below.

Some main points of SAR interferometry principles and previous studies were described in Reeves (1975); Franceschetti and Lanari (1999); Soumekh (1999); and Hanssen (2001) and hereafter summarized in the following sections.

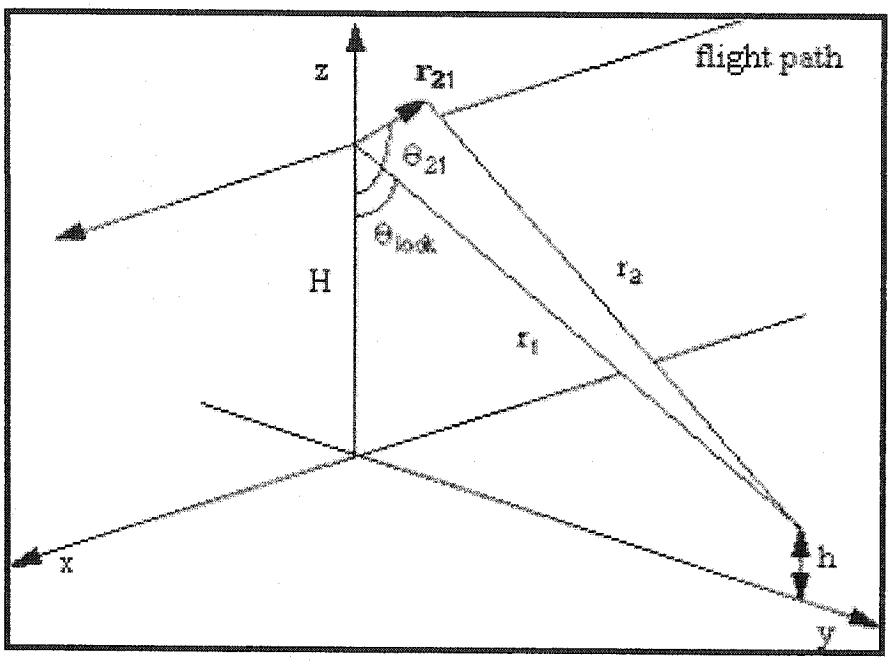

Figure 4.10: Across track interferometry geometry
(Source: After Shields, 1997)

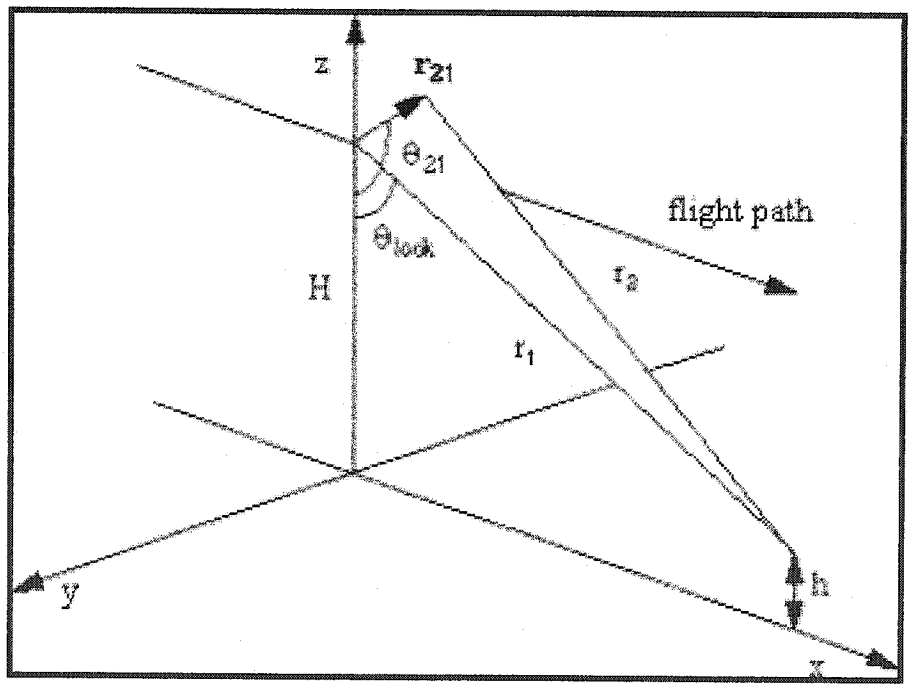

Figure 4.11: Along track interferometry geometry
(Source: After Shields, 1997)

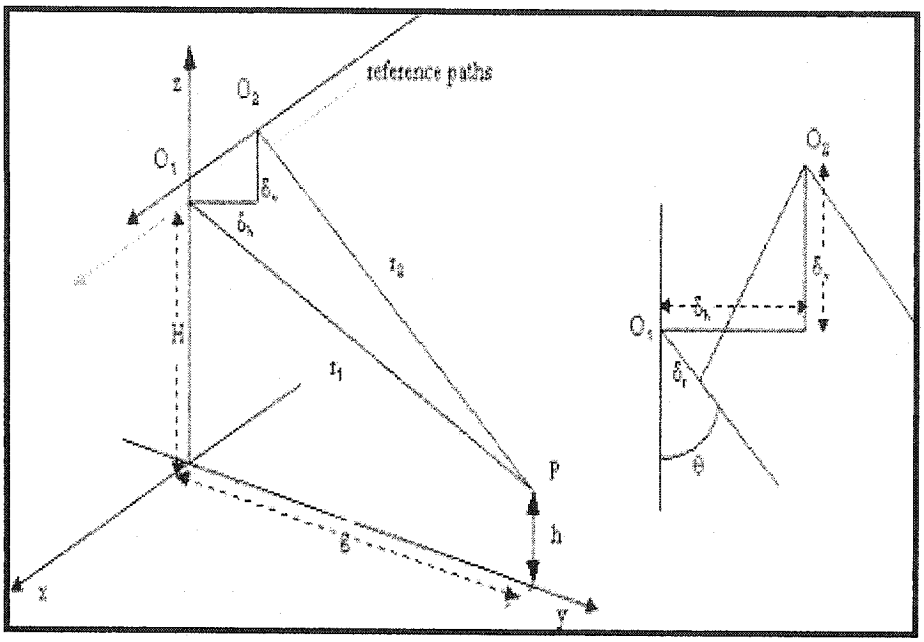

Figure 4.12: Repeat pass interferometry geometry
(Source: After Shields, 1997)

4.5.2. Overview of past work and differential SAR interferometry methods

In 1946, after the Second World War, radio interferometry developed when Ryle and Vonberg constructed the first radio analog of the Michelson-Morley interferometer and was soon able to locate a number of cosmic radio sources (Tubbs, 1997). This was followed by developments in the field of planetary mapping, where the range-Doppler configuration enabled the mapping of radar reflectivity from iso-range lines and iso-Doppler lines (Evans and Hagfors, 1968). Rogers and Ingalls solved ambiguity between reflections from the northern and southern hemispheres of the planet, which remained unknown, in 1969 by using two antennas interferometry for the first time. Ziks (1972) later used the antennas small beam width in measuring elevation differences using interferometry.

The U.S. military were the first to perform airborne radar (SAR) experiments for topographic mapping, when a patent for obtaining elevation from phase difference images was filed in 1971 (Richman, 1982; and Henderson and Lewis, 1998). Graham published the first results of this method using two antennas and coherent additive interferometry with optical processing techniques in 1974. On the other hand, two antennas single pass airborne interferometry with digital image processing and coherent multiplicative interferometry matured in the 80's with first results published by Zebker and Goldstein in 1986.

These applications of interferometry are still used by various researchers since its development after the Second World War with topography estimation being the main focus, and thus yielding elevation accuracies comparable with optical methods with the valuable advantage of working in all weather conditions (Table 4.2). Nevertheless, the experiments with the repeat-pass configuration and the use of differential interferometry clearly demonstrated an even more spectacular application, deformation monitoring (Hanssen, 2001).

Differential interferometry is a technique that requires the comparison of two interferograms and thus involves the use of either a third data set from repeat pass interferometry or an accurate DEM from an external resource.

Some most recent interesting experiments using this method with satellite data were carried out in the 80's and 90's and resulted in mainly three methods of generating differential interferograms used in detecting very small ground surface changes.

Location	Reference
Earthquakes	
Kobe, Japan	Ozawa et al. (1997)
Landers earthquake, California	Massonnet et al. (1993); Massonnet and Adragna (1993); Zebker et al. (1994); Peltzer et al. (1994); Massonnet et al. (1994); Feigl et al. (1995); Peltzer et al. (1996); Massonnet et al. (1996b); Hernandez et al. (1997); Price and Sandwell (1998); Michel et al. (1999)
Hector earthquake, California	Sandwell et al. (2000)
Manyi earthquake, Tibet	Peltzer et al. (1999)
Izmit earthquake, Turkey	Barbieri et al. (1999); Hanssen et al. (2000a); Reilinger et al. (2000)
Eureka valley, California	Massonnet and Feigl (1995b); Peltzer and Rosen (1995)
Northridge earthquake, California	Massonnet et al (1996a); Murakami et al. (1996); Kawai and Shimada (1994)
Kagoshima-kenhokuseibu earthquake, Japan	Fujiwara et al (1998)
Nuweiba earthquake, Gulf of Elat (Aqaba)	Baer et al. (1999); Klinger et al. (2000)
Grevena earthquake, Greece	Mayer et al. (1996); Clarke et al. (1996)
Colfiorito, Umbria-Marche, Italy	Stramondo et al. (1999)
Creep San Andreas fault/Parkfield	Rosen et al. (1998); Burgmann et al. (2000b)
Volcanoes	
Vatnajokull, Iceland	Roth et al. (1997); Thiel et al. (1997)
Keafla spreading segment, Iceland	Sigmundsson et al (1997)
Etna, Italy	Massonnet et al (1995); Briole et al. (1997); Delacourt et al (1997); Lanari et al. (1998); Williams and Wadge (1998)
Iwo Jima, Japan	Ohkura (1998)
Izu peninsula, Japan	Fuliwara et al. (1998)
Katmai, Alaska	Lu et al. (1997); Lu and Freymueller (1999)
Kilauea, Hawaii	Mouginis-Mark (1995a); Rosen et al. (1996); Zebker et al. (1996,1997)
Soufriere Hills, Montserrat	Wadge et al (1999)
Campi Flegrei, Italy	Usai et al. (1999); Avallone et al. (1999)
Yellowstone caldera, Wyoming	Wicks et al. (1998)
Piton de la Fournaise, Reunion	Sigmundsson et al (1999)
Long Valley, California	Thatcher and Massonnet (1996)
Unzen, Japan	Fujii et al. (1994)
Galapagos	Mounginis-Mark (1995a); Jónsson et al. (1999); Amelung et al. (2000a)

Table 4.2: Major geophysical events studied using radar interferometry, and main references
(Source: After Hanssen, 2001)

Location	Reference
Induced Subsidence/Uplift	
Geothermal fields	Massonnet et al. (1997); Hanssen et al. (1998a); Jónsson et al. (1998); Carnec and Fabriol (1999); Fialko and Simons (2000)
Las Vegas, Nevada	Amelung et al. (1999)
Paris, France	Fruneau et al. (1998)
Napels, Italy	Tesaur et al. (2000)
Antelope Valley, California	Galloway et al. (1998)
Gardanne, France	Carnec et al. (1996)
Pomona, California	Ferreti et al. (2000)
Groningen, Netherlands	Hanssen and Usai (1997); van Bree et al. (2000)
Imperial Valley, (swelling), California	Gabriel et al. (1989)
Glacier/Ice Motion	
Antarctica/Patagonia	Goldstein et al. (1993); Hartl et al. (1994a,b); Wu (1996); Rott and Siegel (1997); Rott et al. (1998); Joughin et al. (1999)
Greenland	Joughin (1995); Kwok and Fhnestock (1996); Joughin et al. (1996); Rignot et al. (1997); Joughin et al. (1997); Mohr (1997); Mohr et al. (1998); Joughin et al. (1998);Hoen and Zebker (2000)

Table 4.2 continued: Major geophysical events studied using radar interferometry, and main references
(Source: After Hanssen, 2001)

The first method was developed by Gabriel and Goldstein, where shuttle's SIR-B data was used first in 1988 in studying dynamic phenomenon and thus a method was proposed to measure very small (1 cm or less) surface motion with good resolution

(10 m) over large swaths (50 km) using SAR images (Gabriel and Goldstein, 1988; and Goldstein et al., 1989). Gabriel et al. (1989) method used two images made of a scene by simultaneously flying two physically separated antennas, or one antenna flown twice over the same track. The phase of corresponding pixels are later differentiated, and altitude is deduced from some simple computation and image rectification. This method was applied to a site in Imperial Valley, California, using Seasat data and was able to detect very small motion effects due to water-absorbing clays.

The second method, DEM Elimination (DEME), was developed in 1993 when SAR interferograms from the European ERS-1 satellite were first combined with digital elevation models (DEM) by Massonnet et al. (1993) to generate earthquake displacement maps. The interferogram used was generated using SAR images acquired before and after the earthquake where a Digital Elevation Model (DEM) was later used to remove topographical effects. This method was able to isolate the earthquake line- of-sight displacement field. The method was later further developed in 1994, achieving successful results and demonstrating that for a particular area data sets acquired more than one year apart were sufficiently correlated to form interferograms and suggested that the accuracy could be sacrificed in certain circumstances if atmospheric effects are ignored (Massonnet et al., 1994).

The third method, Double Difference (DD) or three-path method, suggested by Zebker et al. (1994), combines three SAR images in generating two pairs of interferograms where topographic as well as dynamic effects are separated and thus

displacement field is estimated using radar data alone. The results of this method were verified by comparing them with available Global Positioning Systems (GPS) data.

4.5.3. Principles of SAR interferometry

Although the basic module of Synthetic Aperture radars is considered the same, this radar can be found in many different configurations. The most important radar feature to enable SAR or Interferometric SAR is to be coherent within the time span between sending and receiving one pulse so as to retain the phase of the transmitted signal and use it as a reference against which the returned signal can be compared (Hanssen, 2001). Imaging radar interferometry uses complex SAR images generated using either one antenna or different antennas at different locations and time as was mentioned earlier. This high-resolution 2-D imaging radar is used to generate an interferogram that permits the determination of minute differences in the range, on the sub-wavelength scale, for corresponding points of an image pair.

The principles of SAR interferometry fall into two basic classes, spatial and temporal baselines, where multiple inteferograms can be combined with simultaneous spatial and temporal baselines. The baseline here is defined as the distance between two acquisition tracks and is denoted by "B" as was illustrated Figure 4.8.

The baseline is called " spatial baseline" when the measurement is simultaneous on these two tracks, which means that the transmission point is either from a common or separate point on each track. This type of baseline is used in terrain topography

estimations as it allows us to measure target elevations. Moreover, the baseline is called " temporal baseline" when the measurement is acquired from an exactly identical acquisition track at different times and thus helps in measuring changes in the observed scene between the periods of data acquisition using interferometric differencing. Both previous baselines can be used simultaneously resulting in a so-called " Mixed baseline".

4.5.4. Phase observation, topographic height, and surface deformation

This section summarizes the basic principle of interferometry topographic mapping. Although topographic height and surface deformation estimates are obtained using two-phase observations, differential interferometry can be used to improve the accuracy of those measurements. Following is the mathematical derivation of the basic two-phase interferometry used for topographic mapping and surface deformation estimations. Figure 4.13 defines all the variables used in the derivation. Both SAR images used to generate the interferogram are composed of a regular grid with complex values y1 and y2 as follows (Hanssen, 2001):

$$y1 = |y1| \exp(i\psi_1)$$

$$y2 = |y2| \exp(i\psi_2) \qquad (4.3)$$

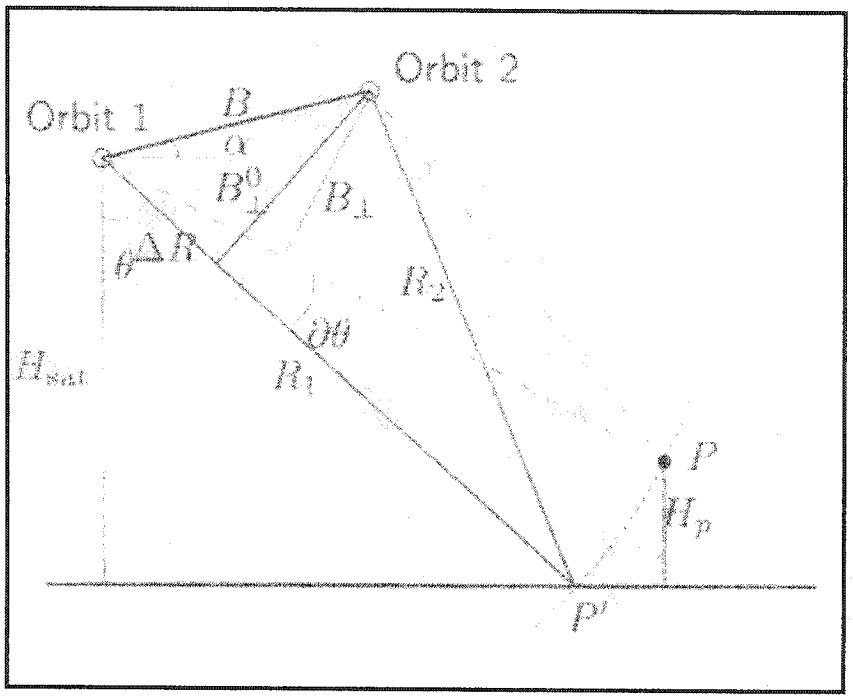

Figure 4.13: Interferometric configuration for height Hp
(Source: After Hanssen, 2001)

The y2 grid is aligned and resample to the corresponding locations in the y1 grid followed by a complex multiplication resulting in a complex interferogram:

$$\nu = y1\ y2^{*} = |y1||y2| \exp(i(\psi_1 - \psi_2)) \tag{4.4}$$

In the previous equation, $y2^{*}$ denote the complex conjugate of the value y2. For resolution cell P, both observed phase values of ψ_{1p} and ψ_{2p} in the two used images could be expressed as follows (Hanssen, 2001):

$$\psi_{1p} = -\frac{2\pi 2R_1}{\lambda} + \psi_{scat,1p}$$

$$\psi_{2p} = -\frac{2\pi 2R_2}{\lambda} + \psi_{scat,2p} \tag{4.5}$$

Here R_1 and R_2 represent the geometric distances, while $\psi_{scat,1p}$ and $\psi_{scat,2p}$ represent the scattering phases in both images. There are circumstances where the value of the scattering phases become the same ($\psi_{scat,1p} = \psi_{scat,2p}$), in this case the interferometric phase can be written as (Hanssen, 2001):

$$\phi_p = \psi_{1p} - \psi_{2p} = -\frac{4\pi(R_1 - R_2)}{\lambda} = -\frac{4\pi\Delta R}{\lambda} \tag{4.6}$$

With ΔR representing the path difference. The differentiation of ϕ_p can be expressed as follows:

$$\partial\phi p = -\frac{4\pi}{\lambda}\partial\Delta R \tag{4.7}$$

With the path length difference, $\Delta R = B \sin(\theta - \alpha)$ approximately, according to the far-field or parallel-ray approximation (Hanssen, 2001). It is not possible to derive ΔR from the geometry in Figure 4.13 due to the 2π ambiguities and orbit inaccuracies. However, the relation between the changes in ΔR and θ can be found using:

$$\partial\Delta R = B\cos(\theta^0 - \alpha)\partial\theta \tag{4.8}$$

Both Eq. (4.7) and Eq. (4.8) can be combined to obtain the relation between an interferometric phase change and the change in the look angle θ as follows:

$$\partial\theta = -\frac{4\pi}{\lambda}B\cos(\theta^0 - \alpha)\partial\theta \tag{4.9}$$

The interferometric phase change, which can be defined as the difference between the measured phase ϕ and the expected phase for the reference body ϑ derived from the orbit geometry, thus written as:

$$\partial\phi = \phi - \vartheta \tag{4.10}$$

As can be seen in Figure 4.13, the height of the satellite above the reference body can be expressed as:

$$H_{sat} = R_1 \cos\theta \tag{4.11}$$

The above equation is differentiated for a resolution cell P with range R_{1p} resulting in an expression of the relationship between changes in look angle θ due to height difference ∂H_{sat}, that can be expressed as (Hanssen, 2001)

$$\partial H_{sat} = -H_p = -R_{1p} \sin\theta_p^0 \partial\theta \tag{4.12}$$

Where Hp is the measured height for range resolution cell P, since both P and P' are in the same resolution cell.

Considering geometry and with the use of both equations (4.7) and (4.10), the relationship between both the height Hp, above the reference body, and the phase difference $\partial\phi p$ can be written as follows:

$$Hp = -\frac{\lambda R_{1p} \sin\theta_p^0}{4\pi B_{\perp,p}^0} \partial\phi_p \tag{4.13}$$

Where

$$B_{\perp,p}^0 = B\cos(\theta_p^0 - \alpha) \tag{4.14}$$

Here, the initial value θ_p^0 must be found for an arbitrary reference surface, for example a sphere or an ellipsoid. Using $\partial\phi_p = 2\pi$ in Eq. (4.13) yields the height of ambiguity, which is the amount of height change that leads to a 2π change in interferometric phase:

$$h_{2\pi} = \left| \frac{\lambda R_{1p} \sin\theta_p^0}{2B_{\perp,p}^0} \right| \tag{4.15}$$

The influence of topography, Hp, and surface displacement, Dp, on the interferometric phase differences relative to the reference body are then combined. From Eq.s (4.7), (4.8), and (4.13) we find (Hanssen, 2001):

$$\partial\phi_p = -\frac{4\pi}{\lambda}\left(D_p - \frac{B_{\perp,p}^0}{R_{1p}\sin\theta_p^0} H_p \right) \tag{4.16}$$

Since the measured interferometric phase is equal to the sum of the reference phase ϑ and the derivations:

$$\phi_p = \vartheta_p + \partial\phi_p \tag{4.17}$$

Where the reference phase, ϑ_p, is defined as:

$$\vartheta_p = \frac{4\pi}{\lambda} B \sin(\theta_p^0 - \alpha) \tag{4.18}$$

From all of the above, we can find that the measured interferometric phase is defined as (Hanssen, 2001):

$$\phi_p = \frac{4\pi}{\lambda}\left(B\sin(\theta_p^0 - \alpha) - D_p - \frac{B_{\perp,p}^0}{R_1 \sin\theta^0} H_p \right) \tag{4.19}$$

This equation implies that for an effective baseline, $B_\perp$, of 100 meters, a height difference Hp of 1 meter yields an interferometric phase difference of approximately 4.5 degrees, which is well below the noise level of some 40 degrees, and is therefore practically undetectable (Hanssen, 2001). However, in the differential case, change Dp of 1 cm in the range direction, yields a phase difference of 127 degrees, which is easily detectable (Hanssen, 2001).

4.6. Available interferometric software

Several interferometric software have been developed by different organizations, institutions, and companies, with the ability to form Single Look Complex SAR images from RAW radar data, and use a pair of them to generate an interferogram that can be used for deformation studies in a given area. Table 4.3 lists some of the available interferometric software. In this research, SAR and interferometric processing will be conducted using the Repeat Orbit Interferometry Package, ROI_PAC, a SAR processing and Interferometry software developed at JPL/Caltech. The algorithms and procedures implemented in ROI_PAC, wrote by many contributors, which was initially developed at JPL in the 1980 and first released outside JPL and Caltech in 2001, will be thoroughly explained and discussed in chapter 6 of this dissertation. This particular package was chosen for the following reasons:

1- One software capable of generating Single Look Complex (SLC) SAR images from RAW SAR data, as well as use a pair or three of such images to generate interferograms of the study area.
2- Available in public domain and offer a free academic license.
3- Capable of performing both two-pass and three-pass interferometric techniques.

The package can perform interferometric processing by either using a pair of ERS SAR images and a Digital Elevation Model (DEM) to remove phase due to topography, or a set of three SAR images. Two-pass SAR interferometry with Digital Elevation Model Elimination (DEME) approach suggested by Massonnet and others, 1993, will be used as the interferometric analysis method, where an already available Digital Elevation Model (DEM) will be acquired and used to estimate and remove the topographic signal. This method was chosen for the following reasons:

1- USGS DEM's are easily obtained and readily available.
2- ERS SAR radar data are very expensive and thus limits the data that can be purchased for this research.

Chapter 7 of this dissertation will involve using the chosen Interferometric package and technique to generate an interferogram of a subsidence case study. The chapter will also include a thorough interferometric analysis of the study area.

Software Package	Description	Developer
Differential Interferometric Automated Process Applied to Survey Of Nature (DIAPASON)	Creates of all kinds of interferometry products (Interferometric phase images, Differential interferometric phase images, Coherence images and Coregistered amplitude images) from raw data or complex images (SLC) from ERS-1, ERS-2, JERS-1, RADARSAT and ENVISAT satellites.	French Space Agency (CNES) 1992
FOCUS™ PHASE™	1- Capable of ingesting raw data and producing Single Look Complex (SLC) SAR images 2- Includes algorithms for phase unwrapping, interpolation, height model generation and differential interferometry	VEXCEL Corporation 1993
Earthview APP ® Earthview InSAR ®	1- Offers a full choice of SAR processing algorithms and parameters and is capable of utilizing multiple CPU's for increased throughput. 2- Produces digital elevation models and height change maps through the use of repeat-pass SAR interferometry.	Atlantis Scientific Inc. 1995
Modular SAR Processor (MSP) Interferometric SAR Processor (ISP)	1- Allows the generation of complex and real valued SAR images from raw data of the current spaceborne and airborne sensors. 2- Generation of interferometric products starting with complex SAR data as the Single Look Complex (SLC)	GAMMA Remote Sensing 1995
Delft Object Oriented Radar Interferometric Software (Doris)	Capable of processing Single Look Complex (SLC) SAR images to the basic interferometric products (e.g. coherence maps, phase images)	Delft University of Technology 1998
Repeat Orbit Interferometry Package (ROI_PAC)	Uses raw radar data and digital elevation models (DEM; externally provided or interferometrically derived) to produce a variety of derived data products (e.g. full resolution images, interferograms, phase images, DEMs, and error estimates)	JPL/Caltech 2001

Table 4.3: Interferometric Software

4.7. Generating an interferogram example

At this stage, generating an interferogram example of an affected area where ground surface deformation has occurred, due to either an earthquake or subsidence for example, will help in demonstrating the effectiveness of this technique in detecting and thus studying very small ground surface deformations. The generation of this example will also aid in understanding the aspects of the proposed technique.

4.7.1. Example overview

Two-pass SAR interferometry with Digital Elevation Model Elimination (DEME) approach suggested by Massonnet and others, 1993, will be used as the interferometric analysis method, where an already available Digital Elevation Model (DEM) will be required and used to estimate and remove the topographic signal. SAR and interferometric processing will be conducted using the Repeat Orbit Interferometry Package, ROI_PAC, a SAR processing and Interferometry software developed at JPL/Caltech. Two synthetic Aperture Radar (SAR) images of the same area on the ground acquired at different dates, in order to detect any ground deformation that might have occurred during the intervening period, are required to generate the interferogram.

Raw SAR data acquired from the European Space Agency's (ESA) ERS-1 or ERS-2 satellites will be used to generate the two required images which are later used to generate the interferogram. The ERS raw data will be processed using ROI_PAC to generate two full resolution Single-Look Complex (SLC) SAR images. Two quantities are associated with each pixel on the SLC SAR image, Amplitude,

representing the backscatter amplitude and phase, equal to the sum of the two-way propagation phase delay. The two SLC produced images will then be registered to common reference geometry where mapping of pixel locations of common features from one image to the other, accounting for shifts and distortion of the source images arising from the geometry and inherent system limitations, is determined (Burgmann et al., 2000). At this point, an interferogram can be generated by resampling one of the complex images to match the other according to the co-registration prescription followed by multiplying each complex pixel of the first image by the complex conjugate of the same pixel in the second image. The interferogram is then a complex image itself, the phase of which is the difference of the signal phases that records the topography and deformation accumulated between observation times (Burgmann et al., 2000). The phase of the interferogram must be unwrapped at this stage so as to reduce the resultant phase to a geophysical observable. From orbit knowledge and the DEM acquired, a topography-only interferogram must be simulated and used to remove the topography from the desired interferogram. The resultant phase difference can then be further processed to map ground deformation over large areas (Mayer and Lu, 2001). Figure 4.14 shows the schematic of steps involved in processing SAR data from interferometric applications.

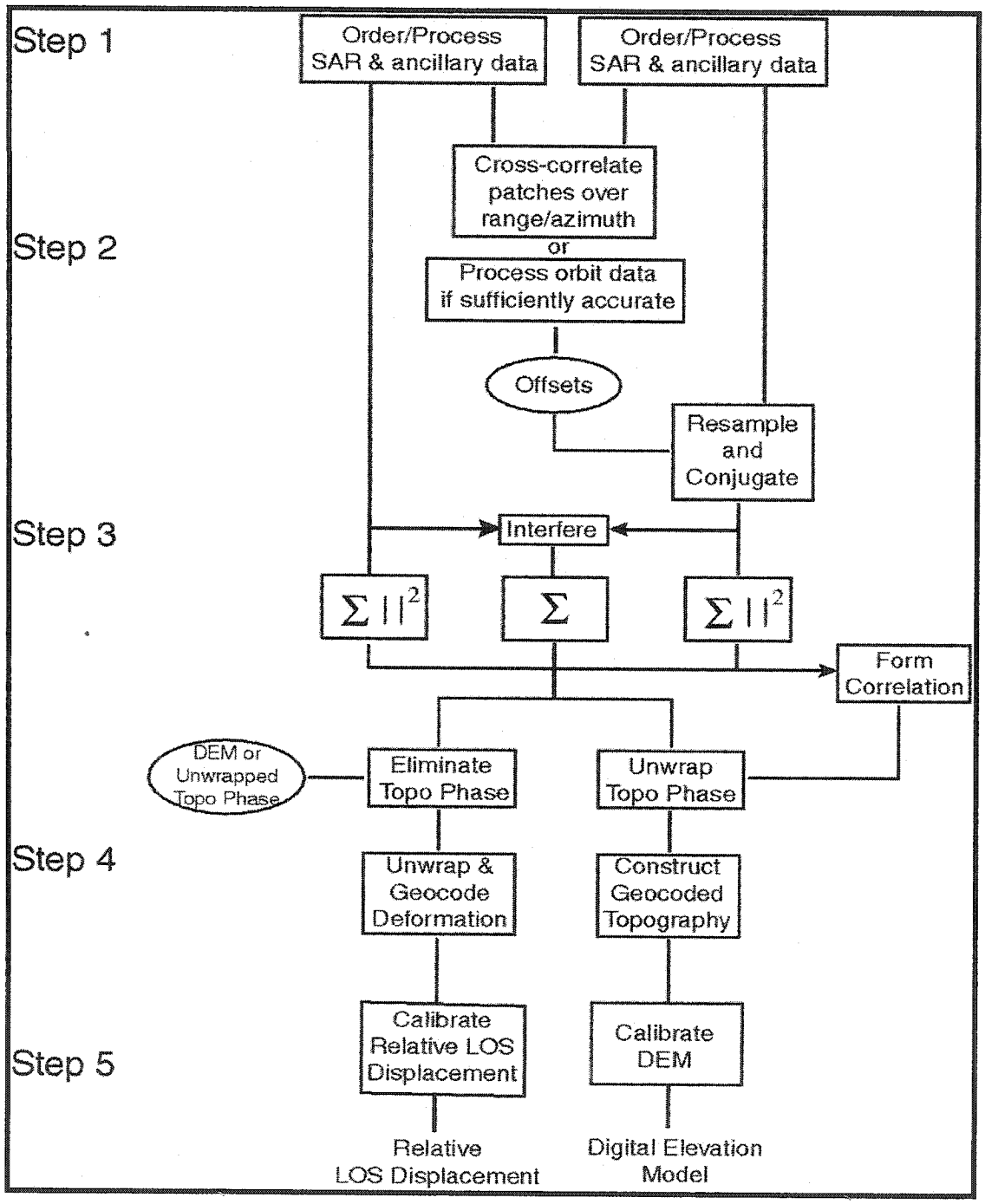

Figure 4.14: Schematic of steps in processing SAR data for interferometric applications
(Source: After Burgmann et al., 2000)

4.7.2. Example results

European Space Agency (ESA) Spaceborne Synthetic Aperture Radar (SAR) images of the Grabens region of Canyonlands National Park, an area located near the center of Colorado Plateau in Southeastern Utah (Figure 4.15), were used to generate the interferogram in this example.

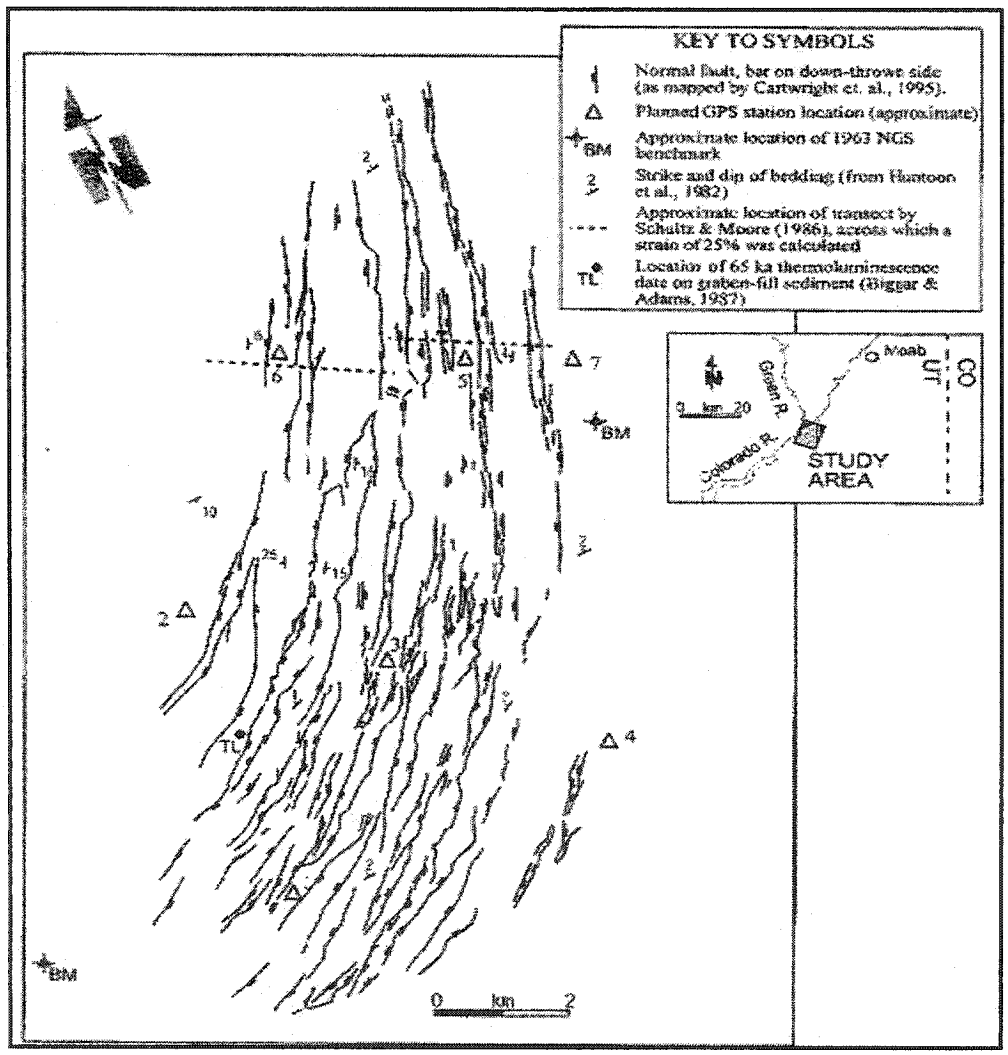

Figure 4.15: Map of faults in the Canyonlands garben system, South Utah. Insert show location of study area
(Source: After Cartwright et al, 1995)

This interferogram is the result of a temporal shift in slant range phase that spans between the two images (July 21, 1993 and February 9, 1996) and thus illustrates the deformation over a period of 933 days (2 years, 6 months and 23 days). The InSAR data used were collected from an ERS-1 (European Remote Sensing satellite platform) descending orbit (track 363, frames 747/765) with a 29-meter perpendicular baseline (Table 4.4). Using a smaller perpendicular baseline as apposed to large one, results in a smaller topography element in our signal and therefore less noise. In our case, the study area (covering an almost 33X50 square Km's) was spread over two frames and thus one frame was shifted towards the other to get one image covering the whole study area.

	Master Image	Slave Image
Acquisition Date	July 21, 1993	Feb 9, 1996
Platform	ERS-1	ERS-1
Track	363	363
Frame	747/765	747/765
Orbit	Descending	Descending
Band	C	C
Wavelength (cm)	5.6565	5.6565
Incidence Angle (Degree)	23	23

Table 4.4: Interferometric date parameters

The raw SAR format data of the two scenes were first processed to ground-range Single Look Complex image (SLC) using ROI_PAC, a SAR processing and Interferometry software developed at JPL/Caltech, producing a 100X100 Km scene with pixel dimensions of 7.9m in range and 4m in azimuth as can be seen in Figure 4.16. A 16-look image is used in the Figure, as it is smaller in size and easier to view. Nominal orbit state vectors of each scene header are enhanced, during image formation, using the ESA/DLR precise state vector (PRC) data provided by the German Processing and Archiving Facility. After the two-image formation process, the master and slave images are registered, where a set of range and azimuth offset measurements are determined and used to estimate a functional mapping to resample the slave image to the master image. A correlation image between the master and slave image is then generated, as can be seen in Figure 4.17, giving good correlation is some areas and bad correlation in others and especially were mountains and river are located. We can notice that the correlation image is flipped over (east and west directions) which is considered a normal part of processing.

The differential interferometric approach employed here is the two-pass plus DEM technique, where isolating and removing the topographic contribution from an interferogram, using a DEM, determine phase due to deformation. In this stage the software uses the available DEM (Figure 4.18) to import the elevations and synthesises the phase due to topography by converting the double binary format DEM into phase representation compatible with RIO_PAC.

For this purpose, a 7.5-minute quadrangle DEM with 30-meter resolution was obtained from the U.S. Geological Survey (USGS). This new interferogram is then subtracted from the initial one to generate the differential phase image. The measured interferogram phase is then unwrapped to determine the absolute interferometric phase, which can be directly related to the topographic height and amount of deformation. Residue-based unwrapping algorithms developed by Goldstein et al., 1988, and referred to as GZW algorithm was implemented in ROI_PAC.

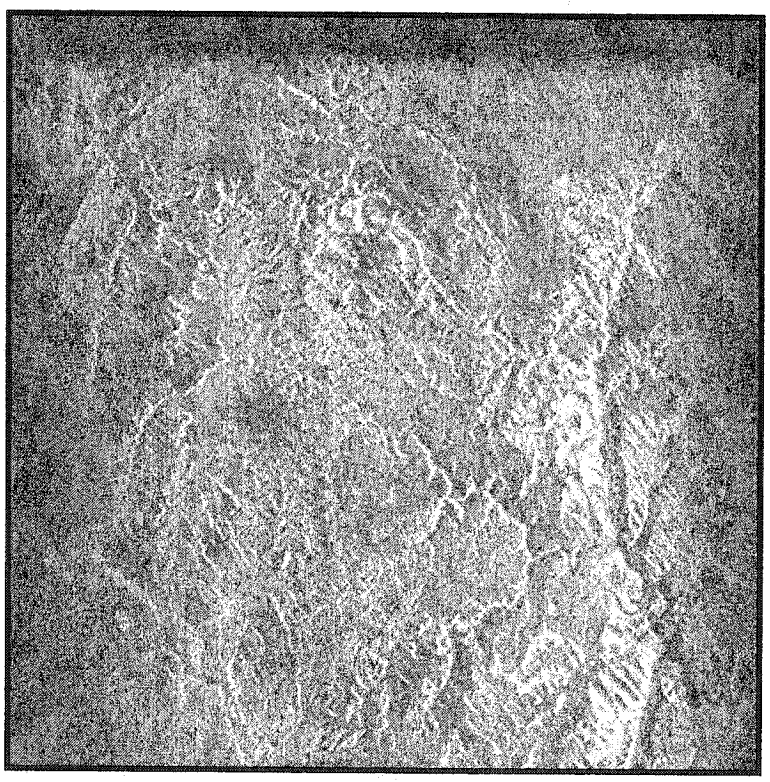

Figure 4.16: Single Look Complex SAR image

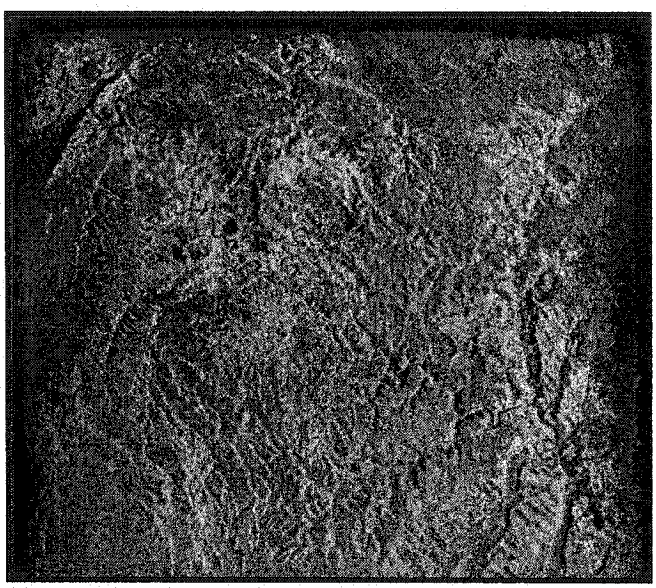

Figure 4.17: Correlation Image

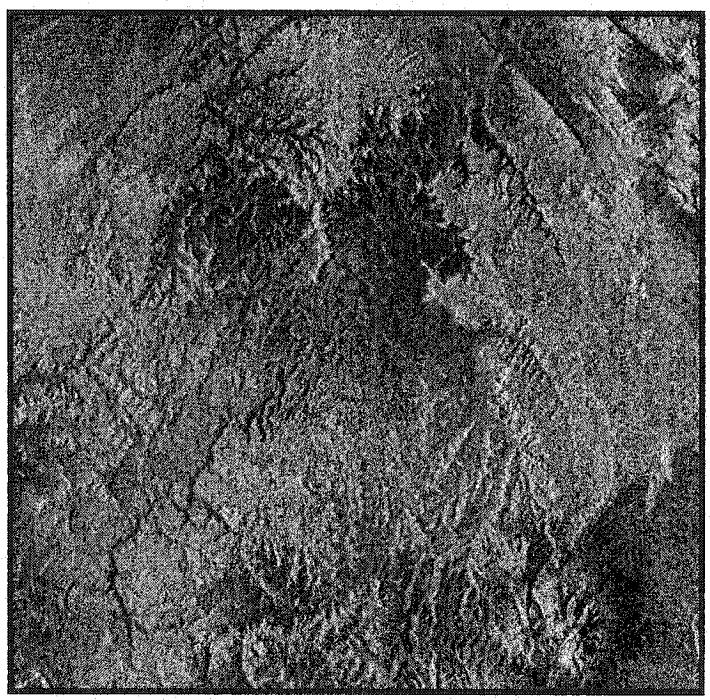

Figure 4.18: DEM used to remove topography

The final differential unwrapped interferogram with a color ramp representing the absolute interferometric phase rate is displayed in Figure 4.19. The profile (black line) shown on the Figure was constructed and used to generate a cross-sectional view illustrating the slant range deformation at a given location and thus give insight into the spatial distribution of deformation within the studied area (Figure 4.20). The furthest point, East of the profile, was assumed stable and thus the deformations obtained in the profile represent the deformation at a giving location relative to that stable point. The amount of deformation in cm is related to the determined absolute interferometric phase as follows:

$$\Delta = \Phi_{absolute} * \frac{\lambda}{4\pi} \tag{4.20}$$

Where, Δ is the amount of deformation in cm, $\Phi_{absolute}$ is the absolute interferometric phase in radian, and λ is the radar wavelength in cm. From the absolute interferometric phase cycle of the 2.5 years pair interferogram, it can be estimated that the maximum downward movement along the constructed profile over that period was approximately 1.18 cm. Since this interferogram was generated using a descending orbit data, a positive deformation that indicates an increase in the line of sight leads to the conclusion that the area of interest is either subsiding or extending away from the satellite. By studying the geological settings of the study area, it was determined that this type of movement agrees very well with the expected ground surface movements. The geological settings of the area are not discussed here as they are out of the scoop of this research.

Figure 4.19: Final differential interferogram

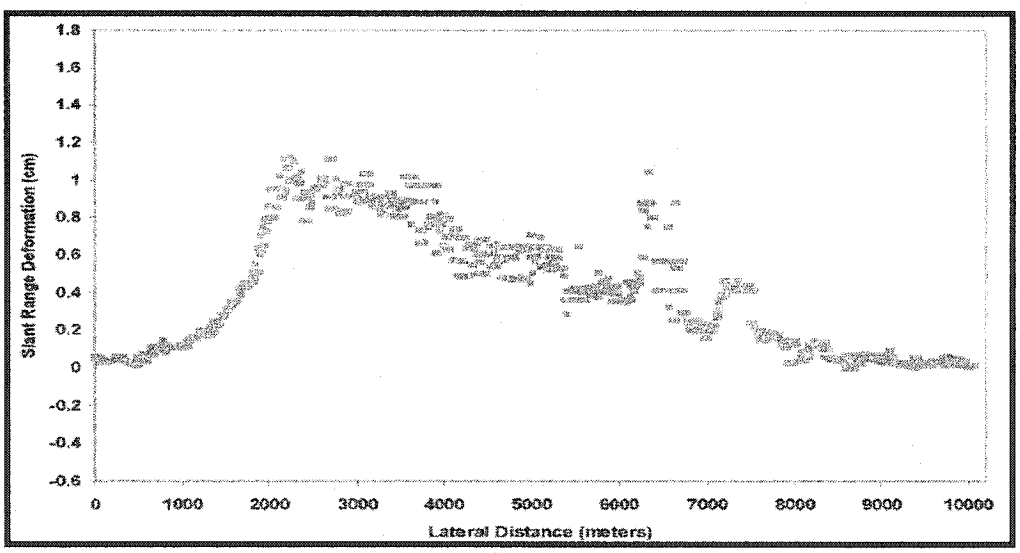

Figure 4.20: Slant range deformation along constructed profile

5. Surface subsidence over a circular underground cavity, a feasibility study

5.1. Overview

The achievements of Synthetic Aperture Radar interferometry (InSAR) in terms of deformation monitoring and topographic mapping have clearly demonstrated the unsurpassed capabilities of the technique in detecting very small ground surface changes. This technique was able to detect ground surface motions in the order of centimeters or less with good resolution (10 m) over large swaths (50 Km) (e.g., Gabriel et al, 1989). Nevertheless, these outstanding results do not necessarily prove the feasibility of this technique for any potential application.

This chapter will investigate the utility of the method in detecting subsidence caused by sinkholes in Karstic areas by studying whether these ground surface deformation can be measured by Synthetic Aperture Radar Interferometry (InSAR).

In this preliminary investigation, it is postulated that the mechanism of ground surface subsidence results due to the existence of an underground circular cavity represented by a circular tunnel. Figure 5.1 shows the flow chart of the proposed methodology. As shown in Figure 5.1, one of the basic premises of the proposed methodology is that ground surface subsidence could be detectable by SAR interferometry techniques.

This preliminary investigation will first start by studying the order of magnitude of ground surface subsidence as well as width of settlement trough caused due to the existence of an underground circular cavity.

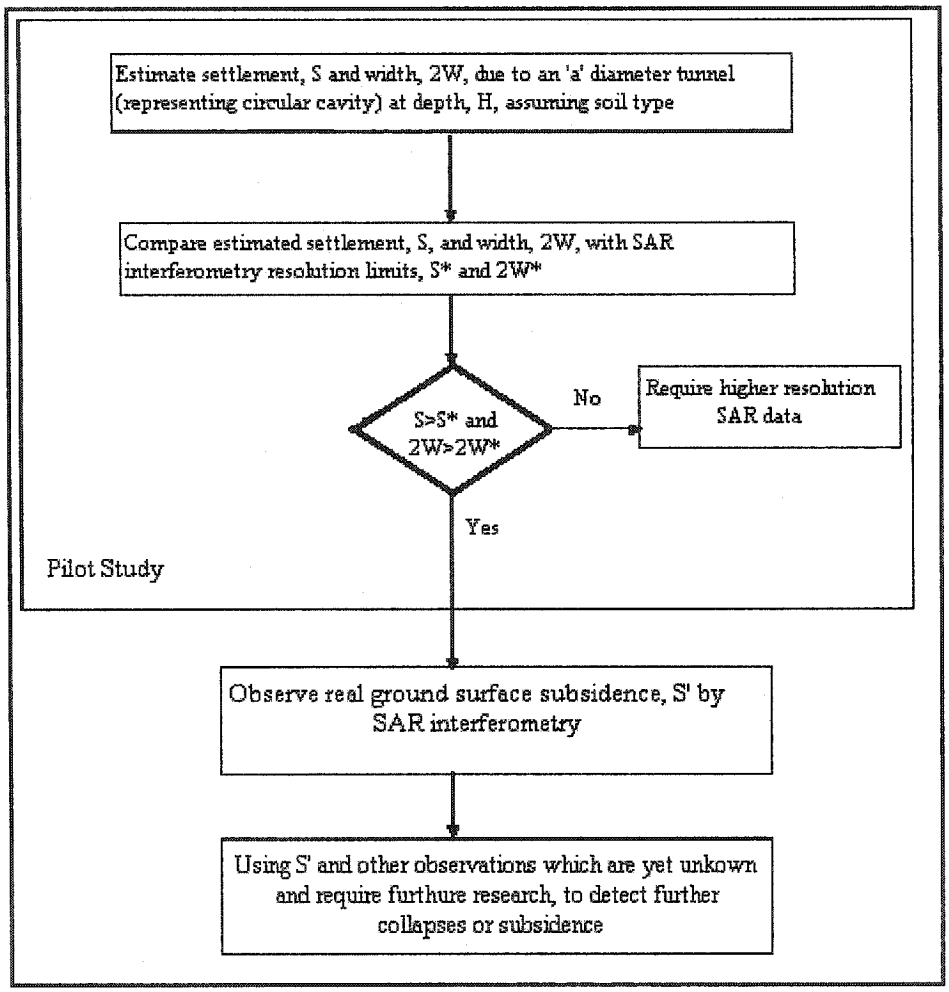

Figure 5.1: Flow chart of the proposed method for monitoring and detecting sinkholes in Karstic areas based on SAR interferometry

A circular tunnel will represent the underground cavity, where a simplified model of the shape of surface settlement trough over a circular tunnel will be used. This simplified model is approximated by the normal probability (Gaussian) distribution theory as can be seen in Figure 5.2 (Peck, 1969; Cording and Hansmire, 1975; and Ghaboussi et al., 1978). Finally, the utility of SAR interferometry in monitoring this phenomenon and whether these settlements magnitude and width are sufficiently large to be detected using this technique will be discussed.

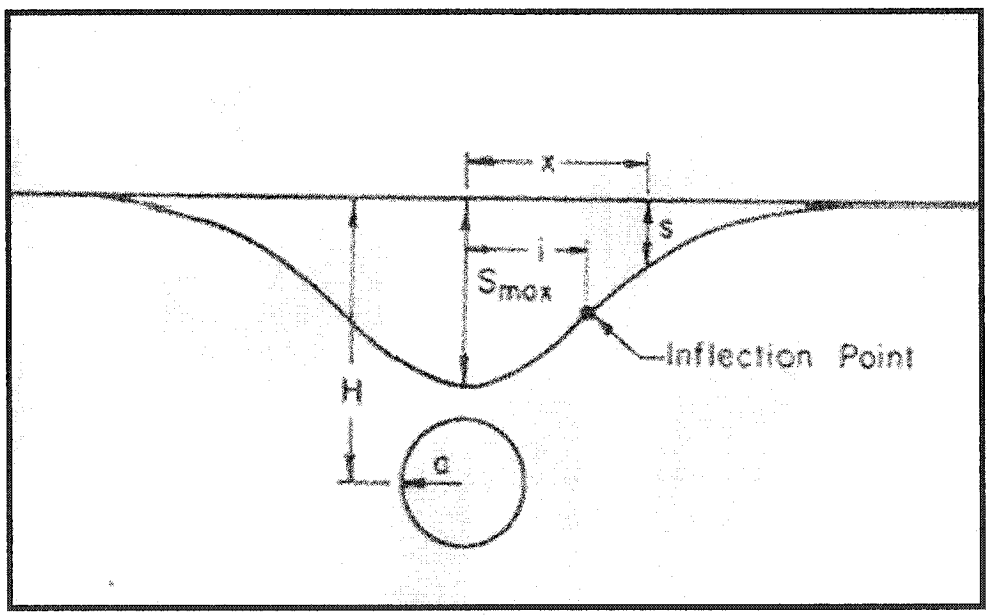

Figure 5.2: Shape of settlement trough as approximated by Gaussian error function (Source: After Ghaboussi et al., 1978)

5.2. Results

As was mentioned earlier in this chapter, for this preliminary investigation it was postulated that the mechanism of ground surface subsidence results due to the affects of an underground circular cavity existing in the effected area.

For the sake of simplicity, an already generated model showing the settlements caused by a circular tunnel will be used in the present analysis as a representation of such cavities. Since SAR interferometry has been reported to be able to detect ground surface fluctuations in the order of centimeters (e.g., Gabriel et al., 1989), hereafter, the magnitude of measurable change in ground surface elevation will be denoted as S*. It was also reported that this technique could measure these very small surface motions with good resolution (10 m) over large swaths (50km) (Gabriel et al., 1989), which means that the technique can discern individual objects which are around 10 meters wide or larger and thus the noticeable object width will be denoted as 2W*. Therefore the one-dimensional model of the shape of settlement trough over a tunnel is introduced in order to determine the soil parameters, ground conditions including the cavity's depth and diameter that may cause both ground surface fluctuation and subsidence profile width to be larger than S* and 2W*.

It has been observed from previous studies that the shape of the surface settlement trough over tunnels in most cases may be approximated by a Gaussian probability curve as was illustrated previously in Figure 5.2 (Ghaboussi et al., 1978). This well accepted error function method, which was based to a great extent on empirical data,

has proven quite accurate (Schmidt, 1969; Peck, 1969; and Sagaseta, 1987). The equation for this curve as stated by Ghaboussi is as follows:

$$s = S_{\max}.\exp-\left(\frac{x^2}{2i^2}\right) \tag{5.1}$$

In which,

s = Settlement at horizontal distance x from tunnel center-line

$S_{\max}$ = Maximum settlement above tunnel center-line

x = Horizontal distance from tunnel center-line

And

i = Horizontal distance to the inflection point

It can be clearly seen from the Figure that the width of the settlement trough, and thus i, are functions of the size and depth of the tunnel and the material properties of the medium (Ghaboussi et al., 1978). It can also be noticed that the approximated average slope of the settlement trough depends on the maximum settlement and width of settlement trough and can be expressed in the following relationship:

$$\text{Average slope} = \frac{S\max}{W} \tag{5.2}$$

Here,

W= Horizontal distance from the tunnel center-line to the furthest point on the settlement trough, which can be determined from the horizontal distance to the inflection point, i, using the following equation:

$$W = 2.5\ i \tag{5.3}$$

For practical purposes, it is reasonable to assume that:

$$i = k\,(H-Z) \tag{5.4}$$

Where,

k= Coefficient determined by the method proposed by Mair et al. (1993)

H= Distance below surface to tunnel axis

Z= Elevation at settlement of interest

Since we are interested in settlement caused at ground surface, Z in our case is set to zero. Two methods can be used to estimate the width of settlement trough for different ground conditions. Both methods will be used in this feasibility study to determine the soil parameters, ground conditions including the cavity's depth and diameter that may cause the subsidence profile width to be larger than the present technique resolution limits.

The first methods uses previously determined k values estimated using field measurements above tunnels in both UK and worldwide (Ranking, 1998). Mair et al. (1993) reported that for clay, the data was reasonably consistent with k= 0.5, while for sands, a reasonable fit for most of the data was achieved using k=0.3. Hereafter, we are able to determine the total width of settlement trough to be:

$$\text{Total width} = 2W = \begin{cases} 2.5H & \text{for clays} \\ 1.5H & \text{for sands} \end{cases} \tag{5.5}$$

Since SAR interferometry techniques can only discern individual objects that are 10 meters wide or larger, using this method means that the axis of the tunnel has to be located at least 4 meters below the ground surface in clay and 7 meters in sands to cause subsidence wider than 10 meters and thus be detected by the technique used. Figure 5.3 shows the relation between the depth below surface to tunnel axis, H, and width of settlement trough, 2W for k=0.5.

Figure 5.4 shows the same relation for k=0.3. Using this method one can clearly notice that the width of settlement trough depends on the depth below surface to tunnel axis only. However, affects of tunnel diameter are taken into account when determining the coefficient k.

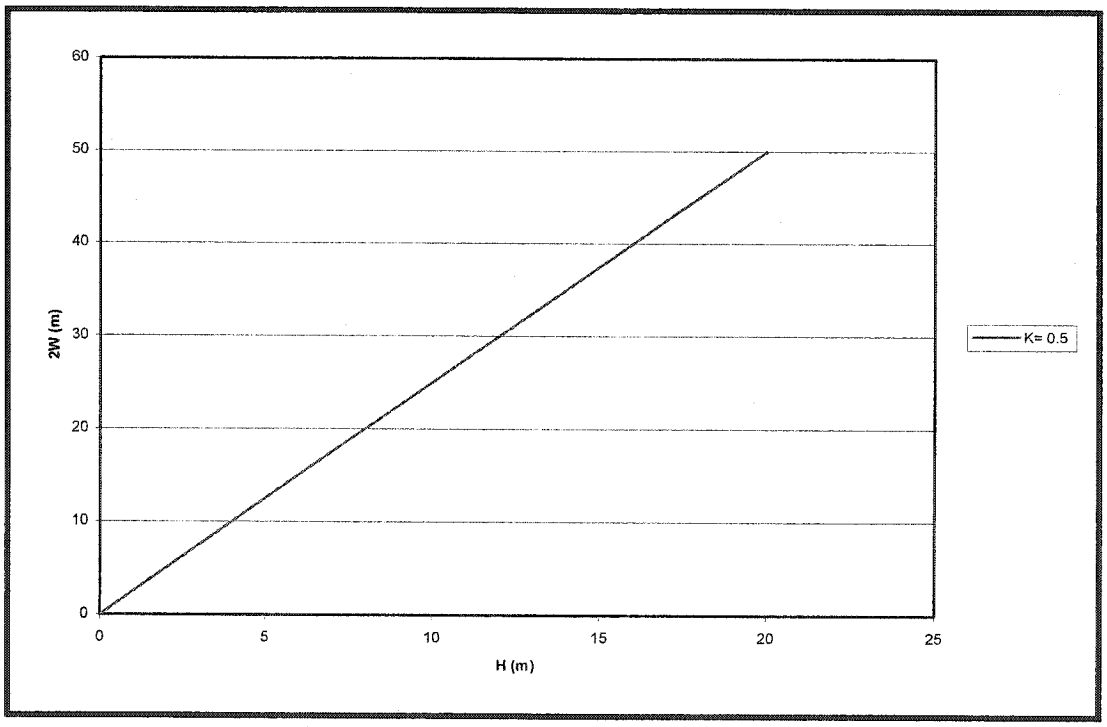

Figure 5.3: Relationship between depth below surface to tunnel axis, H, and total width of settlement trough, 2W for clay, k=0.5

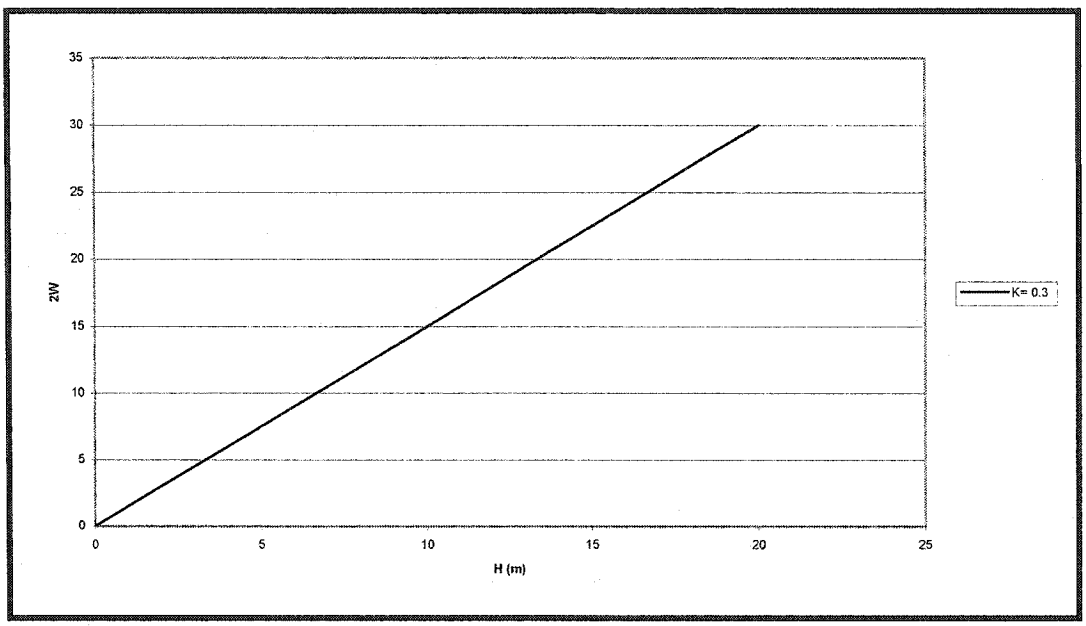

Figure 5.4: Relationship between depth below surface to tunnel axis, H, and total width of settlement trough, 2W for sand, k=0.3

The second method used for determining the width of settlement trough depends on the geometry of the relationship illustrated on the upper part of Figure 5.5. Hansmire (1975) suggested this relationship, which is expressed in terms of an angle β, after further studying a relationship between H/2a and i/a for various soil types presented by Peck (1969). Both relationships presented by Hansmire (1975) and Peck (1969) are illustrated in Figure 5.5.

The model parameters here are:

β = an angle depending on soil type

H (m)= Depth below surface to the tunnel axis

2a (m) = Tunnel diameter

2W (m)= Total width of settlement trough

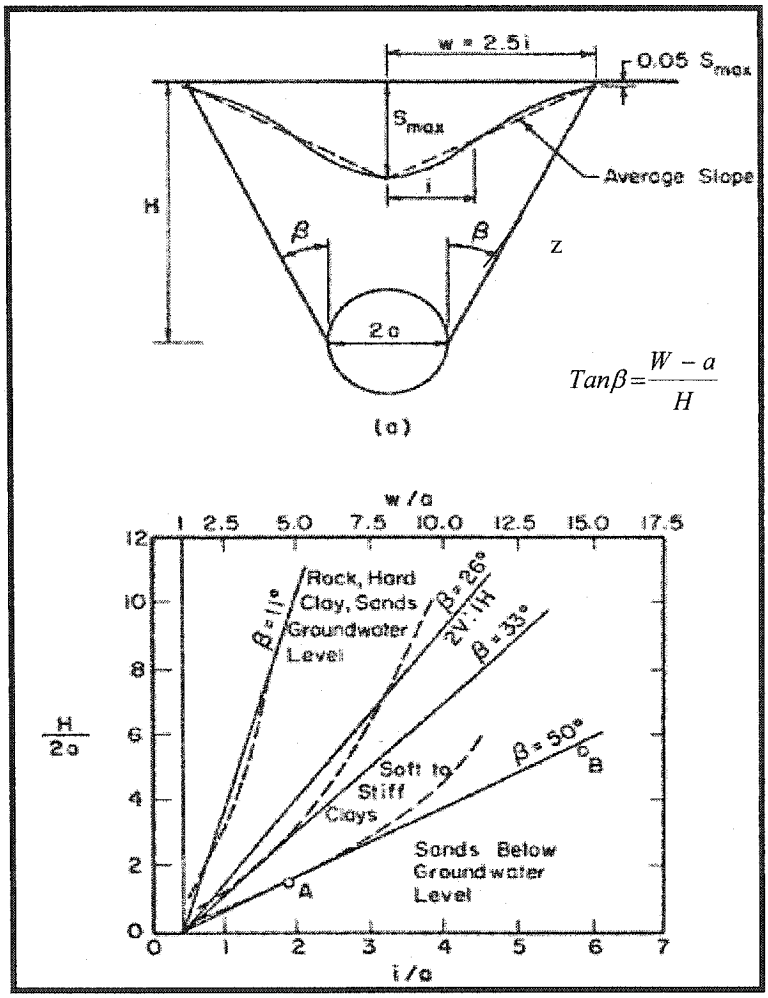

Figure 5.5: Relationship between β and width of settlement trough, 2W, based on relationships presented by Peck (1969)
(Source: Modified after Ghaboussi et al., 1978)

The angle β can be expressed in terms of half of the width of trough, W, tunnel radius, a, and depth below surface to tunnel axis, H and follows:

$$\text{Tan } \beta = \frac{W - a}{H} \tag{5.6}$$

From the geometry of the relationship, illustrated in Figure 5.5, half of the width of settlement trough, W can be expressed as follows:

$$W = a + (z \text{ Sin } \beta) \tag{5.7}$$

It can also clearly be seen from the geometry of Figure 5.5 that the depth below surface to tunnel axis can be expressed as:

$$H = z \text{ Cos } \beta \tag{5.8}$$

And thus,

$$z = \frac{H}{Cos\beta} \tag{5.9}$$

Substituting Eq. (5.9) into (5.7), we get:

$$W = a + H \text{ Tan } \beta \tag{5.10}$$

The values of β suggested by Peck (1969) where used to plot Figure 5.6 below. The present technique resolution limits were taken into account in this Figure by setting half of the width of settlement trough, W to 5 meters.

Given the soil conditions, one can use Figure 5.6 to determine the minimum depth below surface to tunnel axis, H for a given tunnel radius, a, that will cause a settlement at ground surface detectable by the technique.

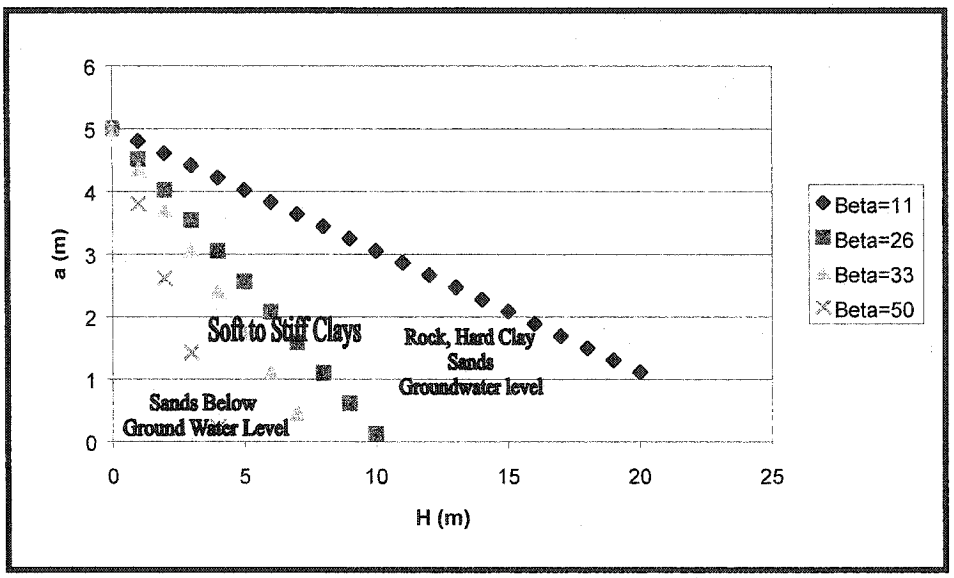

Figure 5.6: Relationship between a, H and Beta for W= 5m

The Figure can also be used the other way around, where for a given depth below surface to tunnel axis, H, one can determine the minimum tunnel radius that will cause a settlement trough width measurable by SAR interferometry. Using the values of depth below surface determined from the first method, H= 4 meters for clays and 7 meters for sands, the minimum tunnel radius that will cause a settlement trough width detectable by the technique should be 2.4 and 2.6 meters respectively. For sands it was assumed the tunnel is at groundwater level and thus an average value of $\beta = 18.5$ was used. From the above results, it may be concluded that the width of settlement trough due to the existence of a circular underground cavity can be sufficiently large to be detected using SAR interferometry, provided that the depth below surface to cavity axis, H, for clays and sands is at least 4 and 7 meters respectively.

The second step in this feasibility study is to determine the amplitude of surface motion that is induced by the existence of a (2a) diameter tunnel at a distance H below surface and make sure it satisfies the resolution limits of the technique.

This implies that the magnitude of settlement at the furthest horizontal point from the tunnel centerline, which is at x=W, should be equal or larger than measurable change in ground surface elevation, S*, where S*= 1 cm. Substituting for x = W in Eq. (5.1), we get:

$$S = 0.0439\ S_{max} \tag{5.11}$$

Since SAR interferometry has been reported to be able to detect ground surface fluctuations in the order of centimeters (e.g., Gabriel et al., 1989), Eq. (5.11) implies that for the settlement to be detectable, the value of the maximum settlement, S_{max}, which is located above the tunnel center-line, should be either equal to or larger than 23 centimeters.

It is important at this point to define three terms that will be used in our analysis. Volume change, ΔV, is defined as the increase or decrease in soil volume caused by tunneling, whereas the volume of surface settlement, Vs, in the volume of the settlement trough at the ground surface. The third term, volume of lost ground, VL, is defined as the volume of all ground movements taking place about the tunnel (Bickel et al., 1996).

The relationship among these quantities is complex and incompletely defined and thus for most purposes, it is usually possible to assume that the volume of surface settlement is equal to the volume of lost ground (Bickel et al., 1996).

Bickel and others reported that this assumption is generally workable except in soils exhibiting significant increases in soil volume, bulking, or decreases in soil volume, consolidation.

Given the maximum settlement over tunnel centerline, S_{max}, the volume of surface settlement, Vs, (per meter length of tunnel) can be obtained from the integration of Eq. (5.1), and is given by (Cording and Hansmire, 1975; Whitter and Frith, 1990; and Mair et al., 1993):

$$V_S = 2.5\, i\, S_{max} \tag{5.12}$$

Given the ground loss, V_L, the maximum settlement can be used to determine the minimum tunnel diameter, 2a, according to the following (Mair et al., 1993):

$$S_{max} = 0.313\, \frac{V_L (2a)^2}{i} \tag{5.13}$$

For clays, substituting for S_{max} equal to 0.23 meters in Eq. (5.12), assuming that V_L=Vs as Bickel and others (1996) suggested, and using i value obtained for clays above, Eq. (5.13) implies that the minimum tunnel diameters that can cause settlements detectable by SAR interferometry is 1.13 meters, whereas for sands, the minimum tunnel diameter should be 0.85 meters.

From the results of this preliminary parametric study, it may be concluded that the ground subsidence due to the existence of subsurface cavities can be sufficiently large to be detected using SAR interferometry, provided that the cavity has a radius larger than 2.4 meters and located 4 meters below ground surface in clay.

In sand, the minimum tunnel radius and depth below surface to tunnel axis should be 2.6 and 7 meters respectively. The magnitude and width of subsidence trough caused by such sized cavities are close to the present resolution limits of SAR systems.

As depth below surface to tunnel axis increases, the tunnel radius required to cause a measurable settlement magnitude and width of trough decreases. Figure 5.6 above, can be used to calculate the minimum tunnel radius for a given depth below surface to tunnel axis, H, for different soil conditions.

As a final step the collected case histories, presented in the database developed in chapter 3, were compared to the resolution of the proposed method to determine whether they could have been detected if such method would have been used to study them. Only 51.2% of the collected case histories provided sinkhole width and depth information and thus could be used in such a comparison.

Since SAR interferometry has been reported to be able to detect ground surface fluctuations in the order of centimeters with good resolution (10m) over large swaths (50km) (Gabriel et al., 1989), only individual objects that are around 10m wide or large could be discern by this technique. Given that, 54.7% of the collected case histories with width and depth information could have been detected. This technique could not have been used to detect the other 45.23%, as their widths were way below the technique resolution.

6. Repeat orbit interferometry package (ROI_PAC)

This chapter explains in details the algorithms and procedures implemented in ROI_PAC, the Repeat orbit Interferometry Package developed at JPL and Caltech and used in this study. The package, wrote by many contributors, was initially developed at JPL in the 1980 and first released outside JPL and Caltech in 2001. The package processing steps were thoroughly explained in ROI_PAC documentation, part of a Ph.D. dissertation titled "Radar interferometry measurement of land subsidence", by Sean Buckley in 2000. This chapter will provide a terse summery of the ROI_PAC package documentation.

ROI_PAC, which allows researchers in the area of topography and surface change to apply Interferometric Synthetic Aperture Radar (InSAR) methods, implements its fundamental algorithms in C and Fortran 90 programs and drives each executable routine with a Perl control script, running on SGI, Sun, and Linux platforms (Rosen, 2002). The major ROI_PAC processing steps and code elements, listed in Table 6.1, form the basis of the data reduction for the bulk of geophysical applications that use InSAR (Buckley, 2000; and Rosen and Persaud, 2000). This package takes raw data and performs all the necessary interferometric processes such as formation of SAR images, generating the interferogram, phase unwrapping and finally absolute phase determination and removal of signal due to topography. The following sections will describe the major ROI_PAC codes and their functions to help in better understanding the theory behind this software.

Processing Step	Code Element
Process Control	Process_2pass.pl
SAR raw data conditioning	make_raw.pl
SAR image formation	roi.pl
SAR image registration	offset.pl
Interferogram formation	resamp.pl
Baseline determination	phase2base.pl
Interferogram flattening	flatten.pl; look.pl
Correlation determination	icu.pl
Interferogram filtering	icu.pl
Phase unwrapping and absolute phase determination	icu.pl; baseline.pl

Table 6.1: The general processing steps and code elements
(Source: Modified after Buckley, 2000; and Rosen and Persaud, 2000)

The process can be performed and deformation estimated by either using a pair of ERS SAR images and a Digital Elevation Model (DEM), as in this research, to remove phase due to topography, a set of three SAR images, or a set of four SAR images. Although ROI_PAC, as stated by Rosen (2003), is developed primarily to work with ERS data, since ERS assumptions are built into some of the codes and currently supporting ERS-1, ERS-2 and JERS data, it is configurable to work with "strip-mode" data from all existing satellite radar instruments.

ROI_PAC computes the interferometric baseline, which is the orbital separation of the satellite at the observation times, from the provided navigation solutions and then refines the estimate to the mm level of precision using the provided DEM and optional deformation model as reference (Rosen, 2003). Topography signature is later removed by simulating an interferogram from the orbit data and the DEM, subtracting its phase from the measured interferogram and thus leaving just the deformation phase. Figure 6.1 illustrates a flow chart of the image formation process, whereas Figure 6.2 shows the steps involved in the process of generating an interferogram. The 2-pass interferometric technique processing steps implemented by ROI_PAC are illustrated in Figure 6.3. Since USGS DEM's are easily obtained whereas the cost of ERS radar data is high, two-pass technique, where a USGS DEM is used to remove interferometric phase due to topography, will be implemented later in chapter 8 of this dissertation. The resulting interferogram is produced in both its original radar coordinate system as well as georeferenced to the DEM used.

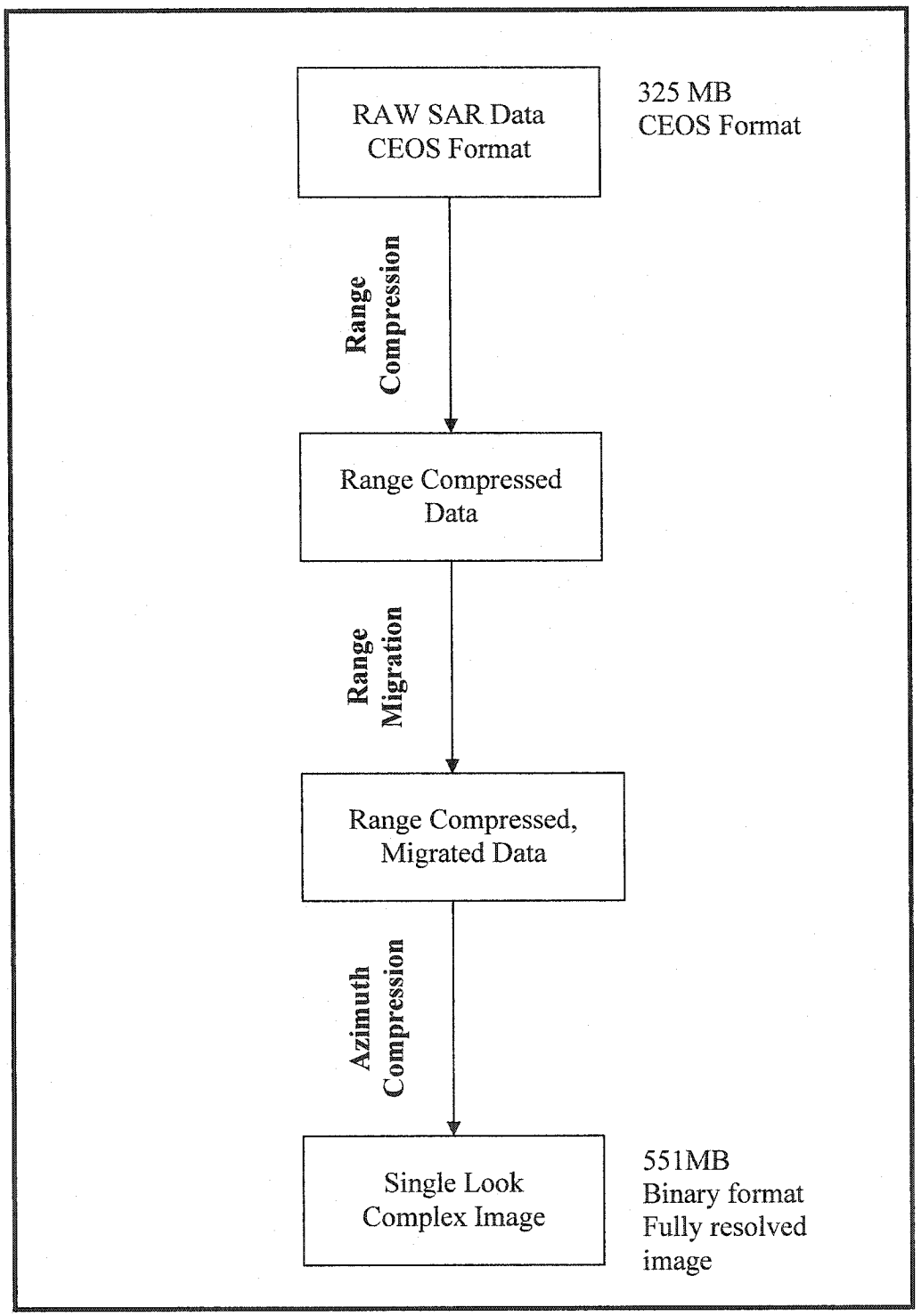

Figure 6.1: Image formation process

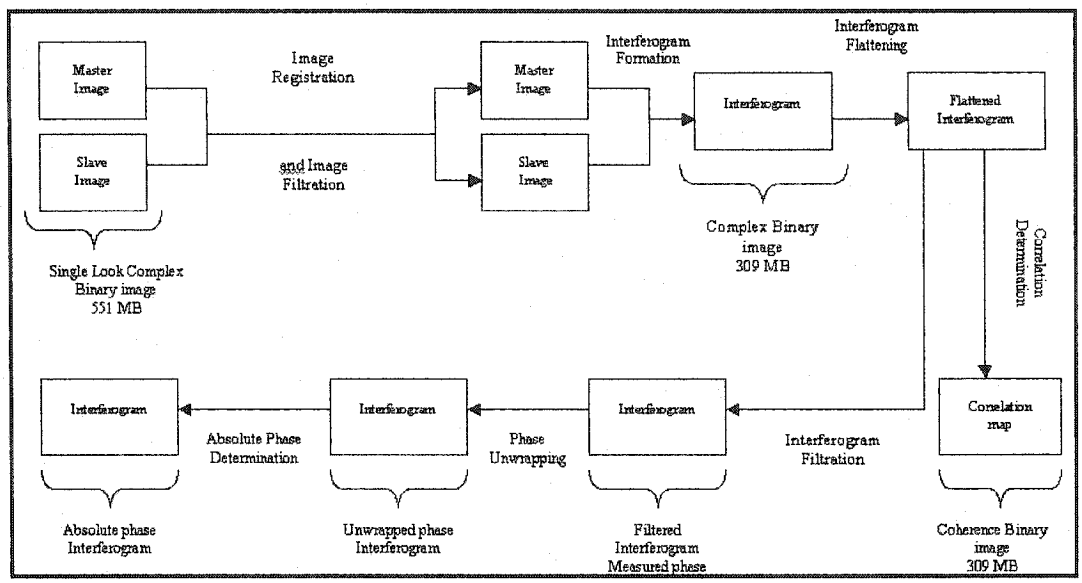

Figure 6.2: Generating interferogram process steps.

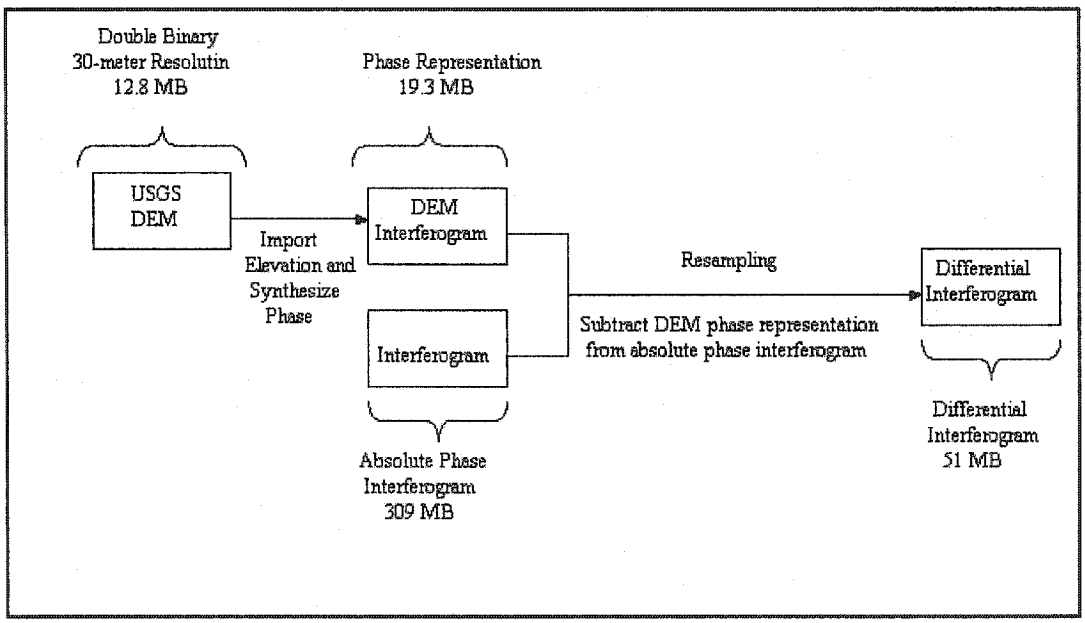

Figure 6. 3: Two pass interferometry process steps

6.1. Process control

The script, process_2pass.pl, goes from raw data through generating unwrapped differential interferometric phase. This script is designed in a way that partial processing of the data is allowed and thus if any particular part of the process happens to fail or is even interrupted, after fixing the problem, the processing can be easily restarted where it left off. Process_2pass.pl calls many other Perl scripts, Fortran, and C programs. To better understand each Perl script usage, intermediate processing stages, and calling sequence one can refer to the documentation script, pod2man.pl, which provides a brief description of each script, its syntax, and what each script performs.

6.2. Raw data conditioning

InSAR requires the use of multiple radar data pairs to better estimate the deformation in the studied area. These sets have to be processed consistently relative to each other and thus, to carefully control the processing of the data, raw signal data or so-called Level 0 data are used. Although raw data from variable sources can be different since there is significant variation in the degree in which various processing facilities prepare the satellite downlink for distribution as raw signal data, such data is considered the most basic level of radar data available. Raw data conditioning is a process that involves steps in which raw data is corrected and prepared for the next step, known as image formation. The following sections will explain briefly the steps involved in the raw data conditioning process starting with the data format needed all the way through preparation of raw data for the image formation procedure.

6.2.1. Raw Data format

Presently, raw SAR data are distributed in the Committee on Earth Observation Satellite (CEOS) format and includes the four following files:

1. Volume Descriptor File
2. SAR Leader File
3. Raw Data File
4. Null Volume File

The first file, Volume Descriptor File, includes description of the arrangement and order information of the data on the storage media. Information relevant to the specific SAR data set, such as raw data file size, spacecraft height, time of acquisition (UTC), and scene center latitude and longitude, etc, are provided in the SAR Leader File. The raw Data File is the actual SAR data and includes both the header file and the SAR raw data stored as one data line per record with each record having a prefix, raw data, and a suffix. Whereas the Null Volume File can be ignored as it includes information not important to the processing procedure

6.2.2. Missing line correction

While processing and preparing data at the archival facility, lines with bad data could occur. These lines are identified and removed and thus are considered as missing lines. Such missing lines in the raw data can pose a problem when using these sets for interferometry applications, where a pair of images are used and must be registered to the sub-pixel level. One could check for missing lines in ordered data by extracting the line counter from the prefix information of each raw data record

and checking if a non-consecutive line counter value exist. A non-consecutive line counter value indicates the existence of a missing line, a problem that can be fixed by simply duplicating the previous data line and thus having it as a replacement for the missing line.

6.2.3. Sampling window start time adjustment (SWST)

Radar return sampling is another important data conditioning step that should be performed on raw data before starting radar interferometry processing. The SAR satellite transmits a pulse of microwave energy that radiates, interacts with the target and illuminates the scene and reflects back towards the radar (Figure 6.4). This backscattered energy is sampled at the range sampling frequency starting at the sampling window start time (SWST) (Buckley, 2000; and Rosen and Persaud, 2000).

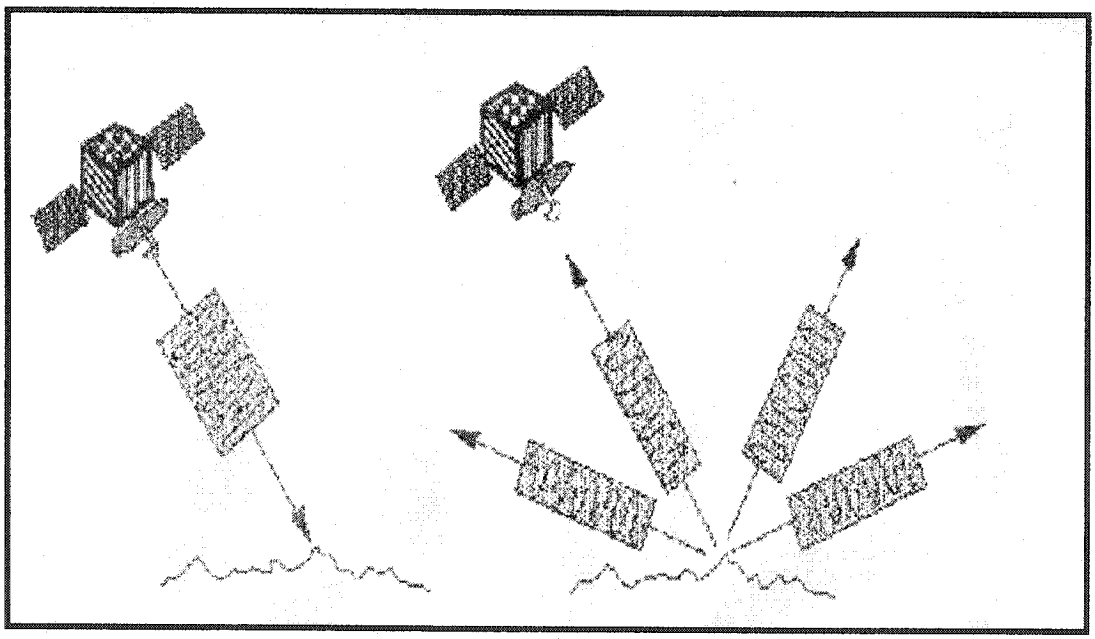

Figure 6.4: Radar transmits a pulse and measures reflected echo (backscatter) (Source: After Freeman, 2000)

As the topography of the imaged area changes, the topographic height of the surface illuminated changes and thus the total transit time taken by the pulse to reach the surface, and return back to the radar changes. To accommodate these changes in transit time, the SWST must be adjusted to keep the data sampled within the illuminated swath (Buckley, 2000; and Rosen and Persaud, 2000).

6.2.4. Data Unpacking

The backscattered energy of the radar is stored as a complex number with two components (Hanssen, 2001):

1- In-phase, represented by the real component of the complex number

2- Quadrature, represented by the imaginary component of the complex number

Both the in-phase and quadrature components of each return sample are 5-bit quantized integer values in the nominal operation mode and sequentially packed as contiguous blocks of 10 bit samples with the first bit being most significant one (Wiik, 2003). Before starting the image formation process, raw SAR data must be unpacked, a procedure in which the distribution of values from each channel are adjusted to have a zero mean (Wiik, 2003). If this step is ignored, the channels biases (and their relative imbalance) will result in gain and phase imbalances (Wehner, 1995, and Buckley, 2000).

This step requires a large hard disk storage space and thus is performed by the image formation software, as part of the data read in so as to save storage space on the hard disk. When raw data is unpacked, each sample component is converted from a quantized integer to a real number and thus the bias from each channel is removed.

For ERS SAR raw data, the nominal in-phase and quadrature biases would be 15.5 (Buckley, 2000; Rosen and Persaud, 2000; and Wiik, 2003). An archival facility determines and removes actual biases and stores deviations from the nominal bias, which are usually common but small, values in the SAR Leader File (Wiik, 2003).

6.2.5. Image formation parameter extraction

Several input parameters are required for the image formation process and must be determined prior to starting the process. Input parameters include radar system parameters, such as pulse repetition frequency, sampling frequency, pulse length and wavelength. Table 6.2 lists ERS SAR system parameters; it should be noted that these parameters could vary slightly between observations. A detailed definition of each parameter will be discussed later in this chapter.

Interferometric processing also requires the knowledge of satellite orbit parameters such as the satellite body fixed position, velocity, and height above the reference point on surface as well as the radius of earth. Buckley (2000), and Rosen and Persaud (2000) stated that significant issues have been raised as to the amount and quality of orbit information provided in the SAR Leader File as some archival facilities provide five or more state vectors spanning the time of the SAR acquisition, whereas others provide virtually no information. To avoid such issues, the data used for this project utilizes ESA/DLR precise state vector (PRC) data provided by the German Processing and Archiving Facility.

System Parameter	Value
Pulse repetition interval, Δt_{PRI}	595.27μs
Pulse repetition frequency, f_{PRF}	1679.9Hz
Sampling frequency, f_s	18.962 MHz
Pulse length, τ_p	37.12 μs
Chirp slope, K	418.91 GHz/s
Wavelength, λ	5.6666 cm
Carrier frequency, f_0	5.29 GHz
Bandwidth, f_{BW}	15.55 MHz

Table 6.2: ERS SAR satellite system parameter
(Source: Modified after Buckley, 2000; and Rosen and Persaud, 2000)

Figure 6.5 and 6.6 illustrates these parameters using the SAR pulse time history. One additional parameter required for image formation processing, the range to a given sample ρ, can be determined given the range sample spacing Δr determined from sampling frequency, the total number of samples relative to the first range sample, as well as the range to the first sample ρ_0 (Figure 6.7). The sample spacing, Δr, which is the area each pixel covers, can be determined from the sampling frequency. Range to the first sample, ρ_0, for ERS SAR satellite systems (ERS-1 and ERS-2) can be determined using the following (Buckley, 2000):

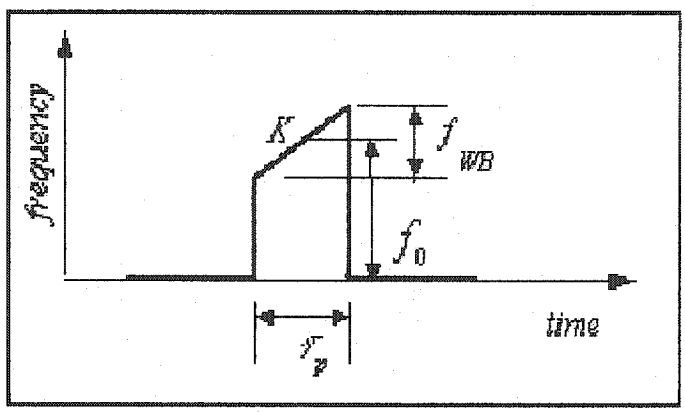

Figure 6.5: Linear FM Chirp

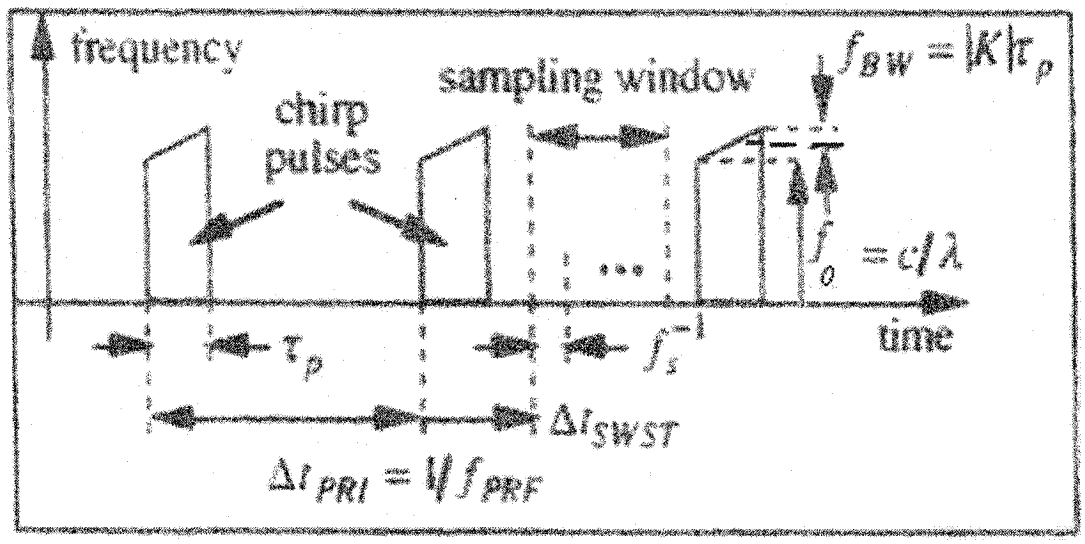

Figure 6.6: SAR pulse time history
(Source: Modified after Buckley, 2000)

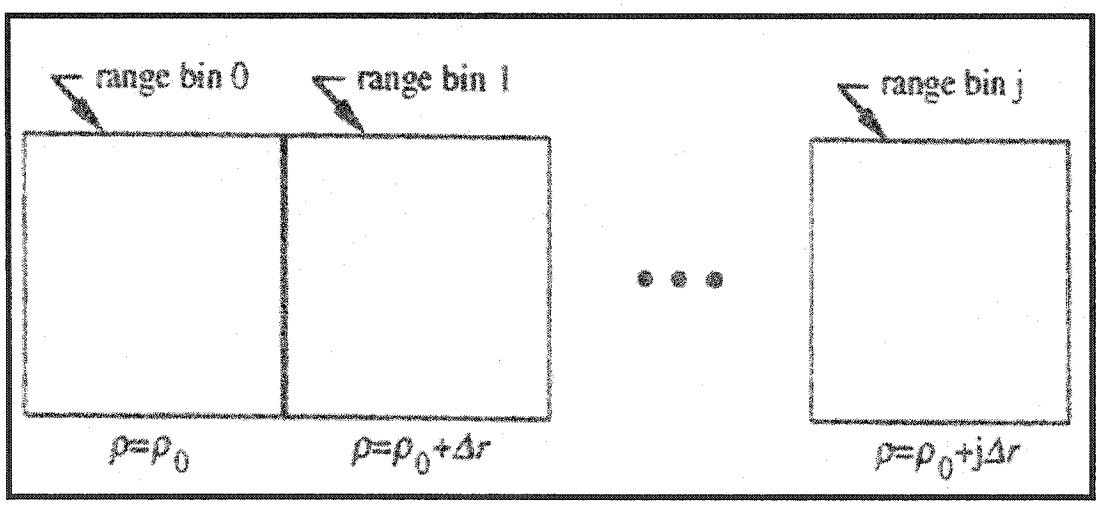

Figure 6.7: Relationship between slant range and range bin
(Source: After Buckley, 2000)

$$\rho_0 = \frac{c}{2}\Delta t_{SWST} \tag{6.1}$$

Where

$$\Delta t\text{SWST} = n\text{SWST}\Delta t_n + 9\Delta t_{\text{PRI}} - 6x10^{-6} \tag{6.2}$$

$$\Delta t_{\text{PRI}} = (n_{PRI} + 2)\Delta t_n \tag{6.3}$$

c = Speed of light

ΔtSWST = Sampling window start time, seconds

Δt_{PRI} = Pulse repetition interval, seconds

nSWST = SWST count

n_{PRI} = PRI count

And Δt_n = Count duration, seconds = $210.94x10^{-9}$

Both the ERS SAR system SWST count, nSWST, and PRI count, n_{PRI}, are given in the prefix of each raw data record. Given the ERS SAR satellite system parameters (Table 6.2), one can determine the ERS SAR PRI count, n_{PRI}, to be 2820.

6.3. Image formation

SAR imagery is built up and characterized using both the time delay and strength of the received backscattered signals, which is primarily affected by the imaged surface roughness and electrical properties such as water content. Since synthetic aperture of SAR uses the redundancy in subsequent pulse returns that explain a single target point, the inverse problem, reconstructing the response from a series of pulse return signals is referred to as SAR focusing or processing (Hanssen, 2001).

Several SAR image formation and focusing technique categories for interferometric applications were developed, with the major and most widely used technique known as range-Doppler processing. For more information on the image formation process, one can refer to numerous books dedicated for this procedure, e.g. Curlander and McDonough (1991), Fitch (1988), and Wehner (1995). This section will briefly explain the image formation process and from a radar interferometry point of view only. The range-Doppler SAR technique will be thoroughly discussed in this section since this algorithm was used to process the ERS SAR data used in this study.

As was explained earlier (chapter 4 of this dissertation), the received backscattered signal of a point target, a quantity that characterizes the image formation process is spread in range (across flight track) and azimuth (along flight track) directions (Figure 6.8). The following section will start with defining the major element of image formation process, the received signal, also known as chirp pulse.

6.3.1. Chirp pulse

A unit amplitude and unit time duration radar pulse centered at time t= 0 can be written as (Buckley, 2000; and Rosen and Persaud, 2000):

$$\text{rect}[t] = \begin{cases} 1, & |t| \le \tfrac{1}{2} \\ 0, & \text{Otherwise} \end{cases} \tag{6.4}$$

In general, a radar pulse centered at time $t = t_i$ with amplitude A (t) and time duration τ can be expressed as (Buckley, 2000):

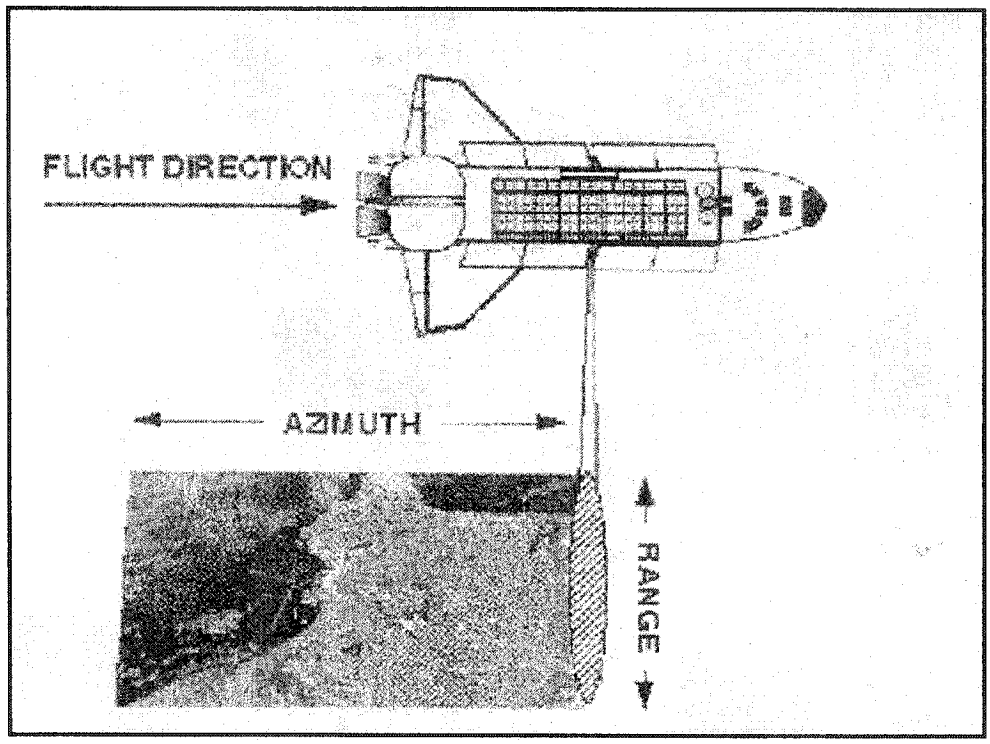

Figure 6.8: Building up a radar image using the motion of the platform (Source: After Freeman, 2000)

$$A(t)\text{rect}\left[\frac{t-t_i}{\tau}\right] = \begin{cases} A(t), & t_i - \frac{\tau}{2} \le t \le t_i + \frac{\tau}{2} \\ 0, & \text{Otherwise} \end{cases} \quad (6.5)$$

And thus a linear frequency-modulated (FM) chirp, $s_n(t)$, which can also be referred to as a chirp pulse, centered at time $t = 0$ and transmitted at time $t = -\tau_p/2$, can be expressed as follows (Buckley, 2000; and Rosen and Persaud, 2000):

$$s_n(t) = e^{j\Psi}\text{rect}\left[\frac{t}{\tau_p}\right] = e^{j2\pi\left[f_0 t + \frac{K}{2}t^2\right]}\text{rect}\left[\frac{t}{\tau_p}\right] \quad (6.6)$$

Where

Ψ= Phase shift of transmitted pulse

f_0 = Carrier frequency

K = Chirp slope, Hz/s

And

τ_p = Pulse duration

A chirp with positive chirp slope K is referred to as an up chirp, whereas a negative chirp slope K is referred to as a down chirp.

In a linear frequency modulate (FM) chirp waveform (Figure 6.6) the instantaneous frequency $f(t)$ of the pulse behaves linearly with respect to time as follows (Buckley, 2000; and Rosen and Persaud, 2000):

$$f(t) = \frac{1}{2\pi}\frac{d\Psi}{dt} = f_0 + Kt \qquad \text{for} \qquad -\tau_p/2 \le t \le \tau_p/2 \tag{6.7}$$

Using the above equations, one can closely approximate the linear frequency modulation (FM) bandwidth, f_{WB}, which is defined as the frequency range of the system measured as the difference between the highest and lowest frequencies that the system supports, from the difference between the instantaneous frequency extremes as follows (Buckley, 2000; and Rosen and Persaud, 2000):

$$f_{WB} = (f_0 + K\tau_p/2) - (f_0 - K\tau_p/2) = |K|\tau_p \tag{6.8}$$

To simplify the development of the chirp pulse point target response, we could assume that the range between the radar and a given imaged point to be fixed for a given pulse, this assumption is referred to as the start-stop approximation and explains why the 2D image formation process could be split into two 1D frequency-domain processing steps in the range-Doppler technique (Buckley, 2000; and Rosen and Persaud, 2000)

One can also determine the time delay, τ(s), between radar signal transmission and reception of backscattered signal, of an imaged point on the surface at a range distance (across flight track), ρ, using the following equation (Buckley, 2000; and Rosen and Persaud, 2000):

$$\tau(s) = 2\rho(s)/c \tag{6.9}$$

Where

s = Known slow time (along-track)

And c = Speed of light

And thus, the imaged point target response $r(s,t)$ is a function of the slow time s and the so-called fast time, t, associated with the range direction, and can be expressed as follows (Buckley, 2000; and Rosen and Persaud, 2000):

$$r(s,t) = s_n(t-\tau(s)) = e^{j2\pi\left[f_0(t-\tau(s))+\frac{K}{2}(t-\tau(s))^2\right]} rect\left[\frac{t-\tau(s)}{\tau_p}\right] \quad (6.10)$$

Where

τ (s)= round-trip time between transmitting and receiving

The carrier frequency is then removed as part of the in-phase and quadrature sampling with a procedure known as basebanding, resulting in the following imaged point target response (Buckley, 2000; and Rosen and Persaud, 2000):

$$r(s,t) = e^{-j4\pi\rho(s)/\lambda} e^{j\pi K[t-\tau(s)]^2} rect\left[\frac{t-\tau(s)}{\tau_p}\right] \quad (6.11)$$

Where

$\lambda = c/f_0$ = The Systems wavelength

This procedure assumes that the carrier frequency, f_0, at time t is equal to zero and thus result in a more accurate images point response.

6.3.2. Matched filter

The major task of an image formation procedure is to process the sampled radar return so as to be able to identify the imaged point targets and allocate them to the appropriate location in the resultant output image. To do so, the matched filter approach, developed by Dr. D.O. North in 1943, is implemented in ROI_PAC to

compress both slow and fast time point target response and determine the appropriate range and azimuth locations. This section will briefly explain the matched filter. For more details, one can refer to a review of the matched filter procedure written by Curlander and McDonough, 1991.

Since the model input and output equations, Eqn. (6.6) and Eqn. (6.10), are both represented in linear time interval system, a system that behaves linearly with respect to time, the matched filter has to also be designed with linear time interval characteristics to be compatible with the model. For a 1-D linear time interval system, the system output $g(t)$ is the convolution (an integral which expresses the amount of overlap of one function, f, as it is shifted over another function, h, and thus blends one function with another) of the system input $f(t)$ with system unit impulse response, $h(t)$ (Buckley, 2000; and Rosen and Persaud, 2000):

$$g(t) = \int_{-\infty}^{\infty} f(t')h(t-t')dt' \tag{6.12}$$

The system unit impulse response, $h(t)$, which characterizes a linear time interval system, is the system response at $f(t) = \delta(t-t')$ and is expressed as follows:

$$[g(t)] = h(t) = \int_{-\infty}^{\infty} \delta(t-t')h(t-t')dt' \tag{6.13}$$

The matched filter is applied in three steps. Range compression first filters the transmitted radar signal response at a given time and assigns the correct range for a target point.

The second step, azimuth compression, involves applying another matched filter by the range-Doppler processing algorithm to identify the correct azimuth for that target point imaged.

Since the spacecraft moves along its trajectory while imaging a target point on surface, an additional step known as range migration is needed before starting the azimuth compression to account for this movement. All three steps will be explained in the following sections.

6.3.3. Range compression

Using the matched filter procedure, for transmitted radar signal $s_n(t)$, with response $r(s,t)$ associated with a point target at range ρ corrupted by noise, a filter is selected to identify a point target and allocate it to the correct range ignoring the azimuth dependence. In this case, the maximum matched filter response occurs at time $t = \tau$ associated with the range, ρ. Since this procedure is a linear time interval system, it can be characterized by its unit impulse response $h(t)$, which can be expressed as (Curlander and McDonough, 1991):

$$h(t) = s_n^*(-t) \tag{6.14}$$

Given this equation and the equation expressing the transmitted radar signal $s_n(t)$, the range compression matched filter, $h_r(t)$, can be expressed as follows (Buckley, 2000; and Rosen and Persaud, 2000):

$$h_r(t) = e^{-j\pi Kt^2} rect\left[\frac{t}{\tau_p}\right] \tag{6.15}$$

Substituting the point target response, $r(s,t)$, and the range compression matched filter $h_r(t)$ into the matched filter equation, and using the linear (FM) bandwidth Eqn. (6.8), the range compression matched filter output becomes (Buckley, 2000; and Rosen and Persaud, 2000):

$$g(s,t) = f_{WB} \sin c\{\pi f_{WB}[t - 2\rho(s)/c]\}e^{-j4\pi\rho(s)/\lambda} \tag{6.16}$$

Where

$$\sin c(x) = \frac{\sin x}{x}$$

Figure 6.9 illustrates the range-compressed point target response power centered at time t = τ. This range compressed point target response is associated with a slant range resolution δr, which can be determined using the following equation (Buckley, 2000):

$$\delta_r = \frac{c}{2f_{BW}} = \frac{c}{2|k|\tau_p} = \frac{c\Delta t_r}{2} \tag{6.17}$$

Where

Δt_r = Round trip time resolution

And

δ_r = One-way slant range resolution

This equation shows that the slant range resolution can be improved by increasing the radar pulses bandwidth, f_{BW}, or as the look angle is increased. One should be able to differentiate between the slant range resolution δr, which indicates the smallest object that can be picked out in the range direction, and the slant range sample

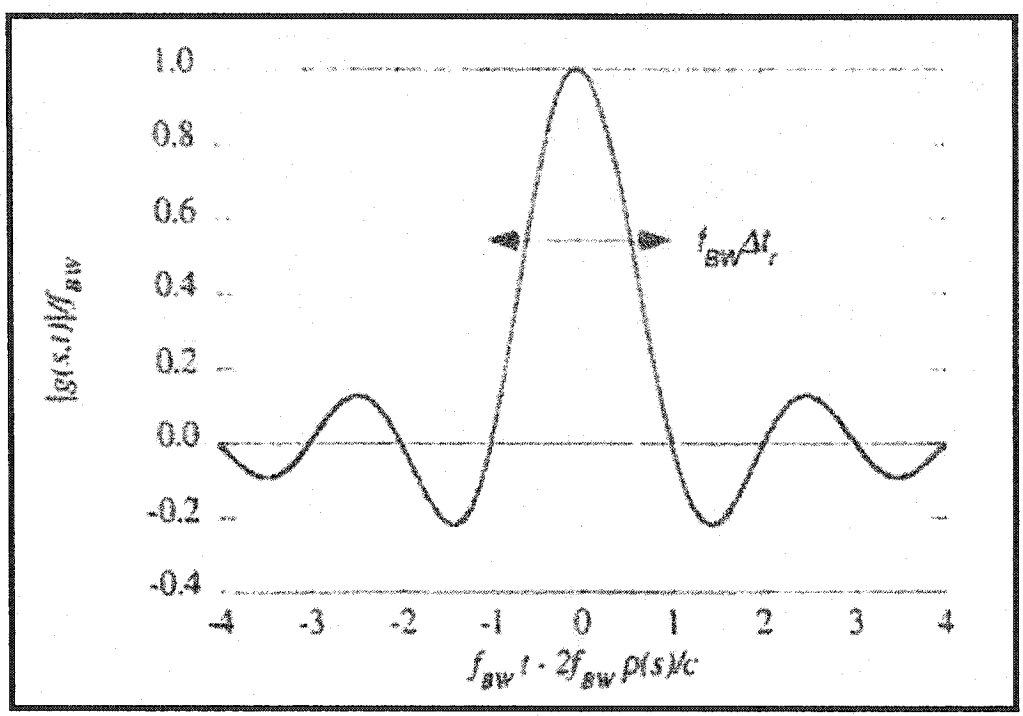

Figure 6.9: Range-compressed point target response modulus
(Source: After Buckley, 2000)

spacing Δr, the area each pixel covers, which can be determined using the following (Buckley, 2000; and Rosen and Persaud, 2000):

$$\Delta r = \frac{c}{2f_s} \tag{6.18}$$

Where

fs = Sampling frequency

And thus, one can notice that the range compression is the convolution of the raw data with the range reference function, which can be determined using a complex multiplication in the range frequency domain (Buckley, 2000; and Rosen and

Persaud, 2000). And thus, range compression can be performed by taking the FT of the range reference function and the one-dimensional FT (in range) of the raw data, multiplying the complex-conjugate transformed reference function and the raw data range transform, transforming the range-compressed data back to the time domain.

6.3.4. Doppler history

In order to resolve the azimuth location of the imaged target point on the surface, doppler shift history information are necessary so as to process data, used for interferometric applications, to the same doppler. This information is needed to estimate both the doppler centroid and doppler rate, which are used in both range migration and azimuth compression processes.

Since the doppler history of an imaged point target on the surface changes in both slow and fast time, the doppler is usually first modeled as a linear function of slow time, s, and the instantaneous doppler frequency may be expressed as (Buckley, 2000; and Rosen and Persaud, 2000):

$$f = f_{DC} + f_R(s - s_c) \tag{6.19}$$

Where,

f = Instantaneous doppler frequency = $\frac{\dot{\psi}}{2\pi} = \frac{-2\dot{\rho}(s)}{\lambda}$

f_{DC} = Doppler centriod, which is the doppler shift associated with a target at the synthetic aperture beam center.

f_R = Doppler rate = $\frac{\ddot{\psi}}{2\pi} = \frac{-2\ddot{\rho}(s)}{\lambda}$

And $\psi = \frac{-4\pi\rho(s)}{\lambda}$ = the phase associated with range compressed point response

The doppler centroid, f_{DC}, and doppler rate, f_R, can be determined using the orbit and altitude data, or can even be determined from the data itself in procedures know as clutter lock and autofocus. In this package, doppler centroid was estimated in an automated fashion, known as clutter lock (Curlander and McDonough, 1991), using the correlation doppler time domain estimator (CDE) proposed by Madsen (1989). The CDE depends on the direct relation between the phase of the correlation function and the doppler centroid and is applied to raw data (Madsen, 1989). Using the CDE algorithms results is a set of doppler centroid frequency versus slant range data points, where the doppler centroid is then modeled as a quadratic function of slant range.

Regression analysis is performed on the output data to determine the doppler centroid quadratic coefficients, which can be expressed as a function of slant range in the raw data (Buckley, 2000; and Rosen and Persaud, 2000):

$$f_{DC} = \tilde{f}_{DC0} + \tilde{f}_{DC1} b + \tilde{f}_{DC2} b^2 \tag{6.20}$$

Where,

$$b = \text{int}\left(\frac{\rho - \rho_0}{\Delta r}\right) \tag{6.21}$$

b = Range bin (numbered from zero)

ρ = Slant range from the antenna to range bin b

ρ0 = Slant range to the zero range bin (Slant range to the first pixel)

int( ) = Integer or truncation operator

The doppler coefficients can also be expressed in terms of slant range as follows (Buckley, 2000; and Rosen and Persaud, 2000):

$$f_{DC} = f_{DC0} + f_{DC1}\rho + f_{DC2}\rho^2 \tag{6.22}$$

Equating both f_{DC} equations, Eqn. (6.20) and Eqn. (6.22), for three b values (b=0, b=1, b=2, with corresponding slant range values of $\rho=\rho_0$, $\rho=\rho_0+\Delta r$, and $\rho=\rho_0+2\Delta r$), the bin-referenced doppler coefficients can be expressed in terms of the range-referenced doppler coefficients as (Buckley, 2000; and Rosen and Persaud, 2000):

$$f_{DC0} = f_{DC0} + f_{DC1}\rho_0 + f_{DC2}\rho_0^2 \tag{6.23}$$

$$f_{DC1} = (f_{DC1} + 2f_{DC2}\rho_0)\Delta r \tag{6.24}$$

$$f_{DC2} = f_{DC2}(\Delta r)^2 \tag{6.25}$$

In this package, the doppler rate, f_R, for a fixed point target on the earth surface is expressed as follows (Buckley, 2000; and Rosen and Persaud, 2000):

$$f_R = -2V_{eff}^{\ 2} / \lambda\rho \tag{6.26}$$

Where

ρ = Slant range from the antenna to the images target point

V_{eff} = Effective velocity related to the body-fixed spacecraft velocity

And

$\lambda = c/f_0$ = System wavelength

In this case, the component of the range dependent acceleration is neglected. For a better understanding of the relationships between doppler history, spacecraft orbit and altitude, one can refer to Curlander and McDonough (1991).

Since two raw SAR data sets have different doppler histories, it is really important to process the pair to the same doppler as processing them to different dopplers may result in the following (Buckley, 2000; and Rosen and Persaud, 2000):

1- The two images will have different geometries.
2- When generating an interferogram using these images, the doppler spectra of the images will not be aligned resulting in interferometric phase signature proportional to the difference in the doppler frequencies that must be removed from the interferogram.

Although processing the two sets of raw data to the same doppler may result in some errors in one or even both of the images, this error can be reduced in the last image formation process steps, known as azimuth compression.

6.3.5. Range migration

Since the spacecraft imaging the target on surface is moving, and thus the target response is distributed over several range bins, range migration is needed to account for this movement before starting the azimuth compression process. Range migration can be defined as a correction procedure, where the range associated with the point target response is adjusted to a constant.

The phase, ψ, associated with the range compressed point target can be expressed as (Buckley, 2000; and Rosen and Persaud, 2000):

$$\psi = -4\pi\rho(s)/\lambda \tag{6.27}$$

Here, s is range compressed point target. This phase can be used to determine the instantaneous doppler centroid, f_{DC}, and rate, f_R, which can be expressed as follows:

$$f_{DC} = \dot{\psi}/2\pi = -\dot{\rho}(s)/\lambda \tag{6.28}$$

$$f_R = \ddot{\psi}/2\pi = -2\ddot{\rho}(s)/\lambda \tag{6.29}$$

A second order Taylor series expansion about the slant range, ρ_c, its derivatives, and slow time, s_c, may be used to express the range to a target as:

$$\rho(s) \cong \rho_c + \dot{\rho}_c(s - s_c) + \frac{1}{2}\ddot{\rho}_c(s - s_c)^2 \tag{6.30}$$

ρ_c = Slant range associated with the target point

S_c = Slow time of range compressed target point

The above equation, illustrated in Figure 6.10, is valid when the target is at the center of the beam. The first and second derivatives of the range, ρ_c, may now be written as (Buckley, 2000; and Rosen and Persaud, 2000):

$$\dot{\rho}(s) = \dot{\rho}_c + \ddot{\rho}_c(s - s_c) \tag{6.31}$$

$$\ddot{\rho}(s) = \ddot{\rho}_c \tag{6.32}$$

$\dot{\rho}_c$ = Linear function of s

$\ddot{\rho}_c$ = Constant

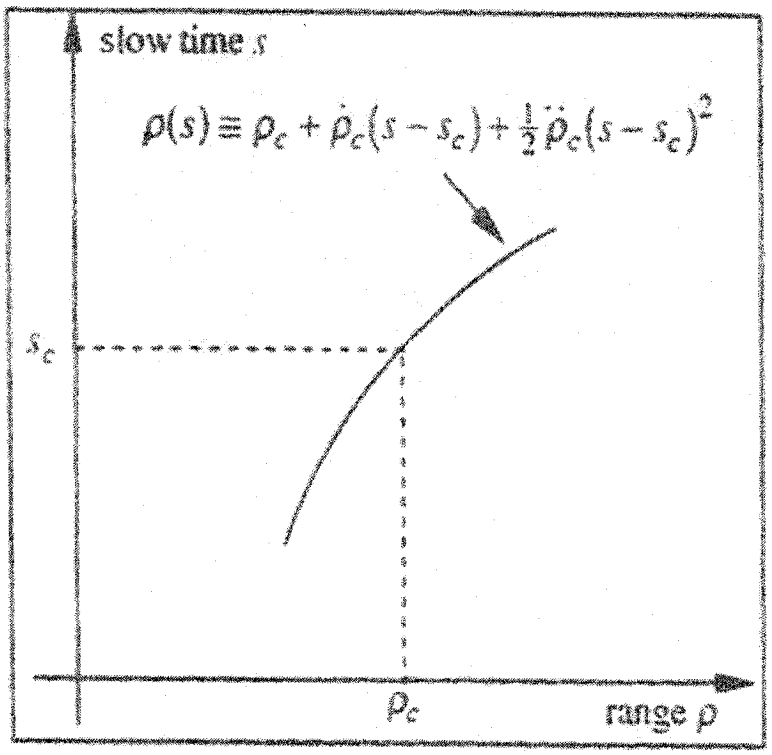

Figure 6.10: Point target range migration locus
(Source: After Buckley, 2000)

We can now express the doppler centroid, f_{DC}, and rate, f_R, in terms of the first and second derivatives of range, ρ_c, as follows:

$$f_{DC} = \frac{-2\dot{\rho}_c}{\lambda} + \frac{2\ddot{\rho}_c(s - s_c)}{\lambda} \tag{6.33}$$

$$f_R = \frac{-2\ddot{\rho}_c(s)}{\lambda} \tag{6.34}$$

Substituting Eqn. (6.33), and Eqn. (6.34) into Eqn. (6.30), the range derivatives can be expressed in terms of the Doppler centroid, f_{DC}, and rate, f_R, as follows:

$$\rho(s - s_c, s_c, \rho_c) = \rho_c - \frac{\lambda f_{DC}}{2}(s - s_c) - \frac{\lambda f_R}{4}(s - s_c)^2 \qquad (6.35)$$

It is important to note that both the Doppler centroid, f_{DC}, and rate, f_R, are functions of slow time and range to target and they change as the radar image different targets at different elevations through slow time (Buckley, 2000).

Since range migration, Δρ, is the range to the point target relative to the Synthetic Aperture beam center point target as the radar images target through time, it can be expressed as (Buckley,2000):

$$\Delta\rho = \rho(s - s_c, s_c, \rho_c) - \rho_c = -\frac{\lambda f_{DC}}{2}(s - s_c) - \frac{\lambda f_R}{4}(s - s_c)^2 \qquad (6.36)$$

This shows that as the wavelength, λ, increase, range migration increase.

6.3.6. Azimuth compression

After applying range compression followed by a range migration procedure on the data, the azimuth compression procedure must be applied to fully resolve the location of the target on the formed image. The azimuth compression matched filter unit impulse response, $h_a(s)$, is referred to as the azimuth reference function and can be expressed as follows (Buckley, 2000; and Rosen and Persaud, 2000):

$$h_a(s) = e^{j2\pi(f_{DC}s - \frac{1}{2}f_R s^2)} rect\left[\frac{s}{\tau_a}\right] \qquad (6.37)$$

Where

$$\tau_a = \lambda\rho_c / 2V_{st}\delta_a \qquad (6.38)$$

$$\delta_a \geq {}^{L_a}\!/_{2} \tag{6.39}$$

s = Measured relative to s_c

τ_a = Synthetic aperture duration, the time for a target to move through the illumination beam

V_{st} = Spacecraft speed relative to the point target

L_a = Antenna size in the along-track direction

And

δ_a = Desired azimuth resolution (theoretical limit = La/2)

One can notice that increasing azimuth resolution, δ_a, for a given wavelength and spacecraft velocity, reduces the synthetic aperture duration, τ_a. After applying azimuth compression, the modulus of the point target response can be expressed as (Buckley, 2000; and Rosen and Persaud, 2000):

$$|g(s)| = B_D \sin c(\pi B_D s) \tag{6.40}$$

Where

$$B_D = |f_R|\tau_a \tag{6.41}$$

And

B_D = Doppler bandwidth

And thus, the azimuth resolution, δ_a, can be expressed as:

$$\delta_a = V_{st}\delta_s = V_S + B_D^{-1} = \frac{V_{st}}{|f_R|\tau_a} \tag{6.42}$$

Where

δ_s = Azimuth filter output main lobe half-power width $= \frac{1}{B_D}$

So it can be noticed that finer azimuth resolution results for large doppler bandwidths is achieved using longer Synthetic Aperture antenna (Buckley, 2000). Figure 6.11 illustrates the azimuth spectra associated with a radar interferometry pair.

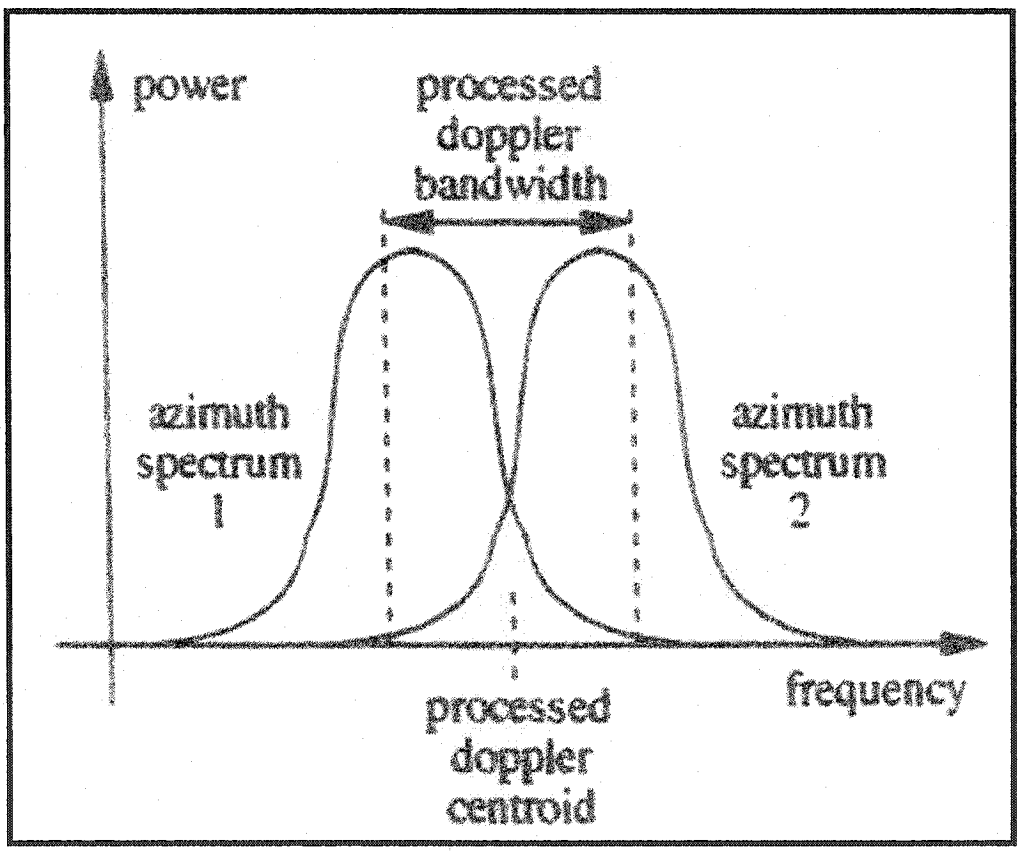

Figure 6.11: Azimuth spectra associated with radar interferometry pair (Source: After Buckley, 2000)

In summary, this section covered a brief explanation of the steps involved in the image formation process starting with range compression, where a filter is selected to identify a point target and allocate it to the correct range, followed by a range migration process, where the resultant range is corrected taking into account the movement of the space craft while imaging the target on surface, and finally azimuth compression to fully resolve the pixel location of an imaged target point.

6.4. Image registration

Since the relative range to an imaged target on a pair of SAR images depend on topography and baseline, in this step, both the master and slave images formed in the image formation process have to be co-registered before starting the interferogram formation process. This step determines the mapping of pixel locations of common targets from the master and slave image with considerations to shifts and distortions due to imaging system geometry and inherent limitations (Burgmann et a., 2000). The registration process requires the use of a set of range and azimuth offset measurements for each patch to estimate a functional mapping in order to resample the slave image to the master image and align them. An amplitude correlation procedure is implemented on a regular grid across the image to estimate a set of both range and azimuth offset measurements. The master image is divided into patches of 64 x 64 pixels, whereas the slave image is divided into chips of 124 x 124 pixels (64 pixel plus a 30-pixel pull-in on either side). Each patch includes real valued amplitudes determined from the single look complex (SLC) SAR image generated earlier. Since the master image patches are smaller in size than that of the slave

image, a normalized cross-correlation surface between the slave image patch and several master image patches, within the slave image patch, is computed and thus a peak correlation value is estimated. It is important to note that an edit criterion is used to make sure of identifying patches with peak correlation SNR greater than a given threshold as well as a covariance less than a specific threshold in order to deramp and over sample them by a factor of two and implement correlation procedure on them again (Buckley, 2000; and Rosen and Persaud, 2000). The registration process results in a real valued range and azimuth offsets as an output.

In ROI_PAC, the slave image range offset, $\Delta\rho$, and azimuth offset, Δa, were modeled as polynomial functions of the range and azimuth pixel location (x, y) in the master image (Buckley, 2000; and Rosen and Persaud, 2000):

$$\begin{aligned}\Delta\rho &= C_1^\rho + C_2^\rho x + C_3^\rho y + C_4^\rho xy + C_5^\rho x^2 + C_6^\rho y^2 \\ &+ C_7^\rho xy^2 + C_8^\rho x^2 y + C_9^\rho x^3 + C_{10}^\rho y^3 \\ \Delta a &= C_1^a + C_2^a x + C_3^a y + C_4^a xy + C_5^a x^2 + C_6^a y^2 \\ &+ C_7^a xy^2 + C_8^a x^2 y + C_9^a x^3 + C_{10}^a y^3\end{aligned} \tag{6.43}$$

Where,

C_i^ρ = Range offset fit coefficients

C_i^a = Azimuth offset fit coefficients

A single value decomposition procedure is used to determine such fit coefficients utilizing their reduced set of offset measurements. The above equations are used to determine the range and azimuth offsets for a given pixel in the master image, add these offsets to the master image pixel location and thus determine the location of

that pixel on the slave image. Using the above procedure results in both integer and fraction parts representing location on the slave image, where the integer portion is used to determine the amount of shifting to the slave image location, whereas the fractional part is used for interpolating and thus an exact complex pixel value is estimated (Buckley, 2000; and Rosen and Persaud, 2000).

This step is considered important as trying to generate an interferogram from a pair of unregistered images will result in errors due to the fact that the random backscatter phase contribution from each collection of scatterers wont destructively cancel each other (Burgmann et al., 2000).

6.5. Interferogram formation

To form an interferogram, complex pixel of the master image is multiplied by the complex conjugate of the same pixel in the slave image (Burgmann et al., 2000). Prior to the interferogram formation process, one should keep in mind that the difference in look angle between the two acquired radar images results in a shift in the frequency reflectivity,Δf, which should be accounted for and corrected. This problem, which is known as the wave number or spectral shift between the pair of SAR images, adds noise to the generated interferogram. Such noise can be reduced by spectrally filtering both images prior to generating the interferogram and is done in range by shifting each image spectra toward the other by half the total frequency shift and truncating the non-overlapping portion (Gatelli et al., 1994; Buckley, 2000; and Rosen and Persaud, 2000). Spectral filtering is implemented in ROI_PAC, where spectral shift is executed with a complex modulation of both complex images

removing phase ramp. On the other hand, truncation of the shifted images was implemented with a Hamming weight function (Buckley, 2000; and Rosen and Persaud, 2000). Generating the interferogram is then performed by cross-multiplication of pixels and is completed by re-entering the removed phase ramp and thus preserving the phase and range difference between the two images relationship. The interferogram, a complex image itself, contains phase information, which represent the difference of the signal phases that records the topography and the deformation between the two acquisition times. Although the resulting interferogram contains phase due to topography as well as deformation between the two scenes, the interferogram also has a dominant phase due to the elliptical shape of earth. This dominating signal should be removed by interferogram flattening and thus an accurate estimation of interferometric baseline is required.

6.6. Baseline determination

After interferogram formation and flattening, phase due to topography should be estimated and removed in order to determine the phase due to the deformation of interest. This procedure involves the determination of an interferometric baseline, which directly affects the degree to which surface topography contributes to the interferometric phase resulted. Errors in estimating the exact interferometric baseline leads to residual topographic fringes in the differential interferogram and thus results in wrong deformation estimations.

To better understand the interferometric baseline (Figure 6.12), which is defined as the difference between the location of the two antenna phase center vectors at the

time when a given scatterer is imaged (Rosen et al., 2000), consider a point target on the surface imaged by two different satellites (Buckley, 2000; and Rosen and Persaud, 2000):

$$\vec{T} = \vec{P}1 + \rho_1 \hat{l}1 = \vec{P}2 + \rho_2 \hat{l}2 \qquad (6.44)$$

Where

$\vec{T}$ = Target position vector

$\vec{Pi}$ = Reference position for the platform (usually position of one of the imaging antenna's)

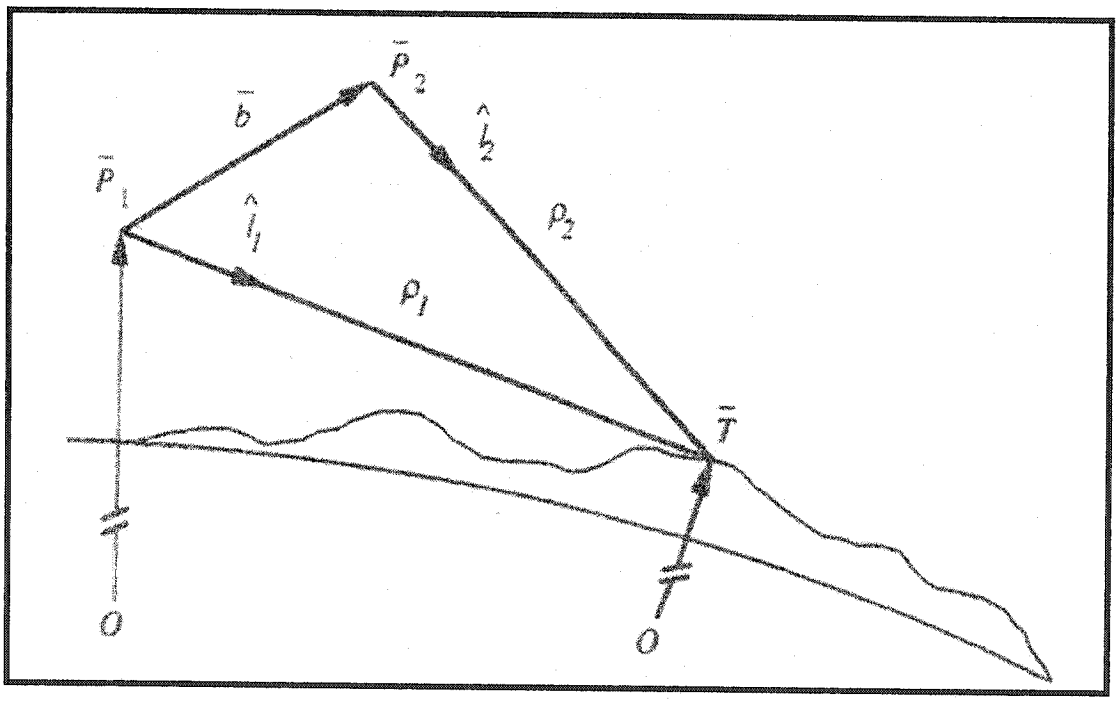

Figure 6.12: Interferometric baseline geometry
(Source: After Buckley, 2000)

ρ_i = Antenna i range to target

$\hat{l}\,i$ = Unit look vector from antenna i to the target

And

i = 1 and 2, representing the two antennas imaging the target point

And thus the baseline, which is a function of both time and target position, can be expressed as follows:

$$\vec{b} = \vec{P}2 - \vec{P}1 = \rho_1 \hat{l}1 - \rho_2 \hat{l}2 \tag{6.45}$$

This means that the interferometric baseline is a function of time (through the antenna positions) and target position (Buckley, 2000).

6.6.1. Baseline in $\hat{S}\hat{C}\hat{H}$ coordinates

To further explain the interferometric baseline determination procedure, baseline is defined using $\hat{S}\hat{C}\hat{H}$ coordinates, where $\hat{S}$ stands for the along track direction, $\hat{C}$, is cross track direction, and $\hat{H}$ is in the vertical direction (perpendicular to along-track direction). This system was developed to take advantage of the along-track (azimuth) and across-track (range) radar geometry and is well suited for radar interferometry height reconstruction problem. To better understand SCH coordinates and how to convert between SCH and Cartesian coordinates systems, one can refer to Hensley et al. (1996), Hensley and Rosen (1996), and Holecz et al. (1996).

Figure 6.13 illustrates the geometry of imaging radar in the SCH coordinate system. The unit-look vector, $\hat{l}_i^{SCH_i}$, associated with antenna i to the target in SCH coordinates may be expressed as (Rosen et al., 2000; Buckley, 2000; and Rosen and Persaud, 2000):

$$\hat{l}_i^{SCH_i} = \begin{bmatrix} l_i^{S_i} \\ l_i^{C_i} \\ l_i^{H_i} \end{bmatrix} = \begin{bmatrix} \cos\theta_i \sin\gamma_i \cos\beta + \sin\theta_i \sin\beta \\ -\cos\theta_i \sin\gamma_i \sin\beta + \sin\theta_i \cos\beta \\ -\cos\theta_i \cos\gamma_i \end{bmatrix} \tag{6.46}$$

Where

θ_i = Look angle associated with antenna i

γ_i = Pitch angle associated with antenna i

β = Azimuth angle

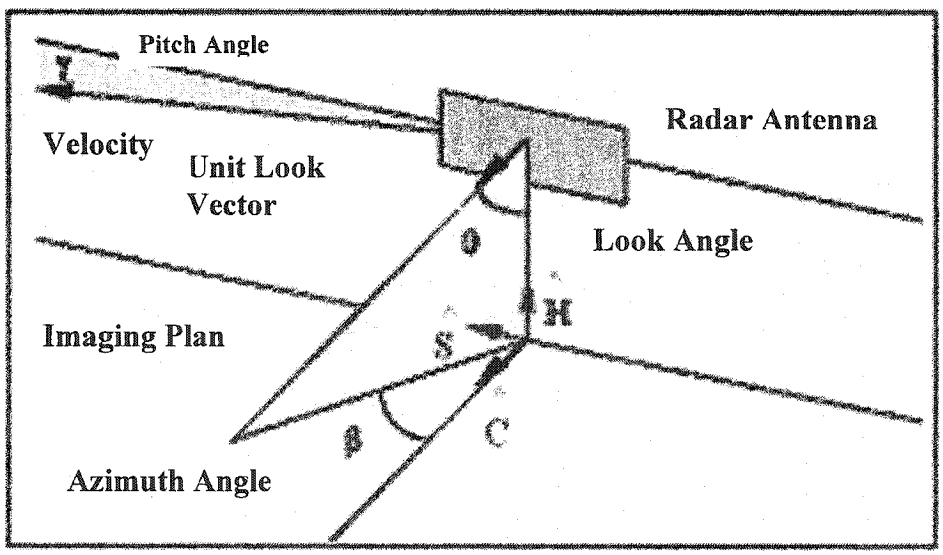

Figure 6.13: Radar imaging geometry in SCH coordinate system (Source: After Buckley, 2000; and Rosen and Persaud, 2000)

And a left looking geometry has been assumed (Buckley, 2000; and Rosen and Persaud, 2000). Given the above, the unit-look vectors for antennas 1 and 2 can be expressed as follows (Buckley, 2000; and Rosen and Persaud, 2000):

$$\hat{l}_1^{SCH_1} = \begin{bmatrix} \sin\theta_1 \sin\beta \\ \sin\theta_1 \cos\beta \\ -\cos\theta \end{bmatrix} \tag{6.47}$$

$$\hat{l}_2^{SCH_2} = \begin{bmatrix} \cos\theta_2 \sin\gamma \cos\beta + \sin\theta_2 \sin\beta \\ -\cos\theta_2 \sin\gamma \sin\beta + \sin\theta_2 \cos\beta \\ -\cos\theta_2 \cos\gamma \end{bmatrix} \tag{6.48}$$

It can be noticed that in the above equations, the pitch angle γ_1, associated with antenna 1 is assumed to be zero and thus the subscript is dropped from the antenna 2 pitch angle so γ is used instead of γ_2. A simple rotation is applied to Eqn. (6.48) in order to express the unit look vector associated with antenna 2, γ, in the antenna 1 SCH coordinates (Buckley, 2000; and Rosen and Persaud, 2000):

$$\hat{l}_2^{SCH_1} = M_{SCH_2}^{SCH_1} \hat{l}_2^{SCH_2} \begin{bmatrix} \cos\theta_2 \sin\gamma \cos(\beta-\eta) + \sin\theta_2 \sin(\beta-\eta) \\ -\cos\theta_2 \sin\gamma \sin(\beta-\eta) + \sin\theta_2 \cos(\beta-\eta) \\ -\cos\theta_2 \cos\gamma \end{bmatrix} \tag{6.49}$$

Where

$$M_{SCH_2}^{SCH_1} = \begin{bmatrix} \cos\eta & -\sin\eta & 0 \\ \sin\eta & \cos\eta & 0 \\ 0 & 0 & 1 \end{bmatrix} \tag{6.50}$$

Where η is the divergence angle from antenna's 1 and 2 tracks in SCH plan. Its next assumed that the divergence angle, η, the pitch angle, γ, and the azimuth angle, β, are small, which are valid assumption for the ERS SAR system antennas, and thus:

$$\tan \eta \approx \sin \eta \tag{6.51}$$

$$\tan \gamma \approx \sin \gamma \tag{6.52}$$

$$\cos \beta \approx 1 \tag{6.53}$$

$$\cos (\beta - \eta) \approx 1 \tag{6.54}$$

Finally, the baseline, for antenna 1 in SCH coordinates, can be determined by substituting both Eqn. (6.47) and (6.49) along with the above approximations (Eqn. (6.51)-(6.54)) into the baseline Eqn. (6.45) can be expressed as follows:

$$\vec{b} = \begin{bmatrix} b_S \\ b_C \\ b_H \end{bmatrix} = \begin{bmatrix} b_C \tan\beta + \rho_2 \sin\theta_2 \tan\eta - \rho_2 \cos\theta_2 \tan\gamma \\ \rho_1 \sin\theta_1 \cos\beta - \rho_2 \sin\theta_2 \cos\beta \cos\eta \\ -\rho_1 \cos\theta_1 + \rho_2 \cos\theta_2 \cos\gamma \end{bmatrix} \tag{6.55}$$

The along-track component of the baseline in Eqn. (6.55) is referred as the target dependent along-tack offset, Δ_{ST}, (Figure 6.14) and can be expressed as follows (Buckley, 2000; and Rosen and Persaud, 2000):

$$\Delta_{ST} = b_c \tan\beta + \rho_2 \sin\theta_2 \tan\eta - \rho_2 \cos\theta_2 \tan\gamma \tag{6.56}$$

Since it is simpler to express the baseline as a function of along-track single variable, *S*, that takes into account time and target dependent portions of baseline, and components in both across-track, C, and vertical direction, H, are assumed to vary linearly with S, a modified baseline model can be expressed as (Buckley, 2000; and Rosen and Persaud, 2000):

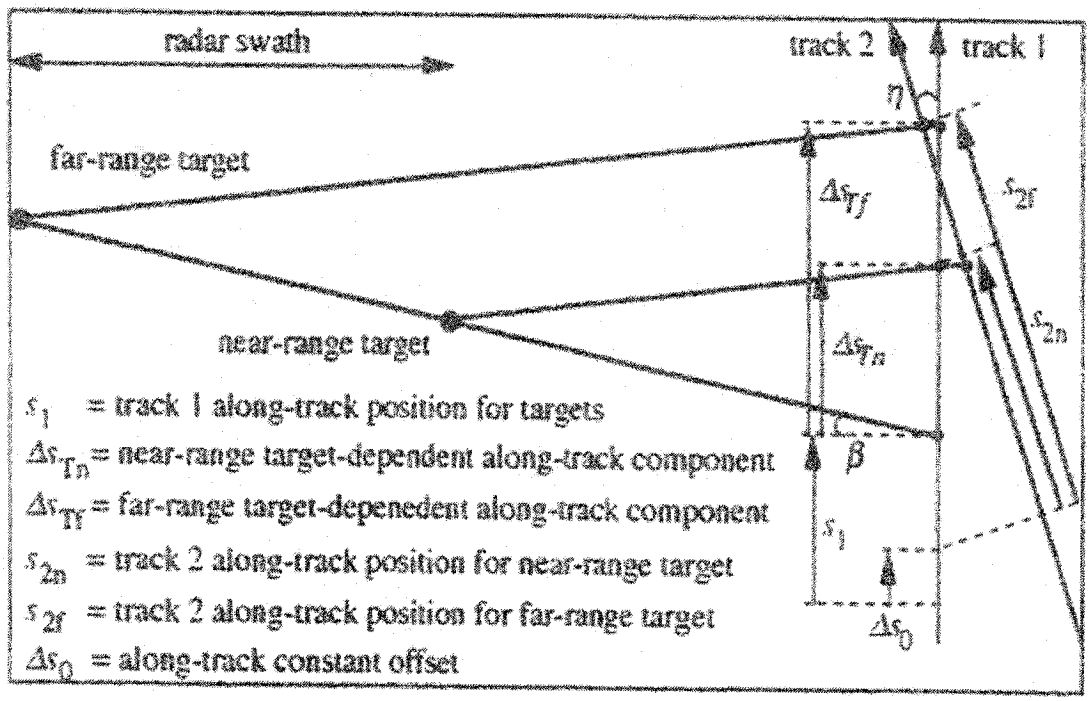

Figure 6.14: Repeat-pass imaging geometry projected into the SC-plane (Source: After Buckley, 2000)

$$\vec{b}' = \vec{b} - \begin{bmatrix} \Delta_{ST} \\ 0 \\ 0 \end{bmatrix} = \begin{bmatrix} 0 \\ b_C \\ b_H \end{bmatrix} = \begin{bmatrix} \Delta_{S0} + (ks_2 - s_1) - \Delta_{sT} \\ b_{C0} + \dot{b}_C (s_1 + \Delta_{sT}) \\ b_{H0} + \dot{b}(s_1 + \Delta_{sT}) \end{bmatrix} \tag{6.57}$$

Where

Δs_0 = Along-track constant offset

k = Along-track scale factor between s_1 and s_2 coordinates

b_{C0} = Initial cross-track baseline

b_{H0} = Initial vertical baseline

$\dot{b}_C$ = Cross-track baseline rate of change

And

$\dot{b}_H$ = Vertical baseline rate of change

Substituting the along-track variable, $s = s_1 + \Delta s_T$, the baseline model is expressed as:

$$\vec{b}'(s) = \begin{bmatrix} 0 \\ b_C(s) \\ b_H(s) \end{bmatrix} = \begin{bmatrix} \Delta_{S0} + (ks_2 - s) \\ b_{C0} + \dot{b}_C s \\ b_{H0} + \dot{b}_H s \end{bmatrix} \tag{6.58}$$

And thus the target dependent along-track offset, Δs_T, is expressed, using baseline rate of change shown in Figure 6.15, as:

$$\Delta_{ST} = b_C \tan\beta + \dot{b}_C \rho_2 \sin\theta_2 - \dot{b}_H \rho_2 \cos\theta_2 \tag{6.59}$$

Where

$\dot{b}_C = \tan\eta$ And $\dot{b}_H = \tan\gamma$

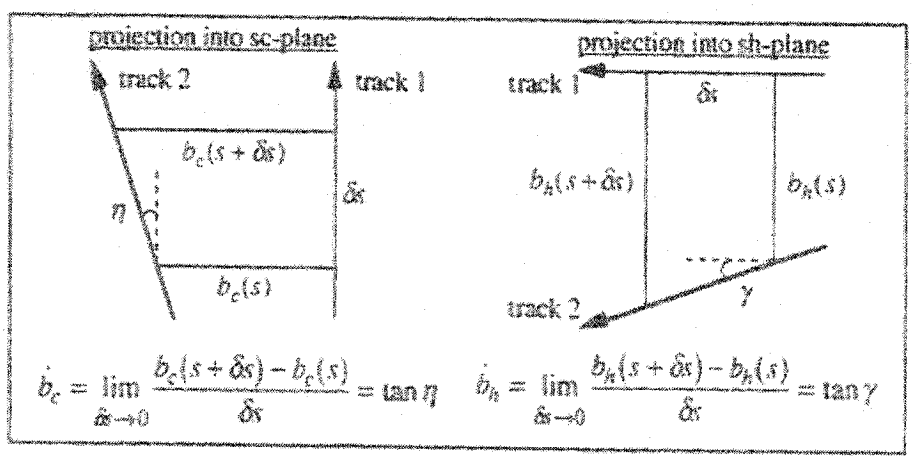

Figure 6.15: Baseline rates of change geometry
(Source: After Buckley, 2000)

6.7. Interferogram flattening

As was mentioned earlier in this chapter, when an interferogram is generated from a pair of SAR images, the dominant interferometric signal resulting is that due to the elliptical shape of earth. To better estimate the interferometric phase due to the deformation of interest, phase due to the ellipsoid shape of earth must be first removed. This is done in a process known as interferogram flattening, which is defined as the linearization of the interferometric phase about the reference surface that results in the subtraction of phase due to the reference surface from the interferogram (Buckley, 2000; and Rosen and Persaud, 2000). Table 6.3 lists the steps involved in the interferogram flattening process along with equations used before processing each step, where i is the number of range samples, j_a is the number of azimuth lines, ρ_0 is the range to the first range sample, and Δ_r is the range sample spacing.

In the following equations:

Δ_a = Azimuth line spacing

h = Spacecraft height above the reference surface

r = Radius of spherical earth

Φ_{ref} = Interferometric phase due to the reference surface

$C\phi_{ref}$ = Complex interferogram due to the reference surface

$C\phi$ = Complex interferogram

And $C\phi_{flat}$ = Complex flattened interferogram

Flattening Step	Equations used
1- Compute ρ_1, s_1, h	$\rho_1 = \rho_0 + (i-1)\Delta_r$ $s_1 = (j_a - 1)\Delta_a$ $h = h_0 + \dot{h}_{s1} + \ddot{h}_{s1}$
2- Compute ρ_2 ($\Delta\rho_{ref}$=0 first time around)	$\rho_2 = \rho_1 + \Delta\rho_0 + \Delta\rho_{ref}$
3- Compute θ_{1ref}, θ_{2ref}, approximate b_C, b_S Where l= 1,2	$\cos\theta_{lref} = \frac{\rho_1^2 + (r+h)^2 - r^2}{2\rho_l(r+h)}$ $b_C \approx b_{C0} + \dot{b}_C s1$ $b_S = \Delta_{ST} = b_C \tan\beta + \dot{b}_C \rho_2 \sin\theta_2 - \dot{b}_H \rho_2 \cos\theta_2$
4- Compute b_C, b_H, b, $\hat{l}_{1ref} . \vec{b}$, approximate $\Delta\rho_{ref}$	$b_C = b_{C0} + \dot{b}_C(s1 + \Delta_{ST})$ $b_H = b_{H0} + \dot{b}_H(s1 + \Delta s_T)$ $b = \sqrt{b_S^2 + b_C^2 + b_H^2}$ $\hat{l}_{1ref} . \vec{b} = b_S \sin\theta_{1ref} \sin\beta + b_C \sin\theta_{1ref} \cos\beta - b_H \cos\theta_{1ref}$ $\Delta\rho_{ref} = \rho_1 \left(\sqrt{1 - 2\left(\hat{l}_{1ref} . \vec{b}\right)\rho_1^{-1} + b^2\rho_1^{-2}} - 1 \right)$

Table 6.3: Interferogram flattening procedure steps
(Source: Modified after Buckley, 2000; and Rosen and Persaud, 2000)

Flattening Step	Equations used
5- Repeat steps 2-4 for new $\Delta\rho_{ref}$	-
6- Compute phase Φ_{ref}, from complex number	$\phi_{ref} = (4\pi / \lambda)\Delta\rho_{ref}$ $C\phi_{ref} = \cos\phi_{ref} + j\sin\phi_{ref}$
7- Conjugate multiplication	$C\phi_{flat} = C\phi C\overset{*}{\phi}_{ref}$
8- Repeat steps 1-7 for all range bin in given azimuth line	-
9- Repeat steps 1-8 for all azimuth lines	-

Table 6.3 continued: Interferogram flattening procedure steps
(Source: Modified after Buckley, 2000; and Rosen and Persaud, 2000)

ROI_PAC implements interferogram flattening by first using the baseline estimated from the registration offsets. The phase is later unwrapped and used to estimate an improved baseline. The last step in this process involves using the estimated improved baseline to flatten the original interferogram. Although this process removes most of the phase due to the spherical shape of earth, there may still be a residual tilt in the interferometric phase that should be removed empirically by relying on observation and experiment.

6.8. Correlation determination

While the phase of the complex valued cross correlation of a pair of radar signals is related to the interferometric phase, the amplitude is related to the correlation coefficient (Buckley, 2000; and Rosen and Persaud, 2000). Noise, which can be considered as random fluctuations in the radar backscattered signal, effects the estimation of correlation coefficients leading to values way below the perfect

correlation value of one, and thus results in interferometric decorrelation which leads to treatment of both master and slave signals, C_1 and C_2, as random processes.

Generally speaking, the standard measure of the degree of statistical similarity of two random process signal used to generate an interferogram measurement is the complex cross-correlation or coherence, γ, and is defined as (Rosen et al., 2000):

$$\gamma = \frac{\left\langle C_1 C_2^* \right\rangle}{\sqrt{\left\langle C_1 C_1^* \right\rangle \left\langle C_2 C_2^* \right\rangle}} = \frac{E\left[C_1 C_2^*\right]}{\sqrt{E\left[C_1 C_1^*\right] E\left[C_2 C_2^*\right]}} \tag{6.60}$$

Where

C_i = Image phase measurement at antenna i,

E[C]= expected value of random process C (statistical or ensemble average)

And

<C> = Time average of random process C

The above equation assumes that both C1 and C2 are ergodic processes in which statistical or ensemble averages of the random processes are equivalent to time averages of the random processes (Ziemer and Tranter, 1995; Buckley, 2000; and Rosen and Persaud, 2000). This means that a spatial average of a single realization in time can be used to determine the coherence. It is important to note that a correlation coefficient, γ =1, represents completely coherent scatterers, whereas γ = 0, indicates an independent scattered fields (Rosen et al., 2000).

The correlation coefficient, $|\gamma|$, which is defined as the amplitude of the complex

coherence, at a given pixel is, estimated over a window of size N as a weighted spatial average (Hagberg et al., 1995; Rosen et al., 2000; Buckley, 2000; and Rosen and Persaud, 2000):

$$|\gamma| = \frac{|C_{12}|}{\sqrt{C_{11}}\sqrt{C_{22}}} \tag{6.61}$$

Where

$$C_{12} = \sum_{k=0}^{N-1}\sum_{j=0}^{N-1} w_N(k,j)C_1(k,j)\overset{*}{C_2}(k,j)C_D(k,j) \tag{6.62}$$

$$C11 = \sum_{k=0}^{N-1}\sum_{j=0}^{N-1} w_N(k,j)C_1(k,j)\overset{*}{C_1}(k,j) \tag{6.63}$$

$$C_{22} = \sum_{k=0}^{N-1}\sum_{j=0}^{N-1} w_N(k,j)C_2(k,j)\overset{*}{C_2}(k,j) \tag{6.64}$$

Where

W_N = Scalar weighting array of window size N

C_D = Complex parameter used to detrend the interferometric phase in the window

The local phase slope is thus removed using the complex parameter, C_D, which if existed could affect the estimated correlation.

The same windowing and weighting process is used to estimate the local phase slopes associated with each pixel from the flattened interferogram. ROI_PAC uses a normalized Gaussian low pass filter in the scalar weighting process, which can be expressed as (Buckley, 2000; and Rosen and Persaud, 2000):

$$W_N(j,k) = w_N(k,j) \Big/ \sum_{k=0}^{N-1} \sum_{j=0}^{N-1} w_N(k,j), \qquad j,k = 0, \ldots, N\text{-}1 \tag{6.65}$$

Where

$$W_N(j,k) = e^{-\left[(k-M)^2 + (j-M)^2\right]/M} \tag{6.66}$$

$$M = \text{int}(N/2) \tag{6.67}$$

Studies by Rodriguez and Martin in 1992 had shown that as the number of looks, N_L, used to generated an interferogram increases, the interferometric standard deviation, σ_ϕ, of the interferometric phase progressively approaches a lower bound on the phase variance in terms of the correlation, which can be expressed as (Buckley, 2000; Rosen et al., 2000; and Rosen and Persaud, 2000):

$$\sigma_\phi = \frac{1}{\sqrt{2N_L}} \frac{\sqrt{1-|\gamma|^2}}{\gamma} \tag{6.68}$$

One can notice that as the correlation coefficient decreases, the interferometric phase standard deviation, σ_ϕ, increases leading to complications in the phase unwrapping process, which could also lead to unwrapping errors. To over come this problem, a correlation threshold is chosen and the phase of only those pixels with interferometric phase standard deviation larger than the value of the threshold are unwrapped. Another approach of solving such complication is applying a filtering process to filter the interferogram, a step that will be further explained in the upcoming section.

6.9. Interferogram filtering

Since in a radar image, the observed surface backscatter results due to the coherent summation of individual scatterers within a particular resolution cell leading to an interferometric phase dominated with a single fringe frequency, which means that the generated interferogram power spectra will contain both narrow-band signal and broad-band noise. A process, known as interferogram filtering, is used to remove this type of noise. Regions of high deformations include increased phase due to noise as well as high local fringe rates, which if not carefully filleted, would cause errors in the unwrapping process (Goldstein and Werner, 1998).

ROI_PAC interferogram filtering process implements algorithms of a nonlinear spectral filter, know as power spectrum adaptive filter, designed by Goldstein and Werner, 1998. In this process, the local interferogram power spectrum is filtered to increase the signal to noise ratio. Power spectrum of a random signal can be estimated using DFT, which utilizes periodogram analysis, a process where the power spectrum estimator is the so-called periodogram (Buckley, 2000). The periodagram is the square of the magnitude of the two dimensional DFT, I (u, v), of interferogram I (x, y). (u, v) here are the frequencies associated with the range and azimuth coordinates (x, y). The interferogram I (x, y), is split into overlapping rectangular patches where a single periodagram is computed for each patch. The power spectrum estimate is then smoothed and the linear filter, Z (u, v), is constructed as follows (Buckley, 2000; and Rosen and Persaud, 2000):

$$Z(u,v) = \left| \hat{C}(u,v) \right|^{\alpha} \tag{6.69}$$

Where

α = Filter weight

If α is set to zero, no filtering occur, whereas when it is set to a value larger than zero, filtering occurs and increases with the increase of the value of α used. Goldstein and Werner (1998), states that useful values of α lie between 0.2 and 1.

Finally, the filtered interferogram $\hat{I}(x,y)$ is determined as follows (Buckley, 2000):

$$\hat{I}(x,y) = FT^{-1}\left\{ \tilde{I}(u,v) Z(u,v) \right\} \tag{6.70}$$

Where FT^{-1} = Two-dimensional inverse Fourier transform

Since this procedure is repeated for all the generated interferogram patches, the patches are overlapped and a triangular weighted sum of the overlapping patches is used to minimize or eliminates discontinuities at patch boundaries (Goldstein and Werner, 1998; Buckley, 2000; and Rosen and Persaud, 2000).

One hindrance of such process, is that it poorly effects and decreases the bandwidth associated with both range and azimuth coordinates. It is important to keep in mind taking into account the non-stationary power spectrum, which lead to spatially changing fringe frequency when choosing a filtering method (Buckley, 2000; and Rosen and Persaud, 2000).

6.10. Phase unwrapping

At this stage, and after all the previous processes are performed on the generated interferogram, the resulting interferometric phase, or so known as measured interferometric phase, must be further processed to generate the absolute interferometric phase which is directly related to the topographic height and amount of deformation of interest. Measured interferometric phase represents the absolute interferometric phase only modulo 2π, meaning that an integral number of phase cycles on each measurement is lost (Zebker and Lu, 1998). And thus, to determine the absolute phase, the measured phase must be unwrapped and an absolute phase must be determined. The relationship between measured, $\phi_{measured}$, unwrapped, $\phi_{unwrapped}$, and absolute, $\phi_{absolute}$, interferometric phases can be expressed as follows (Goldstein et al., 1988; and Madsen and Zebker, 1992):

$$\phi_{measured} = \mathrm{mod}(\phi_{absolute}, 2\pi) \tag{6.71}$$

$$\phi_{unwrapped} = (\phi_{measured})_{unwrapped} = \phi_{absolute} + 2\pi n \tag{6.72}$$

$$\phi_{absolute} = \frac{4\pi}{\lambda}\delta\rho \tag{6.73}$$

Where

n = An integer

$\delta\rho$ = Represents one-way path length difference due to topography and deformation

And

$(\,)_{unwrapped}$ = Phase unwrapping process

ROI_PAC implements an unwrapping algorithm known as the residue-cut tree algorithm, where the absolute interferometric phase is determined by first differentiating the measured phase followed by an integration of resultant phase gradient. This algorithm, developed by Goldstein et al., 1988, and known as GZW algorithm, is applied to pixels with correlation coefficient value above a chosen threshold and is divided into three steps:

1- Residue identification

2- Residue connection

3- Integration

The algorithm assumes that radar sampling was performed in such a way that the unwrapped phase from one pixel to the next will vary by no more than one-half of a cycle, $+\pi$ or $-\pi$, and thus unwrapped phase varying by more than one-half of a cycle is considered as residues.

So the algorithm first identifies the location of all residues in the generated interferogram and marks them as positive or negative, connects the residues with branch cuts in order to prevent the existence of non-neutral integration paths and thus ensure consistency (Zebker and Lu, 1998).

The goal of residue connection is to connect residues with branch cuts in order to arrive to an overall neutral charge for the connections network, referred to as the tree, which are used to eliminate full cycle phase discontinuities along closed paths when integrated (Buckley, 2000; and Rosen and Persaud, 2000).

In Residue connection process, the length of branch cuts in a given tree are kept to a minimum and thus leads to minimum number of half cycle discontinuities. Thus residue calculations considering the following general subset of measured phase values may be expressed as follows (Goldstein et al., 1988; Buckley, 2000; Rosen et al., 2000; and Rosen and Persaud, 2000):

$$\begin{bmatrix} \phi(i,j) & \phi(i,j+1) \\ \phi(i+1,j) & \phi(i+1,j+1) \end{bmatrix} \tag{6.74}$$

Where residue assigned to pixel (i, j) associated with the above values is expressed as (Goldstein et a., 1988; Buckley, 2000; and Rosen and Persaud, 2000):

$$residue(i,j) = \frac{1}{2\pi}\left[\Delta\Phi_i(i,j) - \Delta\Phi_j(i,j)\right] \tag{6.75}$$

Where

$$\Delta\Phi_i(i,j) \equiv \Phi_i(i,j+1) - \Phi_i(i,j) \tag{6.76}$$

$$\Delta\Phi j(i,j) \equiv \Phi_j(i+1,j) - \Phi_j(i,j) \tag{6.77}$$

$$\Phi_i(i,j) \equiv \Phi(i+1,j) - \Phi(i,j) \tag{6.78}$$

$$\Phi j(i,j) \equiv \Phi(i,j+1) - \Phi(i,j) \tag{6.79}$$

Residue calculations using the above method can yield in either a value of zero, indicating no residue, a value of +1, indicating a positive residue, or a value of –1, indicating a negative residue. It is also important to note that both phases, Φi and Φj, may need to be adjusted by a multiple of 2π to be consistent with the algorithm assumption of less than one half of a cycle phase change from one pixel to the other

(Buckley, 2000; and Rosen and Persaud, 2000). If unwrapping is done along a closed path containing only a single positive or negative residue, a +/- 2π phase discontinuity result. Whereas when integration is done along a path containing the same number of positive or negative residues, when closing the integration along this neutrally charged path, phase remains continuous.

The algorithm begins by searching the image for residues and once its found a search is initiated to find the closest adjacent residue. The residues are connected with a branch cut and the algorithm proceeds to increase the tree length until the tree is neutralized (Buckley, 2000). This procedure is repeated until all residues in the image are connected with a limit on the tree length so as to keep large trees from isolating sections of the phase field.

Next, the unwrapped phase is estimated by starting integration at a specific location, or so known as seed, and estimating phase for pixels adjacent to that seed, making sure that this pixel in neither crossing a branch or already have an estimated unwrapped phase.

Calculating the unwrapped phase involves adding or subtracting the needed integer number of cycles to each pixel to make the variation in phase of two adjacent pixels equal one half of a cycle.

This step is repeated to all pixels adjacent to that seed and thus making the unwrapping phase grow outward from the seed. Successful phase unwrapping will lead to determination of correct phase differences between neighboring pixels (Rosen et al., 2000).

6.10.1. Absolute phase determination

The last step in the phase unwrapping process involves determining the absolute phase, defined by Rosen and others (2000) as the phase due to range delay, from the unwrapped phase by determining an offset relating both phases to each other. The spectral absolute phase determination approach presented by Madsen and Zebker, 1992, implemented in ROI_PAC, splits the full range bandwidth in the processor into two sub-bands (lower and upper bands, with center frequencies f_{lower} and f_{upper}) with center frequency, f, and processes each individually. The two sub-bands are also divided with center frequencies, f_{lower} and f_{upper}, where two low-resolution interferograms are formed and used to generate a differential interferogram. Since the fringe frequency of the differential interferogram generated is sufficiently low, all measured, unwrapped, and absolute phases are considered almost the same making the unwrapping and absolute phase determination processes unnecessary. And thus, the differential phase scaled by the frequency ratio $\frac{f}{f_{upper} - f_{lower}}$ is equal to the full resolution interferometric phase (Madsen and Zebker, 1992). By forming the difference between the scaled differential interferogram and the unwrapped phase of the full resolution interferogram, and averaging to reduce noise, the remaining phase offset may be determined (Madsen and Zebker, 1992; and Madsen et al., 1993).

6.11. Deformation determination using Two-Pass technique (DEME)

The differential interferometric approach employed here is the two-pass plus DEM technique, where a Digital Elevation Model (DEM) from an external source is used to isolate and remove the topographic contribution from an interferogram leaving only phase due to deformation of interest. At this stage, the software uses the available DEM to import the elevations and synthesizes the phase due to topography by converting the double binary format DEM into phase representation compatible with RIO_PAC. For this purpose, a 7.5-minute quadrangle USGS DEM with 30-meter resolution could be obtained and used. Since the DEM has different alignment than that of the generated interferogram, the DEM has to be resampled and registered to it. DEM resampling involves mapping it to the appropriate radar geometry using the geometric simulation of the imaging process (Buckley, 2000; and Rosen and Persaud, 2000). And thus, the relation between the radar geometry and DEM may be expressed as follows (Buckley, 2000):

$$\hat{l}.\hat{V} = \sin\beta \tag{6.80}$$

Where

$$\hat{l} = \frac{\vec{P}(t) - \vec{P}_{DEM}}{\left|\vec{P}(t) - \vec{P}_{DEM}\right|} \tag{6.81}$$

And

$$\hat{V} = \frac{\vec{V}(t)}{\left|\vec{V}(t)\right|} \tag{6.82}$$

Where

$\vec{P}(t)$ = Satellite position vector

$\vec{V}(t)$ = Satellite velocity vector

$\vec{P}_{DEM}$ = Position vector to a given pixel in the DEM

β = Azimuth angle (assumed known from the processed Doppler centroid)

Time, t_{DEM}, at which the spacecraft position and velocity satisfies Eqn. (6.80), is determined for each and every pixel in the DEM. The corresponding output radar geometry pixel (x, y) can be written as follows (Buckley, 2000; and Rosen and Persaud, 2000):

$$x = \frac{\left|\vec{P}(t_{DEM}) - \vec{P}_{DEM}\right| - \rho_{ref}}{\Delta_r} + 1 \tag{6.83}$$

$$y = \frac{\left|\vec{V}(t_{DEM})\right| t_{DEM} - a_{ref}}{\Delta_a} + 1 \tag{6.84}$$

Where

x = Range pixel

y = Azimuth pixel

ρ_{ref} = Range to first pixel in the output simulation

a_{ref} = Azimuth location of the first azimuth line in the output simulation

Δ_r = Range sample spacing

And

Δ_a = Azimuth sample spacing

Each pixel in the output has two quantities associated with it:

1- DEM height, adjusted for any bias between the DEM datum and output simulation datum (NAD27 in our case).

2- Simulated radar intensity, which can be expressed as (Buckley, 2000):

$$I = \frac{\cos^2 \theta_i}{\sqrt{1-\cos^2 \theta_i}} \tag{6.85}$$

Where

$$\cos\theta_i = -l.n \tag{6.86}$$

θ_i = Incidence angle

And

n = Surface outward unit normal vector

In the next step, this output simulation is registered to the generated interferogram using a procedure identical to the registration process presented in section 6.4, where an amplitude correlation between the simulated radar intensity and the generated interferogram amplitude is used to obtain a set of registration offsets.

This new interferogram is then subtracted from the initial one to generate the differential phase image in a procedure almost similar to the interferogram flattening process explained in section 6.7. The difference here is that the look angle is determined to the topographic height, z, associated with each pixel instead of to the reference surface and thus, the look angle computation equation in step three (Table 6.3) should be replaced with (Buckley, 2000):

$$\cos\theta_{lref} = \frac{\rho_1^2 + (r+h)^2 - (r+z)^2}{2\rho_l(r+h)} \tag{6.87}$$

Where $l = 1, 2$

After unwrapping the differential phase and determining absolute differential interferometric phase, the final step involves calculating the amount of deformation in cm, which is related to the determined absolute interferometric phase as follows:

$$\Delta = \Phi_{absolute} * \frac{\lambda}{4\pi} \tag{6.88}$$

Where

Δ = Amount of deformation in cm

$\Phi_{absolute}$ = Absolute interferometric phase in radian

And

λ = Radar wavelength in cm.

It is important to note that deformation is in slant range, and thus a positive deformation indicates an increase in the line of sight, which leads to the conclusion that the area of interest is either subsiding or extending in a direction away from the

satellite. On the other hand, a negative deformation indicates a decrease in the line of sight leading to the conclusion that the area of interest is either uplifting or extending in a direction towards the satellite.

7. Applications of SAR interferometry for sinkhole subsidence detection in Nevada

7.1. Overview

The Gold Butte district in Clark County, located in the Southeast corner of Nevada as can be seen in Figure 7.1, is a unique geologic region in which collapse and subsidence sinkholes can be observed. This area, located east of the Overton arm of Lake Mead, was selected to study applications of SAR interferometry for sinkhole subsidence detection due to the existence of several sinkholes. Using satellite radar interferometry (InSAR), we will be able to monitor recent deformation across the study area and determine its rate. It is presumed that the largest sinkhole formed in the area, once called "Budd sinkhole" and now known as "Devils Throat sinkhole", created as a massive collapse of the earth in the early 1940's and has been for the past few years gradually increasing in size. Locals say that the sinkhole was around 23 meters (75 feet) across and 28 meters (90 feet) deep in 1978. However, recent collapses in the northwest portion of the sinkhole increased its dimensions to approximately 30 meters (100 feet) across and around 41 meters (135 feet) in depth, measured at the deepest edge.

This chapter focuses on InSAR observations, which are especially ideal in this region due to the predominantly arid weather conditions, regionally broad terrain, and most importantly low vegetation density, and thus increases the likelihood of producing coherent images.

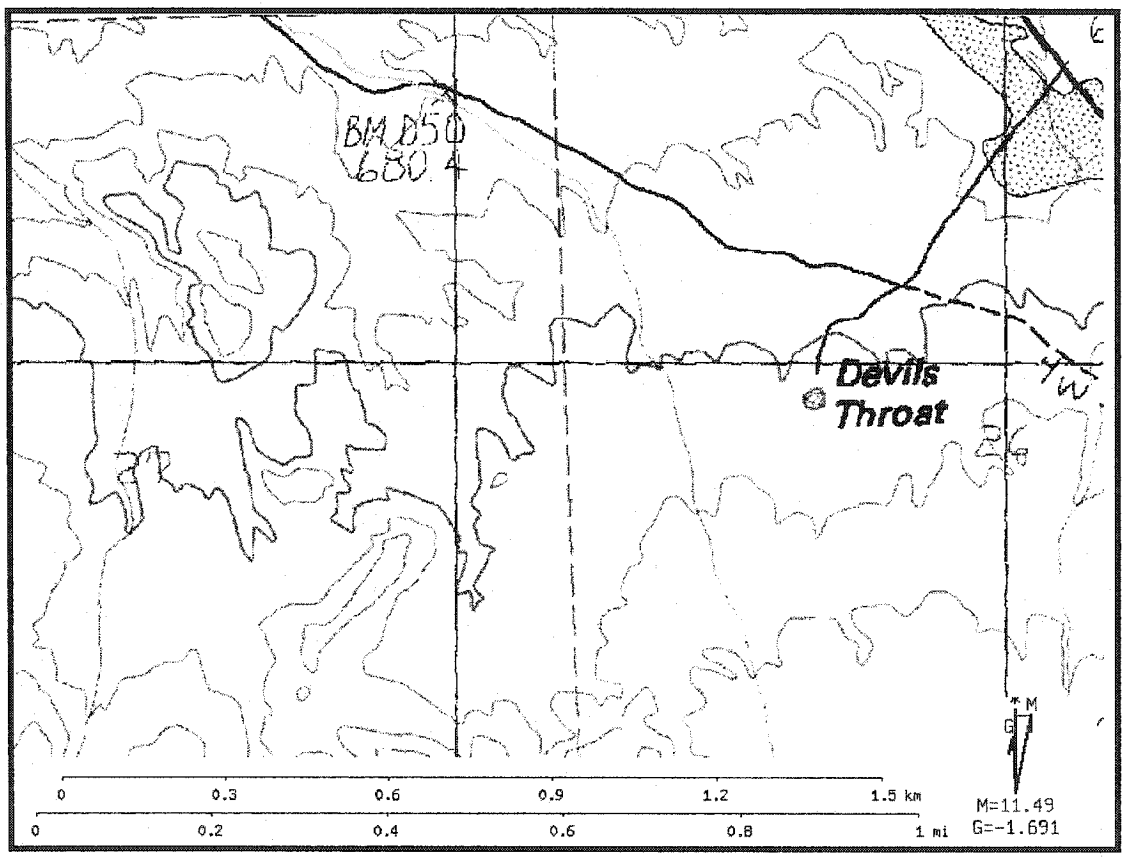

Figure 7.1: Topographic map of the Devil's Throat area in Clark County, Nevada (Source: After Topozone.com)

It is also important to mention that since this technique was proposed to measure very small (1 cm or less) surface motion with good resolution (10 meters) over large swaths (50 km) using SAR images (Gabriel and Goldstein, 1988; and Goldstein et al., 1989), it would be ideal to study the recent rate of deformation due to the existence of a sinkhole that meets the minimum technique resolution requirements.

In this study, Spaceborne Synthetic Aperture Radar (SAR) data of the Devil's Throat area, acquired by the European Space Agency (ESA) Satellites (ERS-1 and ERS-2), encompassing an almost five year observation period (1992-1997), will be used to study the deformation in the area.

After searching the European Space Agency archive, using the Display Earth remote sensing Swath Coverage for Windows (DESCW) catalogues, it was concluded that for this study area the largest number of ERS SAR archive scenes exists for Track 84, Frame 2871, descending track, which provides best coverage of the area of interest as can be seen in Figure 7.2. Each SAR scene covers a 100x100 Km^2 and is centered at latitude of 36° 27 and a longitude of -114° 18.

Three raw SAR scenes, from the above-mentioned descending track of the right-looking European Space Agency (ERS-1 and ERS-2) satellites, were obtained from Eurimage Inc.

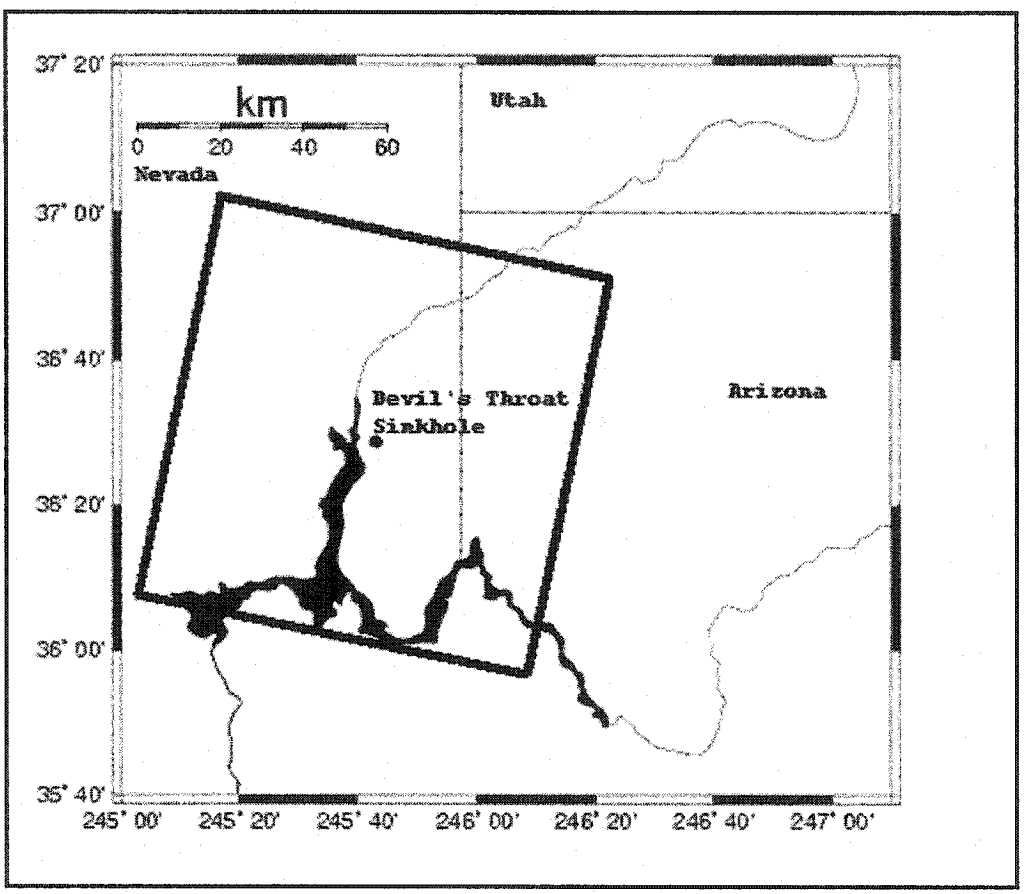

Figure 7.2: ERS orbit Track 84 Frame 2871 over the Gold Butte district in the Southeast corner of Nevada

Eurimage Inc., is an official ESA commercial distributor based in Italy, with a worldwide distribution license for both ERS-1 and ERS-2. The scenes were used to generate three differential interferograms spanning periods of 2 to almost 5 years.

7.2. Data selection criterion

A total of 43 available ERS SAR archive scenes of the chosen combination of track and frame number were located, sorted and listed in Tables A1 and A2 of appendix A. Using these SAR scenes, one can form 903 different interferometric pairs. However, other conditions must also be taken into consideration to determine the suitability of the formed pairs for interferometric processing.

Since the maximum allowable perpendicular baseline for a suitable interferometric pair is 150 meters (Massonet et al., 1995), the next step should involve eliminating pairs with perpendicular baseline larger than the maximum allowable limit.

Although the reviewed literature suggested perpendicular baseline (150-meter baseline) is acceptable, in this study the maximum allowable perpendicular baseline was set to 100 meters since using a smaller perpendicular baseline as apposed to large one results in a smaller topography signal in our interferogram (Zebker et al., 1999).

At this stage, all interferometric pairs formed with perpendicular baseline larger than 100 meters were eliminated resulting in 106 suitable interferometric processing pairs. All 106 ERS SAR pairs, with perpendicular baseline less than or equal to 100 meters, are listed in Tables A3 through A6 of appendix A.

Seasonal considerations were also taken into account resulting in the elimination of interferometric pairs spanning different seasons. This important step takes into consideration atmospheric changes between chosen pairs and thus reduces errors in the resultant interferogram. This step further reduced the number of suitable interferometric pairs to 57 as can be seen in Tables A7 and A8 of appendix A.

Since the dry season represents the best period for radar interferometry, as it represents the season with the least atmospheric changes and thus lead to less errors in our signal, the available 57 interferometric scenes were further reduced to 23 suitable pairs as can be seen in Table A9 of appendix A. These pairs if used would produce the best results with minimum atmospheric errors. Finally, due to limited research budget, the minimum number of scenes that can be used to generate the maximum number of interferograms had to be chosen. Three scenes out of the 24 available scenes satisfied this condition, as these three scenes were suitable to be used in generating three different interferograms due to the fact that the perpendicular baseline for all three pairs formed fell below 100 meters.

To summarize, the three InSAR pairs for this study area were chosen taking into account the maximum allowable perpendicular baseline (less than or equal to 100-meter), seasonal considerations, as well as available research budget.

Table 7.1 lists the chosen InSAR pairs used to generate the interferograms in this research. It can be noticed that the InSAR pair's perpendicular baselines were kept to a minimum in order to minimize the topography element error in our interferograms.

For more details on the degree to which the chosen baseline affects the topography element of an interferogram, one can refer to a Ph.D. dissertation titled "Radar interferometry measurement of land subsidence", written by Sean Buckley in 2000.

Pair	Track	Frame	1st Date	2nd Date	1st Orbit	2nd Orbit	Baseline (m)	Days*
ERS1-1	084	2871	95-04-15	92-08-20	19611	5740	28	968
ERS2-1	084	2871	97-05-25	95-04-15	10960	19611	53	771
ERS2-1	084	2871	97-05-25	92-08-20	10960	5740	81	1739

*Date: Year-Month-Day

Table 7.1: List of pairs made with three target scenes that have baseline less than 100 meters

7.3. Height of Ambiguity

Before starting the discussion on interferogram processing, it is important to describe the geometric configuration of a pair of SAR images and show how such configuration affects the resultant interferometric phase.

The relative geometric configuration of two SAR images can be described sufficiently using the interferometric baseline vector $\bar{b}$ (Figure 7.3), which represents the difference between the phase centers of two satellites at the time when the target is imaged (distance between the two satellite locations) in three different representations (Buckley, 2000, and Hanssen, 2001):

1- Parallel/perpendicular representation

2- Horizontal/vertical representation

3- Baseline length and angle representation

Out of these three representations, the parallel/perpendicular, as can be seen in Figure 7.4, is often used due to its ability to describe the system's sensitivity to topographic heights and amount of geometric decorrelation.

The parallel baseline, B_{II}, can be defined as the satellite basic path length difference and is expressed as:

$$B_{II} = \rho_1 - \rho_2 \qquad (7.2)$$

ρ_1 = Range of the master scene

ρ_2 = Range of the slave scene

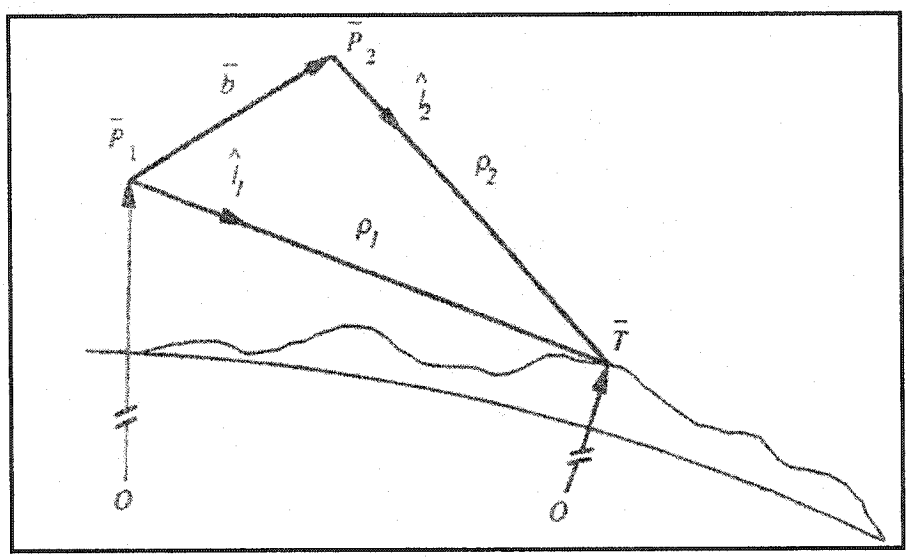

Figure 7.3: Interferometric baseline geometry
(Source: After Buckley, 2000)

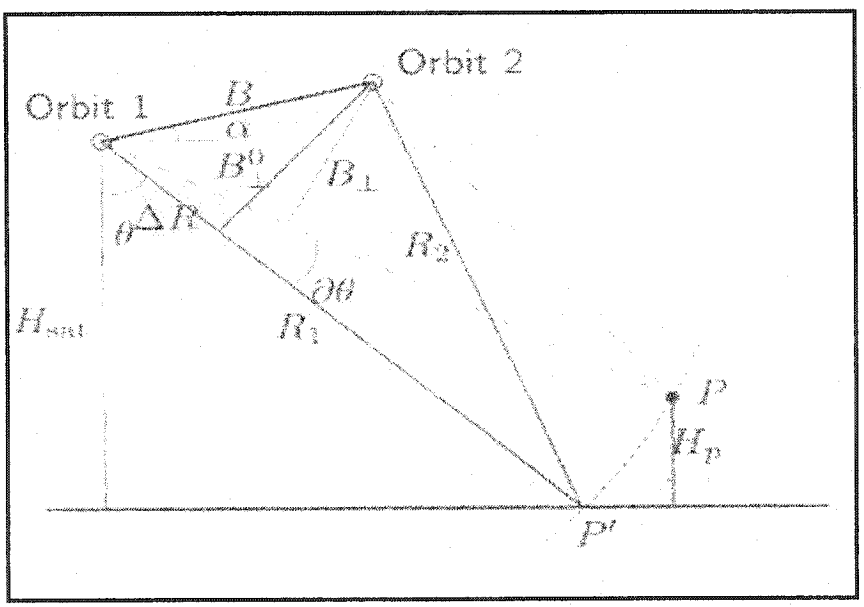

Figure 7.4: Geometry of parallel/ perpendicular baselines
(Source: After Mohr and Madsen, 1995)

On the other hand, the perpendicular baseline, $B_{\perp}$, which is defined as the component of the antenna baseline perpendicular to the range direction, is expressed as follows:

$$B_{\perp} = B\cos(\theta - \alpha) \tag{7.3}$$

Where

θ = Look angle (for ERS is 23°)

This baseline is used as a scaling factor to determine the height of ambiguity, h_a, which is defined as the amount of change in height required to create a 2π phase change (unwanted noise) in our interferogram and is expressed as follows:

$$h_a = \frac{\lambda \rho \sin\theta}{2B_{\perp}} \tag{7.4}$$

Where

λ = Radar wavelength (for ERS C band is 5.6565 cm)

ρ = Platform altitude (for ERS roughly 785 Km)

θ = Radar look angle (for ERS is 23°)

Height of ambiguity is used to describe the affects of the satellite orbital separation on the interferometric phase. In general, a large perpendicular baseline usually implies baseline decorrelation leading to a decrease in the signal to noise ratio in the interferogram and thus increase sensitivity to topography.

In other words, as the perpendicular baseline increases, sensitivity to phase error decreases. Using SAR pairs with a small enough perpendicular baseline generally lead to more accurate results.

7.4. Identification of atmospheric signal using pair-wise logic

Two pass interferometric processing is used in this study and thus topography is removed using a 7.5-minute quadrangle USGS Digital Elevation Model (DEM), as was mentioned earlier in this chapter, and thus the remaining signal consists of both deformation, which occurred during the study period, as well as some noise. Noise error in our signal consists usually of topographic residuals and/or atmospheric disturbance.

Different studies have shown that temporal as well as spatial atmospheric variations could account for a significant percentage in an interferometric phase change and could explain between 0.3-2.3 phase cycles of deformation (Hanssen, 2001). The driving mechanisms of this phenomenon as stated by Hanssen, are localized changes in refractive index due in large part to varying humidity in the troposphere, the lowest layer of the atmosphere (<15 Km).

Atmospheric noise in an interferogram is somehow difficult to determine and identify. However, the analysis of multiple interferograms over a varying time scales could be used to resolve changes in the signal path length and thus help in identifying the magnitude of atmospheric errors.

When analyzing several interferograms of an area where deformation is assumed fairly constant, atmosphere could be the primary reason for the variations in the interferometric signal. In this research, a technique known as linear combinations or pair-wise logic (Massonnet and Feigl, 1995, and Hanssen, 2001) is used to help in resolving the location of some localized atmospheric signal and determining the amount of noise due to atmosphere present. This technique involves creating three interferograms from three SAR images, which can be accomplished by generating two of these three interferograms using a common image between them. This technique helps in identifying atmospheric errors by simply reasoning between what we expect to see in our interferograms with what we actually observe.

In this study, three interferograms will be generated:

1- A = April 15, 1995 – August 20, 1992

2- B= May 25, 1997 – April 15, 1995

3- C = May 25, 1997 – August 20, 1992

When no atmospheric noise is present, the deformation from A (950415-920820) and B (970525-950415) should add up to equal what is observed in image C (970525-920820). Although this is true, a set of several interferograms should be analyzed and compared to prove and be certain that no atmospheric errors are present.

Profiles across all three generated interferograms will be constructed, analyzed, and discussed in the following sections.

The analysis of these profiles will help in identifying and maybe determining the amount of noise due to atmosphere in our interferograms.

7.5. Interferogram processing steps, results and analysis

This section explains in detail all the steps involved in the process of generating an interferogram, followed by an illustration of the generated results and finally the results analysis.

7.5.1. Interferogram processing steps

For each interferogram, the raw SAR format data of the two scenes were first converted to ground-range Single Look Complex image (SLC) using ROI_PAC, a SAR processing and Interferometry software developed at JPL/Caltech. This step produces a 100X100 Km scene with pixel dimensions of 7.9 meters in range and 4 meters in azimuth, as can be seen in Figures 7.5- 7.7. Since a SAR satellite records about 1000 responses for each object creating a lot of noise, dividing the dataset into 16 increments of about 63 responses each and processing each data subset to form an image reduce this noise. The 16 resulting images are then combined to create the final image product, called a 16-look image. The 16-look images are used to illustrate the generated SLC SAR images in the following Figures, as they are smaller in size and easier to view. Nominal orbit state vectors of each scene header are enhanced, during image formation, using accurate satellite orbit information from the German Processing and Archiving Facility (ESA/DLR) known as the precise state vector (PRC) data.

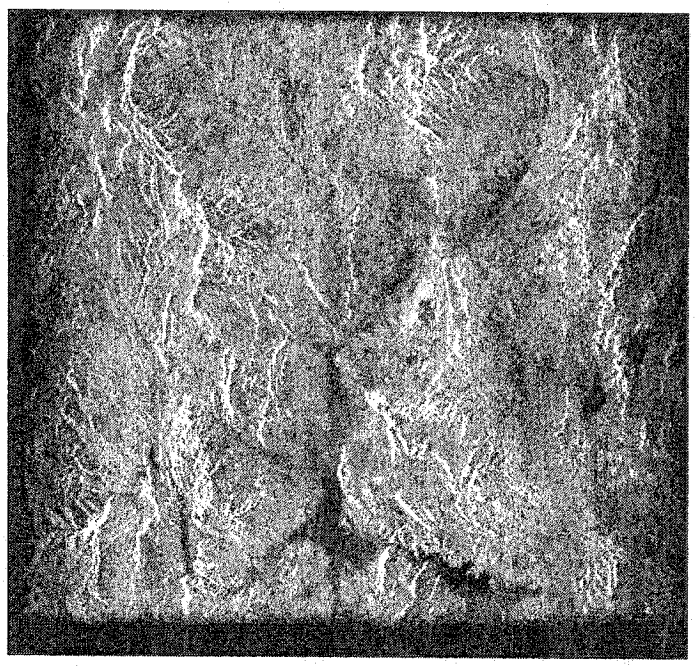

Figure 7.5: August 20th, 1992 Single Look Complex SAR image

Figure 7.6: April 15th, 1995 Single Look Complex SAR image

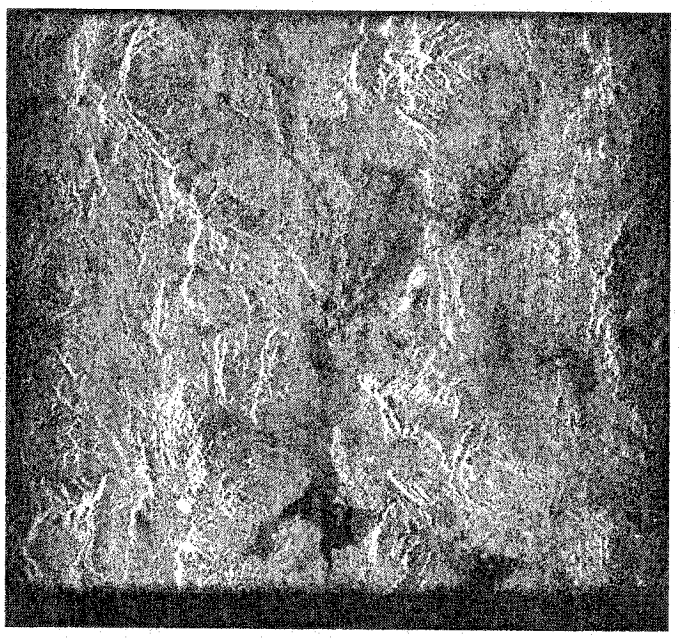

Figure 7.7: May 25th, 1997 Single Look Complex SAR image

After the image formation, the master and slave images of each pair are registered, where a set of range and azimuth offset measurements are determined and used to estimate a functional mapping to resample the slave image to the master image. A correlation image between the master and slave images of each pair is then generated giving good correlation (correlation = 1) is some areas and bad correlation (correlations = 0) in others. Bad correlation can be noticed in areas were rapid changes happening such as areas where rivers exist as an example.

Correlation images of the three interferograms are shown in Figures 7.8-7.10. It should be noted that the correlation images are flipped over, where east and west directions are reversed, which is considered a normal processing step using ROI_PAC.

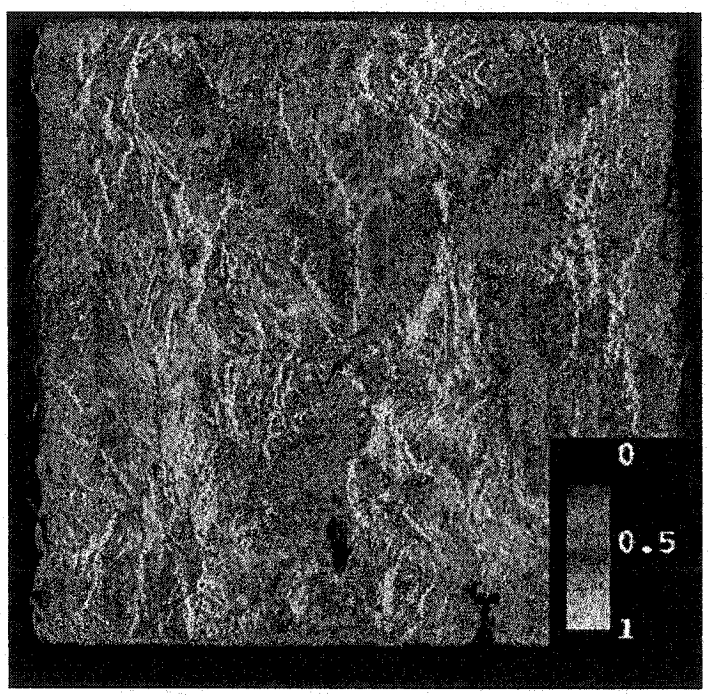

Figure 7.8: 95-92 correlation image

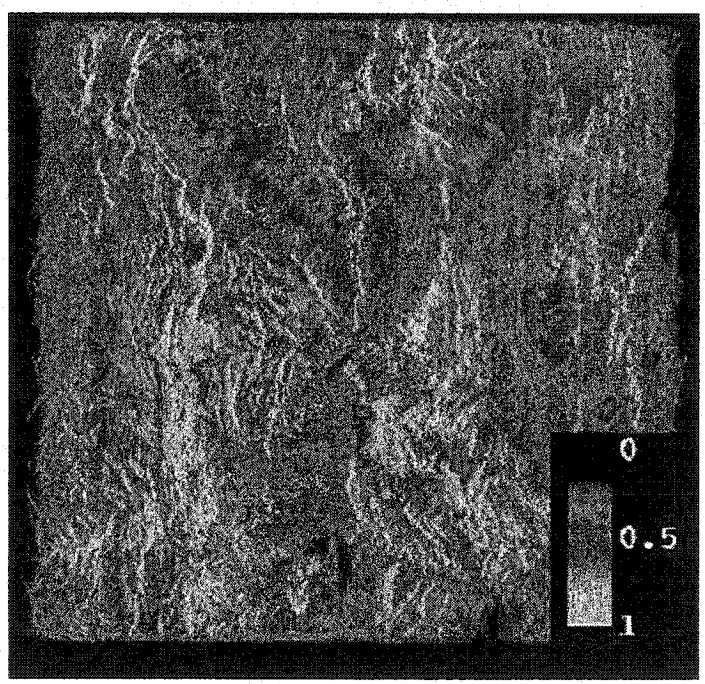

Figure 7.9: 97-95 correlation image

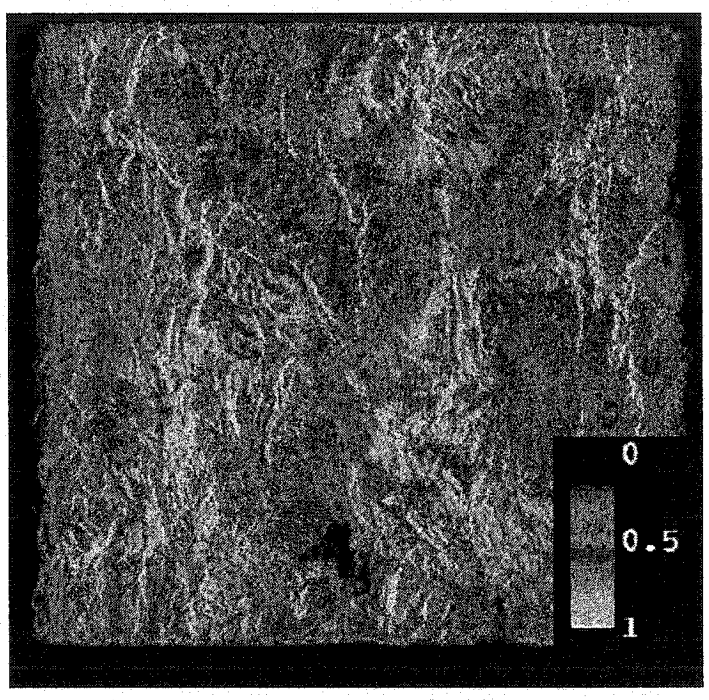

Figure 7.10: 97-92 correlation image

The differential interferometric approach employed here, as was mentioned earlier, is the two-pass plus DEM technique, where isolating and removing the topographic contribution from an interferogram, using a DEM, determines deformation. At this stage the software uses the available DEM to import the elevations and synthesizes the phase due to topography by converting the double binary format DEM into phase representation compatible with ROI_PAC (Figure 7.11). For this purpose, a 7.5-minute quadrangle DEM with 30-meter resolution was obtained from the U.S. Geological Survey (USGS).

Since each USGS DEM quadrangle covers and area of approximately 12 x 14 Km, which is considered not sufficient for our area of interest, a total of 34 adjacent quadrangles were mosaic resulting in a DEM covering a larger area. The resultant DEM covered the whole 59 x 99 Km study area. This DEM is then converted to double binary format compatible with ROI_PAC and used to generate a simulated topography phase interferogram. This new interferogram is then subtracted from the initial one to generate the differential phase image.

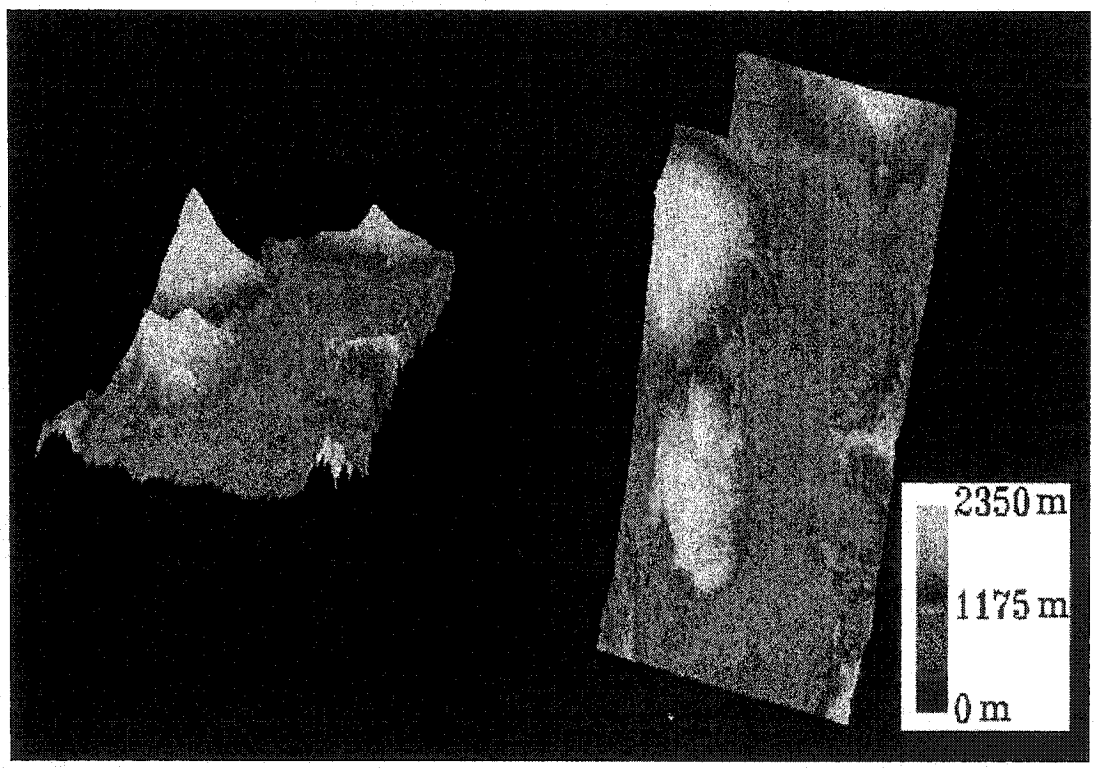

Figure 7.11: Simulated DEM used to remove topography

The measured interferogram phase is then unwrapped to determine the absolute interferometric phase, also referred to as the slant range direction phase. The absolute phase, which represents the path length difference in the radar's line of sight, is directly related to and can be used to determine the height of topography in the area imaged as well as the amount of deformation. The final differential unwrapped interferograms will be illustrated later in this section and analyzed in an upcoming section.

Horizontal as well as vertical profiles across the area of interest in all three generated interferograms are then constructed to give insight into the spatial distribution of deformation within the Devil's Throat area. These profiles and their analysis will be discussed later in this chapter.

7.5.2. Interferogram processing results

The first interferogram, as was shown in Table 7.1, is the result of a change in slant range phase that spans between the two images (April 15, 1995 and August 20, 1992) and thus illustrates the deformation over a period of 968 days (2 years, 7 months and 26 days).

The second interferogram, as was also shown in Table 7.1, is the result of a temporal shift in slant range phase that spans between the two images (May 25, 1997 and April 15, 1995). This interferogram illustrates the deformation over a period of 771 days (2 years, 1 month and 10 days).

The third and final interferogram is the result of a temporal shift in slant range phase that spans between the two images (August 20, 1992 and May 25, 1997) and thus illustrates the deformation over a period of 1739 days (4 years, 9 months and 5 days). The InSAR data used in generating all three interferogram collected from both ERS-1 and ERS-2 (European Remote Sensing satellite platform) descending orbit (track 084, frames 2871) are listed in Table 7.1.

The final unwrapped differential interferograms with color ramps representing the absolute interferometric phase rate are illustrated in Figures 7.12-7.14. A three dimensional surface of each interferogram is illustrated in Figures 7.15-7.17. The profiles (black line) shown on the Figures were constructed and used to generate a cross-sectional view illustrating the relative slant range deformation at a given location along each profile. Such profiles help in giving insight into the spatial distribution of deformation within the studied area (Figures 7.18-7.20). Deformation along each constructed profile is relative to the eastern most point of the profile, which was assumed to be stable (deformation = 0 meters) during the study period. It is also important to mention that deformation values along each profile is multiplied by –1 in order to illustrate the deformation for periods over an increasing time period; 1992-1995, 1995-1997, and 1992-1997 instead over a decreasing time period; 1995-1992, 1997-1995, and 1997-1992, the way the data was processed in our case.

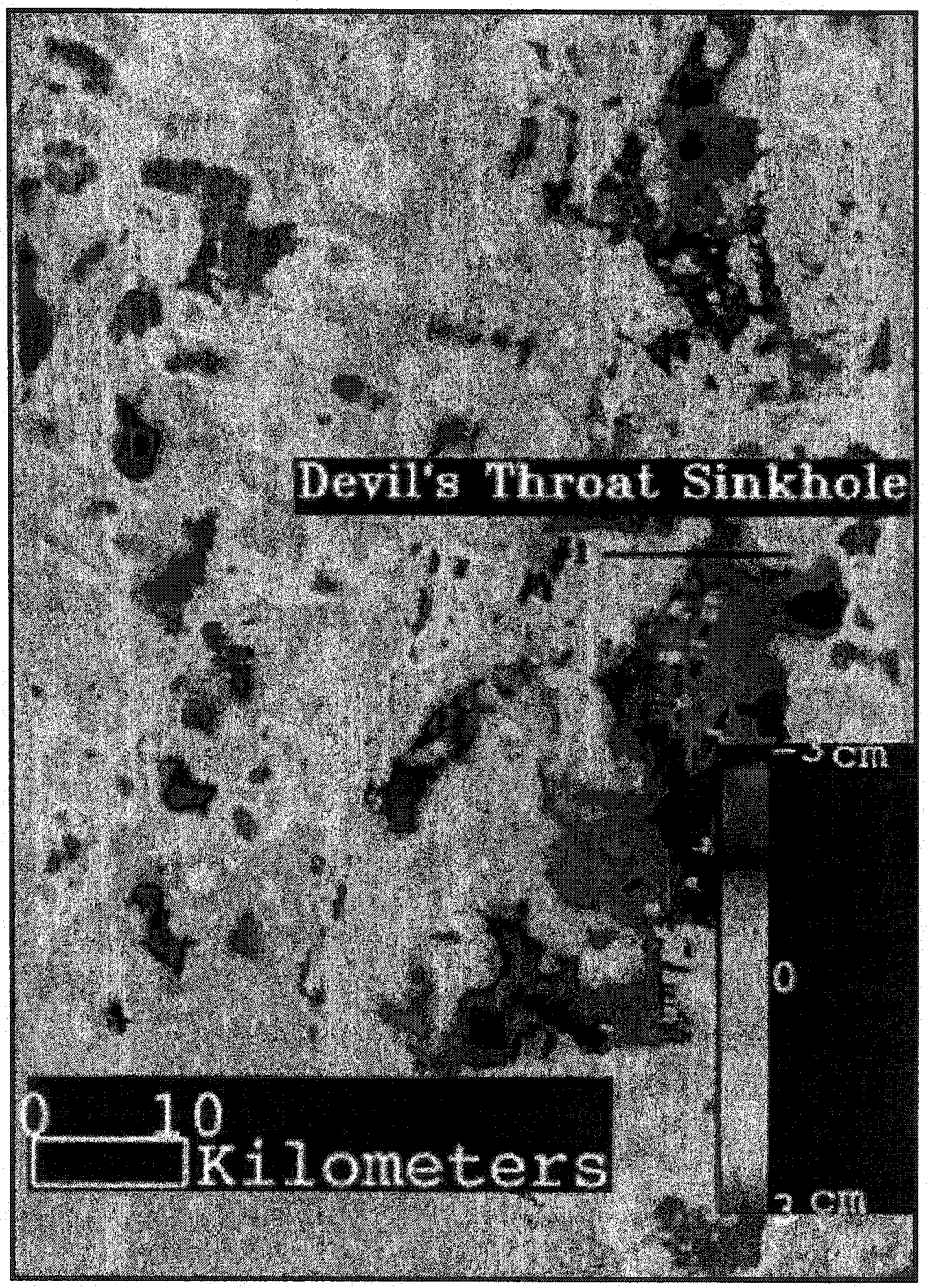

Figure 7.12: 1995-1992 Differential unwrapped interferogram

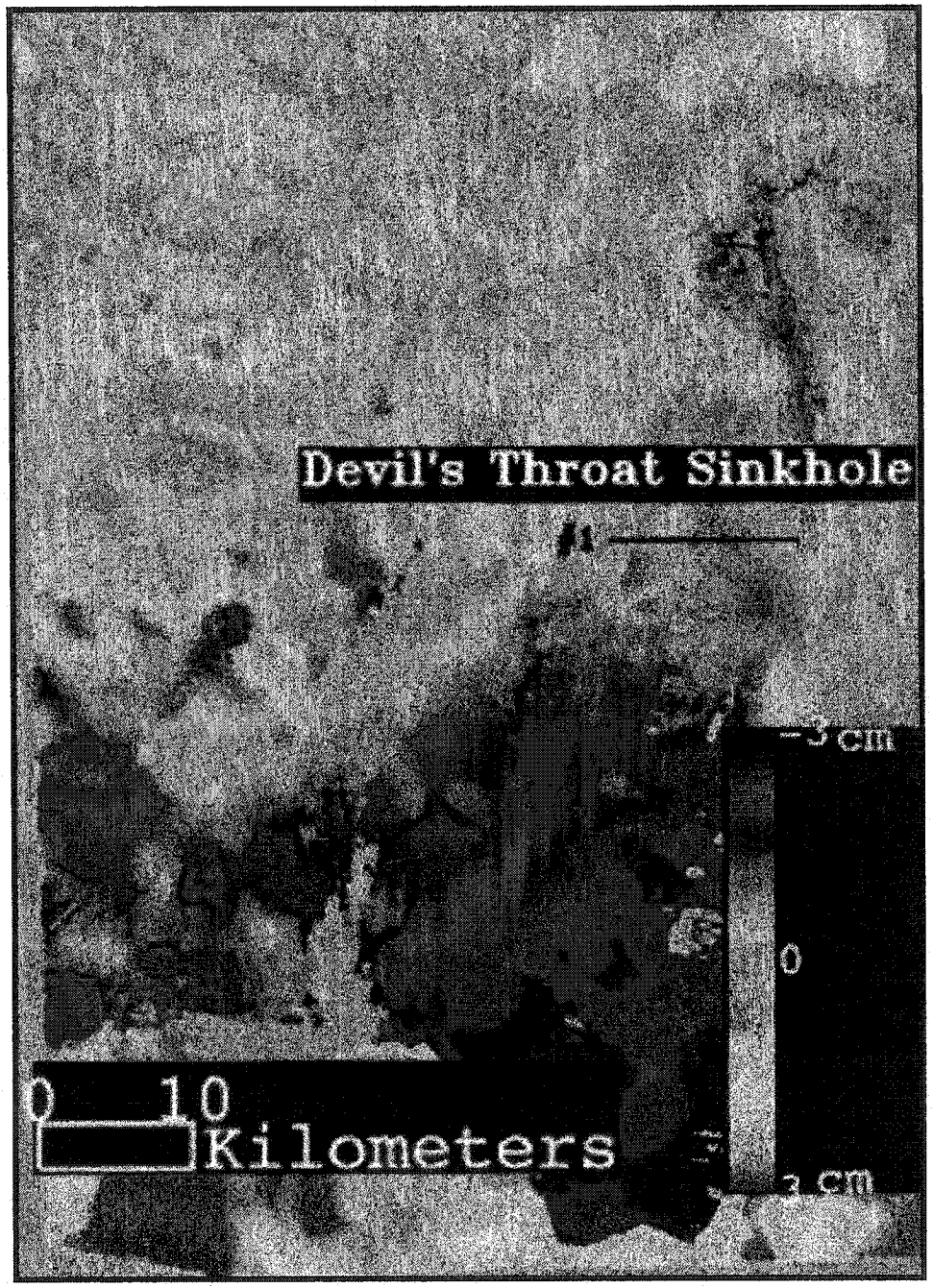

Figure 7.13: 1997-1995 Differential unwrapped interferogram

Figure 7.14: 1997-1992 Differential unwrapped interferogram

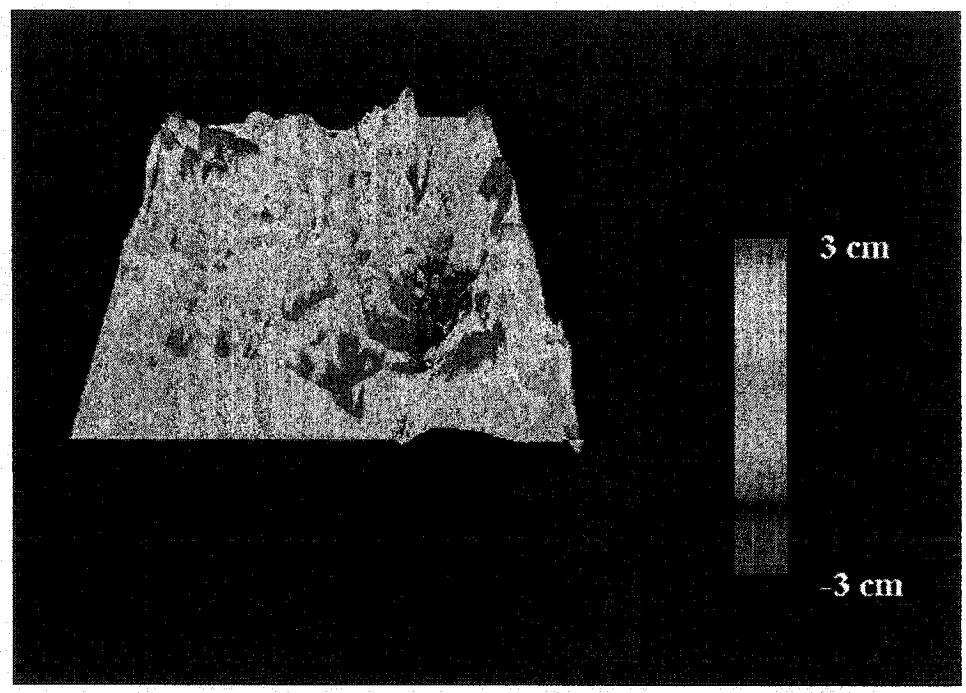

Figure 7.15: 3-D surface of the 1995-1992 Differential interferogram

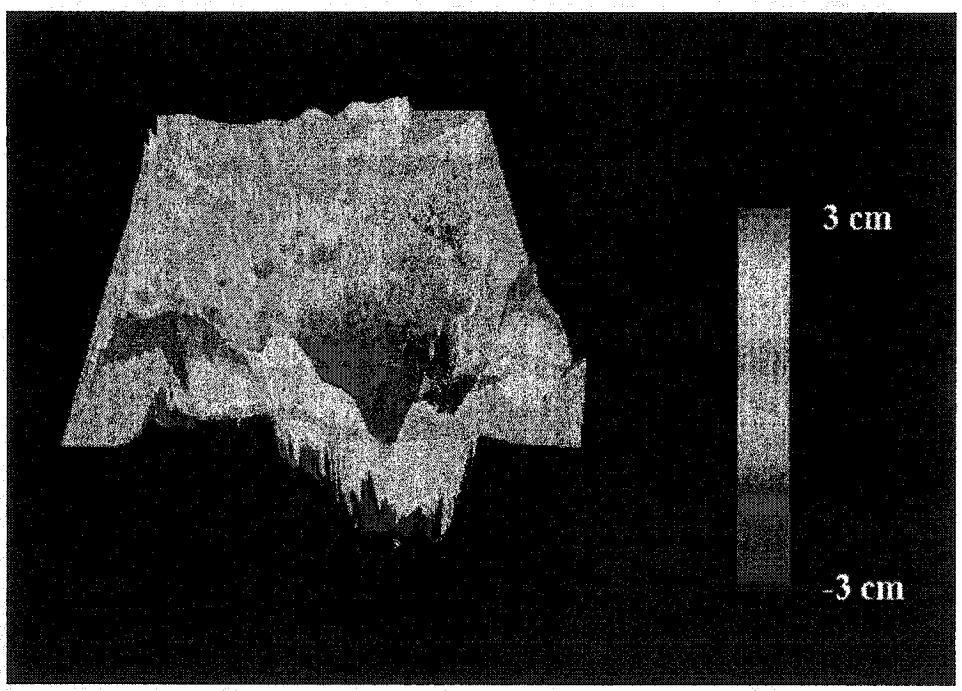

Figure 7.16: 3-D surface of the 1997-1995 Differential interferogram

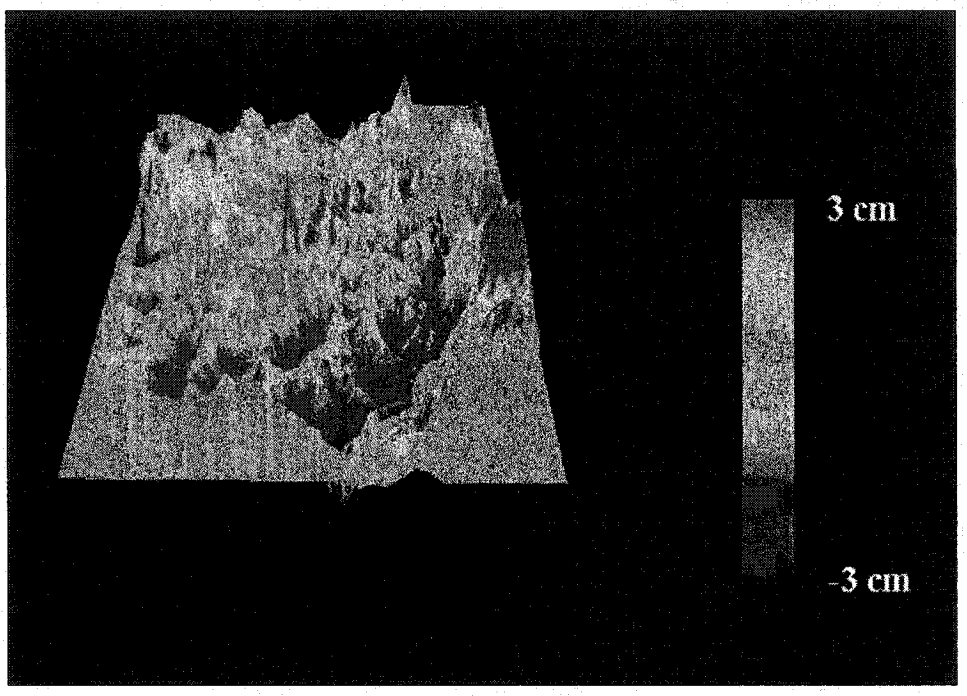

Figure 7.17: 3-D surface of the 1997-1992 Differential interferogram

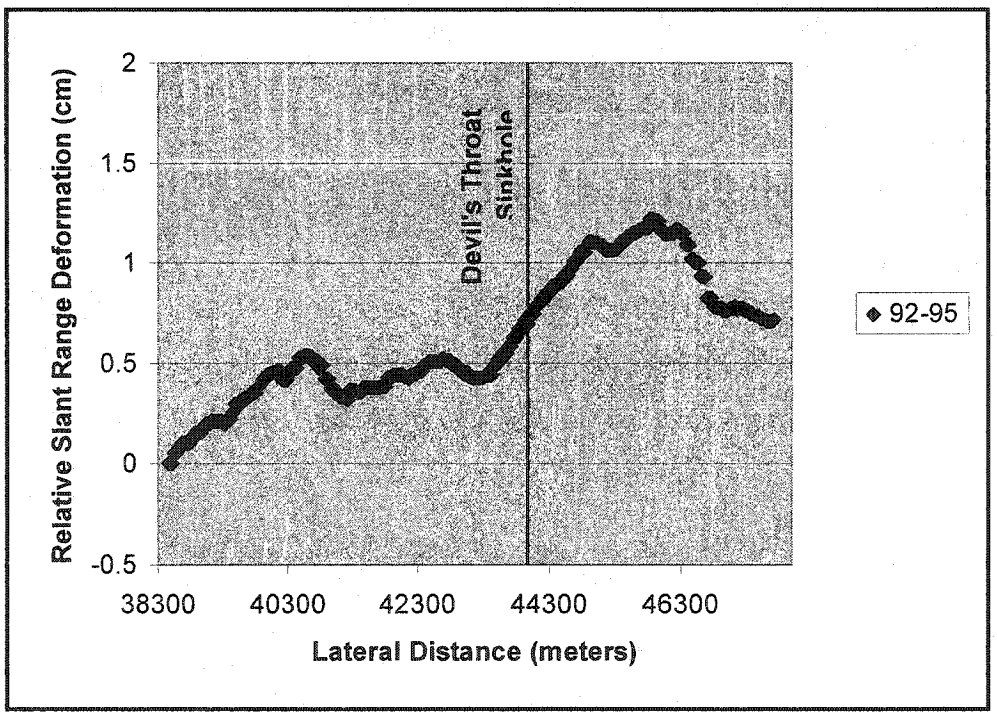

Figure 7.18: 1992-1995 Relative slant range deformation across a horizontal profile

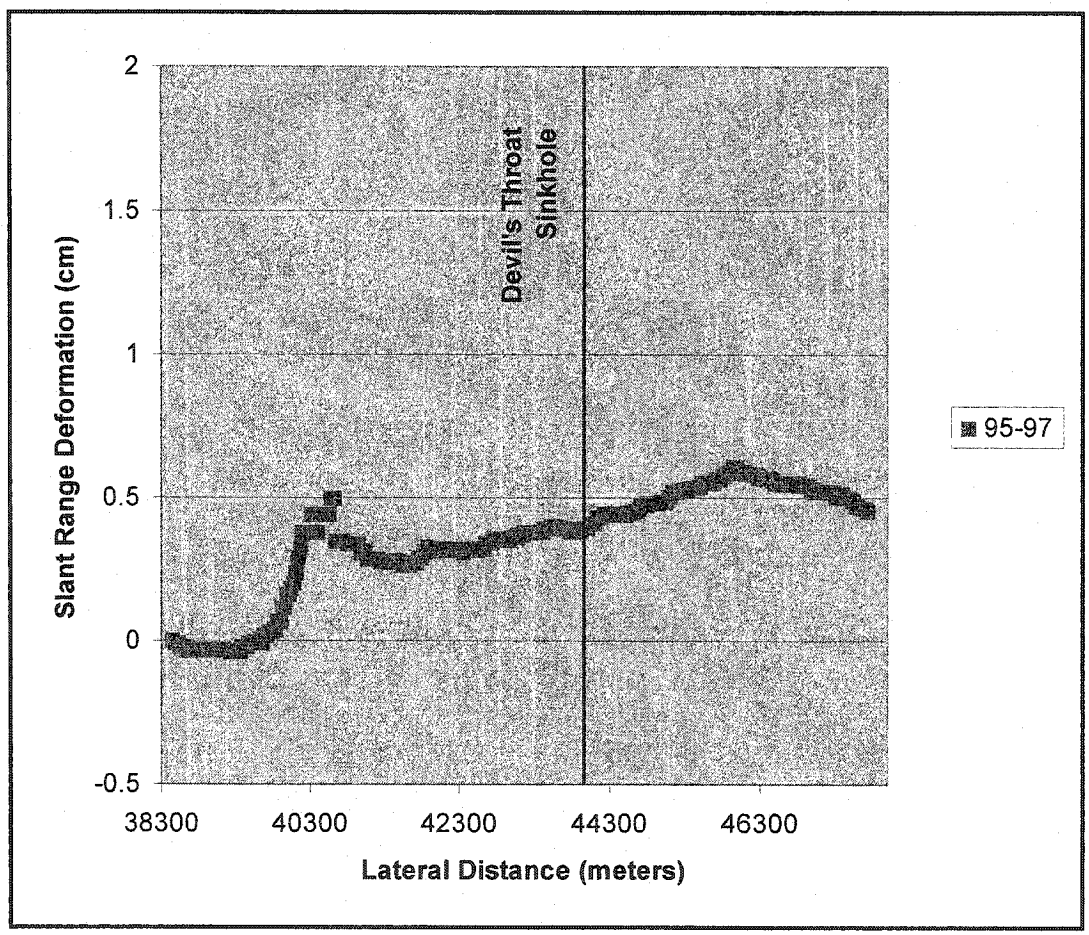

Figure 7.19: 1995-1997 Relative slant range deformation across a horizontal profile

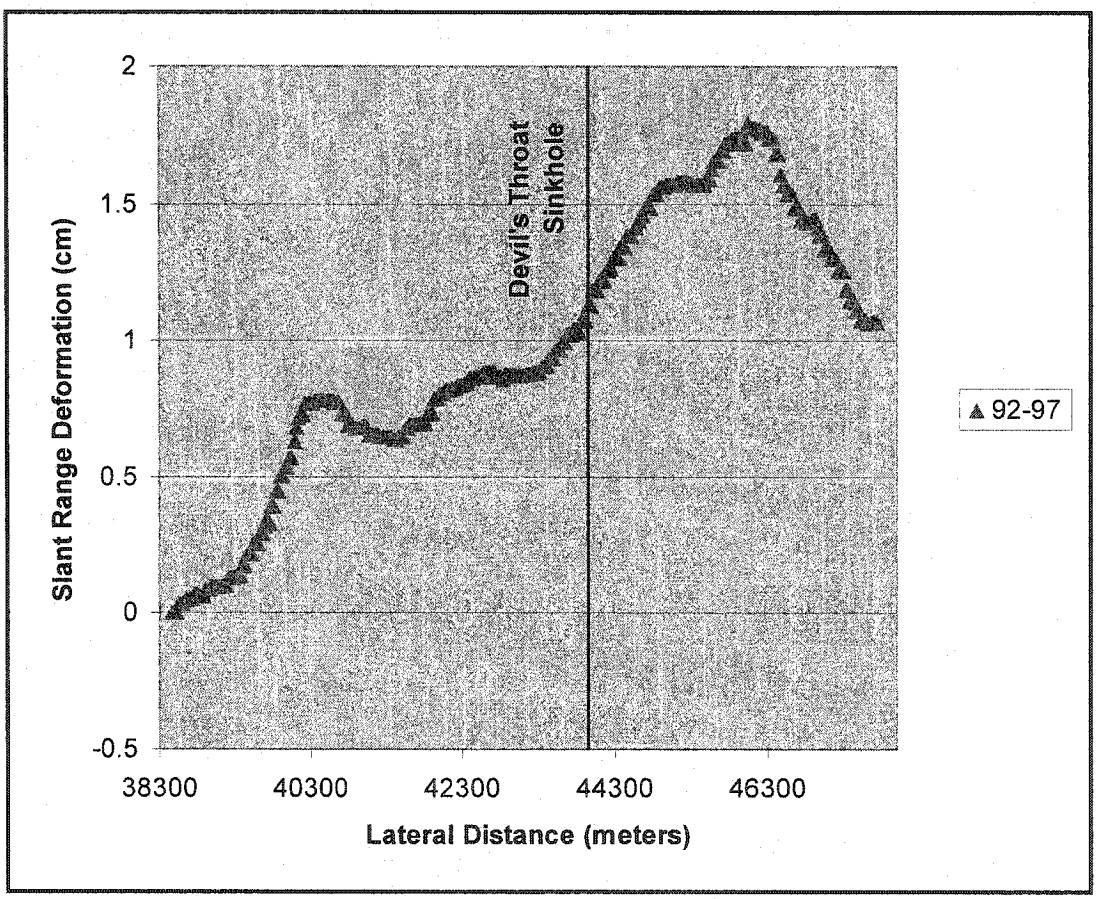

Figure 7.20: 1992-1997 Relative slant range deformation across a horizontal profile

This means that a motion that results in a positive signal over an increasing time period represents motion of the ground away from the satellite indicating a westward extension and/or subsidence. All three profiles will be analyzed and discussed in the following section. The three profiles will also be compared with each other to help in identifying atmospheric noise in the generated interferograms.

7.5.3. Interferogram analysis

Prior to this study, the Gold Butte area deformation rates were unknown. Analyzing the interferograms generated using Synthetic Aperture Radar (SAR) data collected by ESA ERS-1 and ERS-2 satellites, encompassing an almost five year period of observation (1992-1997) will aid in monitoring recent deformations and thus determine deformation rates in the area. Three successful interferograms were generated for a descending orbital trajectory, as was shown earlier, and will be used to yield deformation information.

At this stage, deformation in centimeters at any location on the generated interferogram can be determined in terms of the resulting absolute interferometric phase as follows:

$$\Delta = \Phi_{absolute} * \frac{\lambda}{4\pi} \qquad (7.4)$$

Where, Δ is the amount of deformation in cm, $\Phi_{absolute}$ is the absolute interferometric phase in radians, λ is the radar wavelength in cm.

Since this interferogram was generated using a descending orbit data and was processed in a descending time period order (e.g. 1997-1992), increase in range change shows that the area of interest is either subsiding or extending away from the satellite.

From the absolute interferometric phase cycle of interferogram A (1995-1992), it can be estimated that the maximum downward movement along the constructed profile over that period (almost 2.65 years) was approximately 1.209 cm. This means that the maximum deformation rate for that period of time was approximately 0.456 cm/year. Whereas for the 2.11-year period interferogram B (1997-1995), the maximum deformation along the constructed profile was estimated to be 0.607 cm, indicating that the maximum deformation rate for this period (1997-1995) was around 0.288 cm/year. On the other hand, the deformation rate for interferogram C (1997-1995) was estimated to be 0.376 cm/year, as the maximum subsidence along the profile constructed during that 4.76-year period was about 1.792 cm (Table 7.2). It is important to mention that, by using SAR interferometry, it is not always possible to determine a realistic and absolute deformation field, as deformation at any location is relative to the point where phase unwrapping starts. However, deformation values when determined relatively from one location to another will not change. In our case, ROI_PAC starts unwrapping at pixel location (-9999, -9999), at the lower right hand corner of the image where deformation is assumed to be zero, and thus deformation at all other locations are given relative to that point.

Study Period	Maximum Deformation (cm)	Deformation Rate (cm/year)
1995-1992	1.209	0.456
1997-1995	0.607	0.288
1997-1992	1.792	0.376

Table 7.2: Deformation and deformation rates along horizontal profiles

Height of ambiguity, which is defined as the amount of change in height required to create a 2π-phase change (unwanted noise) in our interferogram is calculated for each interferogram and are listed in Table 7.3. The values given in the table describe the affects of the satellite orbital separation on the interferometric phase and show the distance in meters that create a 2π-phase change of unwanted noise in each interferogram. From the table, one can notice that an increase in the perpendicular baseline used lead to a decrease in height of ambiguity, meaning that our resulting signal includes more topographic related errors. A mean altitude of 785 kilometers was used to calculate the height of ambiguity in each case. The three constructed profiles passing by our area of interest, stretches between horizontal pixels number 1282 and 1591 (9270 meter long horizontal profiles).

Time Period	B⊥	h_a (meters)
1995-1992	28	309.8
1997-1995	53	163.6
1997-1992	81	107

Table 7.3: Height of ambiguity

Deformations along these three interferogram show that the Devil's Throat sinkhole area lay very close to the location where maximum deformation rate occurred (sinkhole located at pixel number 1465 on the constructed profile).

The results also show that the generated deformation rates from interferogram C (1997-1992) agrees very well with the deformation rates generated by adding deformation from both interferograms A (1995-1992) and B (1997-1995) (Figure 7.21). Table 7.4 shows a comparison of expected vs. actual deformation rates. A compression of relative slant range deformations a long a vertical profile crossing the Devil's Throat area was also conducted and is illustrated in Figure 7.22. On this vertical profile the Devil's Throat sinkhole is located at pixel number 1656 (Lateral distance = 49680 meters).

Weather that was present before and on the day of data acquisition was also looked into in order to help in deciding whether atmospheric errors were introduced. Data from the NOAA weather database showed that all three days were dry (precipitation = 0 inches) thus minimizing the chance that atmospheric errors were introduced.

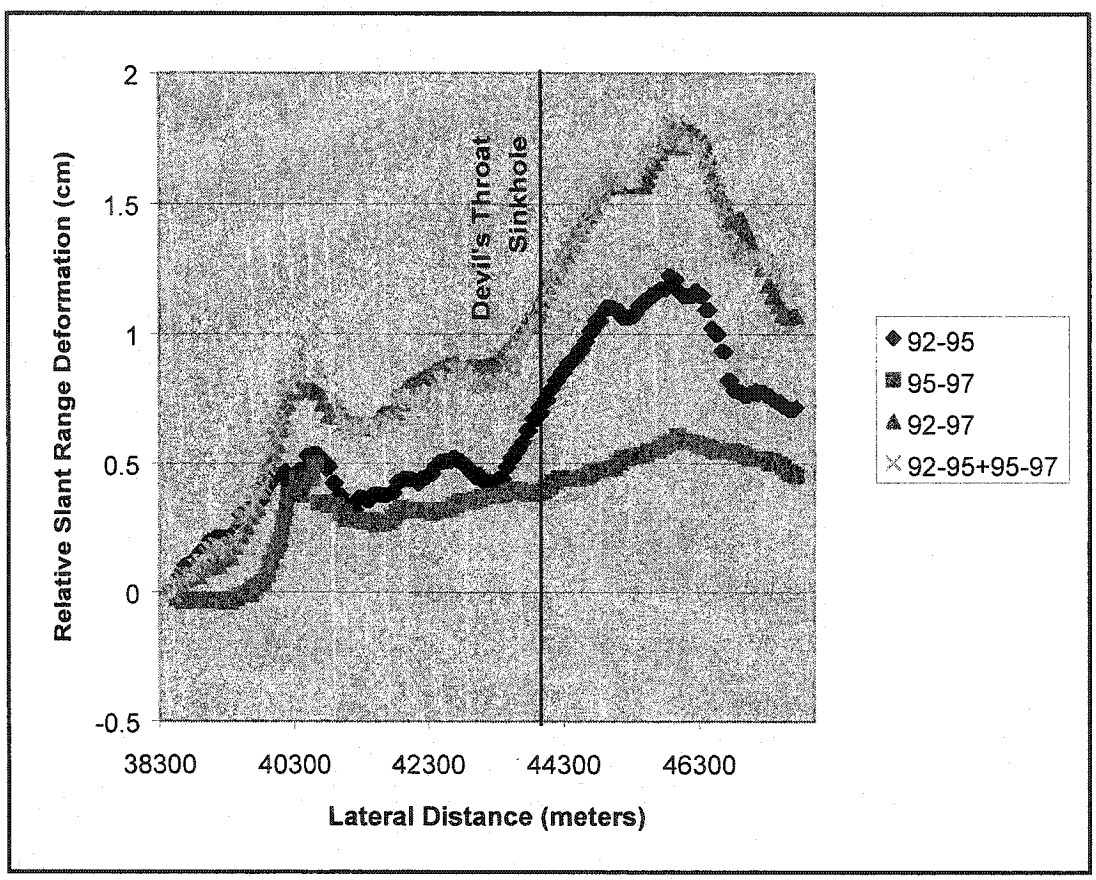

Figure 7.21: Relative slant range deformations across a horizontal profile

Time Period	Expected Deformation (A+B) (cm)	Actual Deformation (C) (cm)	Expected Deformation Rate (A+B) (cm/year)	Actual Deformation Rate (C) (cm/year)
1997-1992	1.816	1.792	0.381	0.376

Table 7.4: Deformation and deformation rates, Expected versus actual

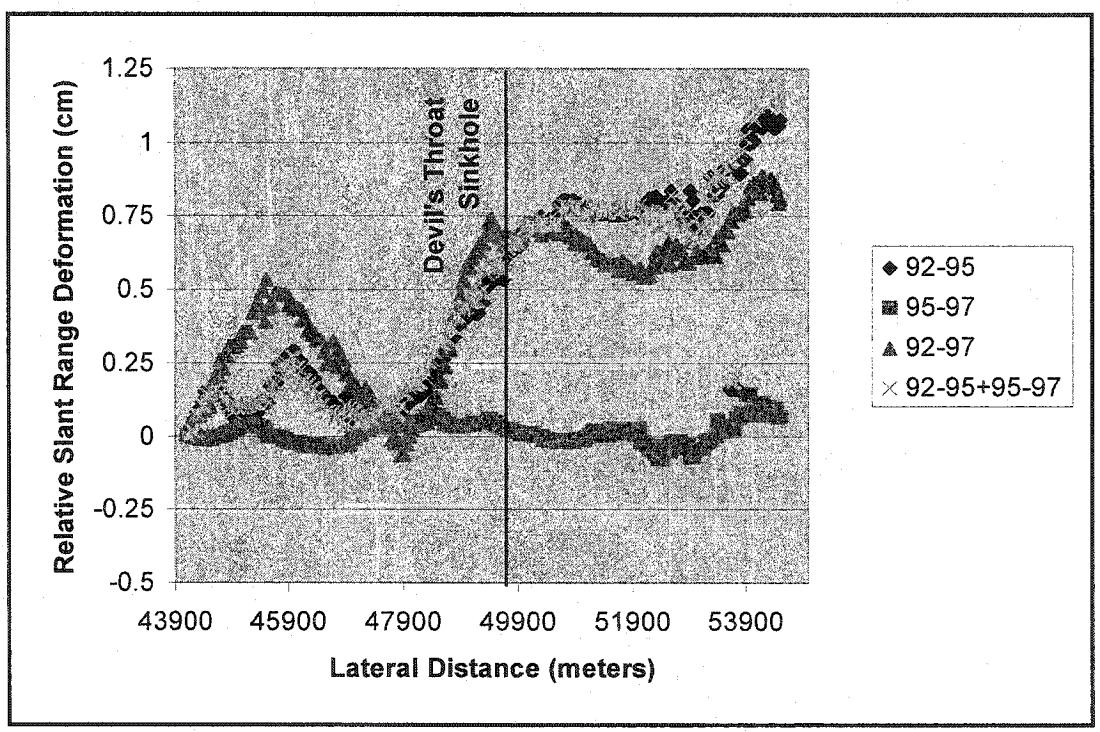

Figure 7.22: Relative slant range deformations across a vertical profile

At this stage, the principles of finite differences (Bardet, 1997) was used to generated shear strain (%) across the generated horizontal as well as vertical profiles (Figure 7.23-7.28). From these Figures, one can clearly notice that in most cases the Devil's Throat sinkhole fell either on or very close to the maximum shear strain present in the area, which agrees very well with what was expected.

By studying the geological settings of the study area, it was determined that this type of movement agrees very well with the expected ground surface movements. The geological settings of the area are not discussed here as they are out of the scope of this research.

7.6. Decomposition of the displacement vector

As was mentioned earlier in section 3 of this chapter, the radar signal that we observe in the differential interferogram represents the difference in path lengths along the radar's line of sight (slant range direction) and thus the deformation values are given in terms of change in slant range. To further analyze the resulting deformation and determine the three dimensional displacement vector, $\vec{d}$, one should refer to the equation outlined by Hanssen (2001):

$$d_r = d_u \cos(\theta_{inc}) - \sin(\theta_{inc}) \left[d_n \cos\left(\alpha_h - \frac{3\pi}{2} \right) + d_e \sin\left(\alpha_h - \frac{3\pi}{2} \right) \right] \qquad (7.5)$$

Where θ_{inc} = Angle of incidence (ERS $\theta_{inc} \approx 23°$), d_n = Deformation in the North direction, d_e = Deformation in the East direction, and d_u = Deformation in the UP direction.

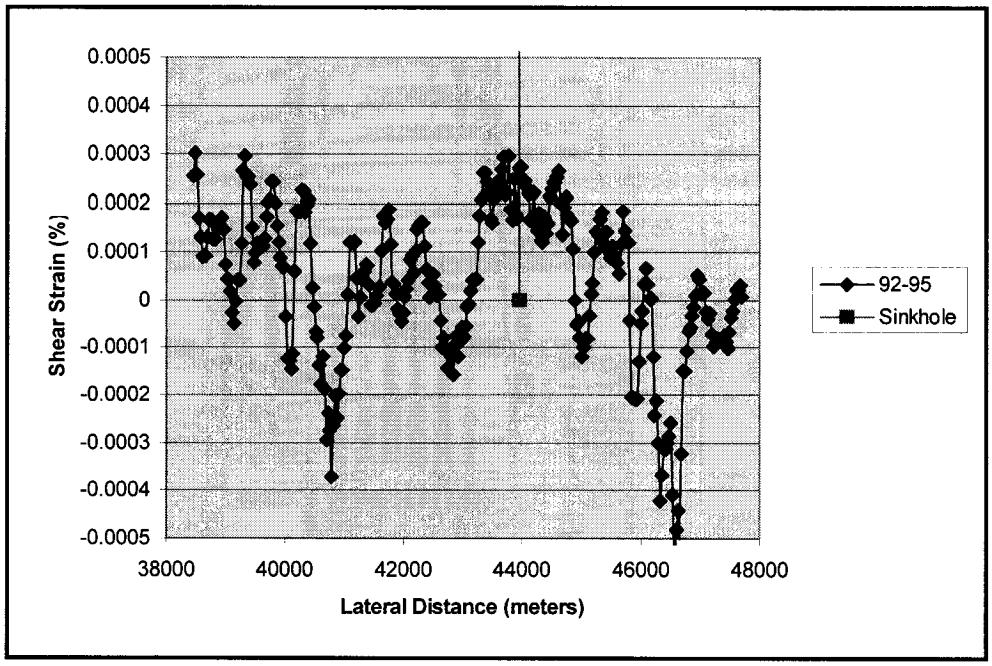

Figure 7.23: 1992-1995 Shear strains across the horizontal profile

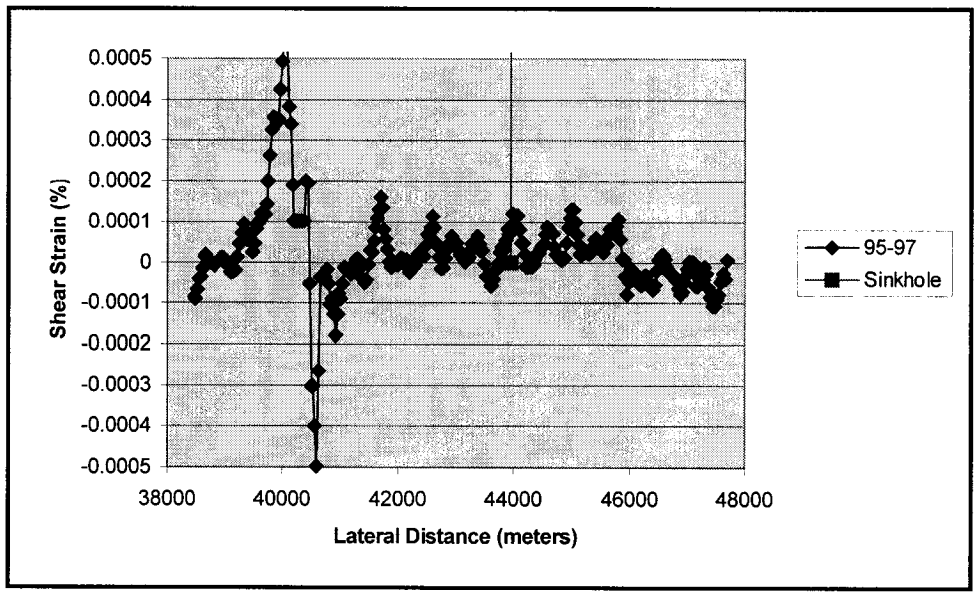

Figure 7.24: 1995-1997 Shear strains across the horizontal profile

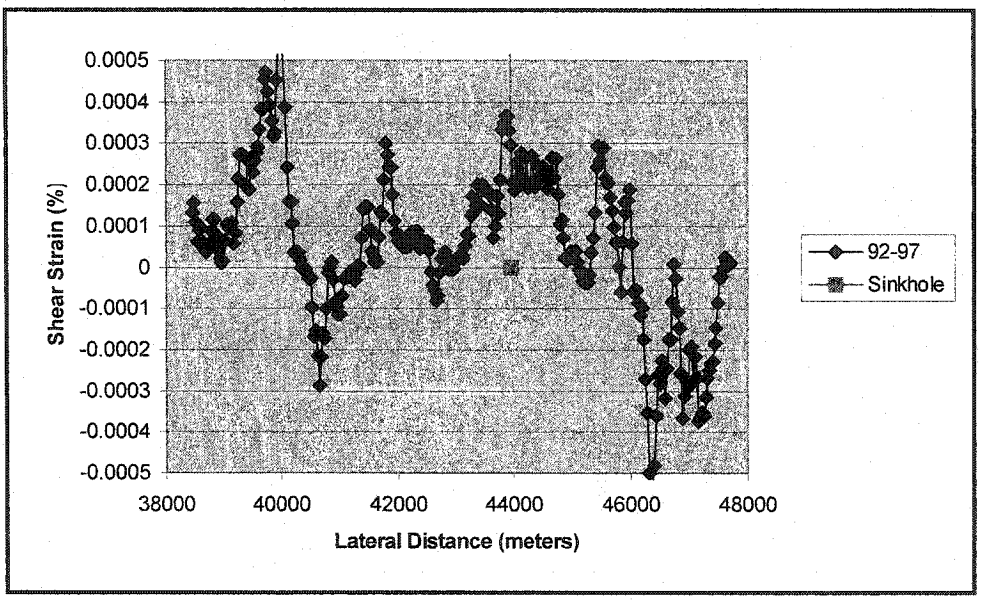

Figure 7.25: 1992-1997 Shear strains across the horizontal profile

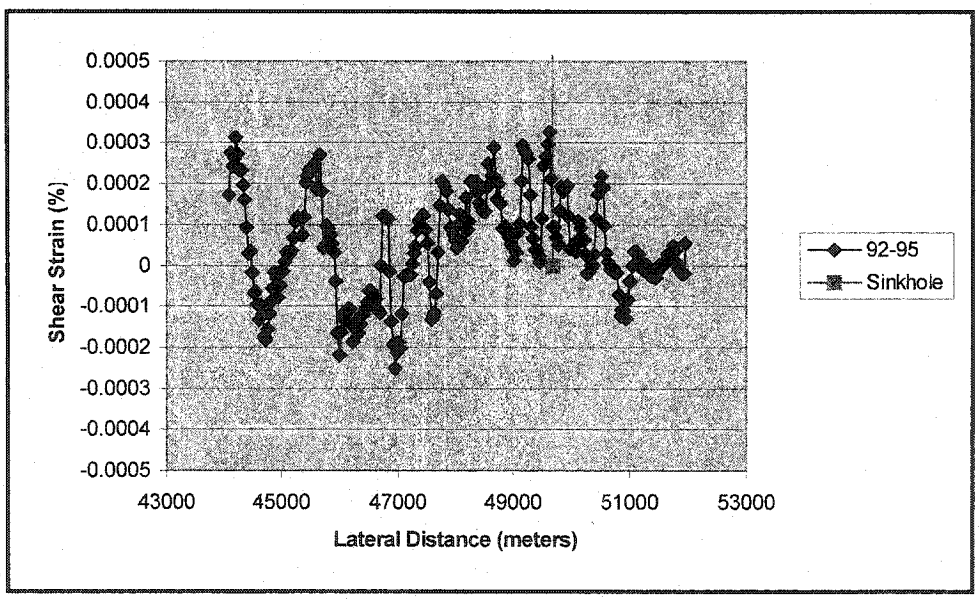

Figure 7.26: 1992-1995 Shear strains across the vertical profile

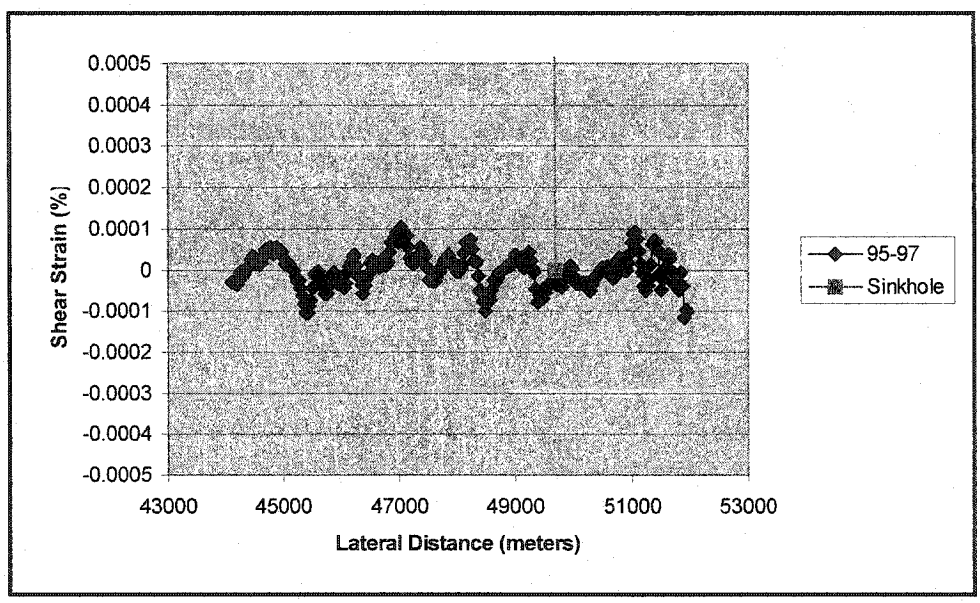

Figure 7.27: 1995-1997 Shear strains across the vertical profile

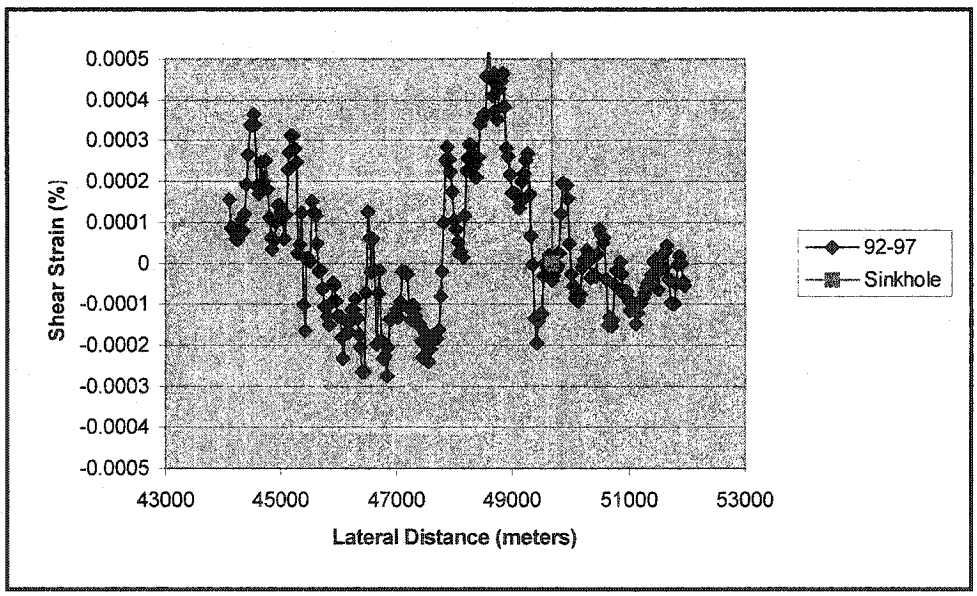

Figure 7.28: 1992-1997 Shear strains across the vertical profile

$\left(\alpha_h - \frac{3\pi}{2}\right)$ as stated by Hanssen (2001) corresponds with the angle to the azimuth look direction, which, for a right-looking radar, is perpendicular to the satellite heading (Hanssen, 2001). Hanssen (2001) further points out that due to the projection of the three-dimensional displacement vector to the radar line-of-sight, it is not possible to retrieve the full displacement vector from either a single look direction nor from both an ascending and descending look directions. In order to retrieve two components of this three-dimensional displacement vector, a combination of interferograms generated from both ascending and descending tracks should be analyzed. To obtain the displacement vector third component, assumptions of the characteristics of the displacement in the area should be made.

From the generated interferograms one can notice that the majority of deformation in the Devil's Throat area of the Gold Butte district is positive, which indicates that the range change increases over the studied period since we are processing the interferograms in a decreasing time period order (i.e. 1997-1992). Since the interferograms were generated using a descending track data, where a ERS radar sensor is looking to the right, or rather, to the west, an increase in the range in this direction indicates that the study area is either subsiding or extending to the west, away from the satellite. In this research, all deformation values determined were left in terms of slant range deformation. After looking into all the available research conducted in this area, it was also assumed that subsidence is the dominant vertical motion.

7.7. Conclusion

Using InSAR in the Devils Throat sinkhole area, we were able to observe:

1. Subsidence of about 0.3-0.5 cm/year
2. Steep gradient in displacement rates on the eastern part of the constructed profile where the Devils Throat Sinkhole occurs.

Deformation rates generated from adding up interferograms A (1995-1992) and B (1997-1995) agreed very well with those generated using interferogram C (1997-1992) meaning that the results agree well with the expected deformations in the area. These results along with the dry weather conditions reported during data acquisition periods also indicate to some extent that almost no atmospheric errors were introduced in the generated interferograms. However, more interferograms of the Devil's Throat area should be analyzed and carefully compared to be certain that no such errors are present.

Since all deformation values determined were left in terms of slant range deformation, processing additional sets of SLC images of an ascending orbit along with assumptions of the ground surface motion based on other studies conducted in the area is necessary to aid in the decomposition of the three dimensional displacement vector.

8. Summary and Conclusion

8.1.Summary

The instability of Karst has caused great damage to roads, buildings, airports and lifelines all over the world and is responsible for millions of dollars of damage to public and private property every year. These Sinkholes are continuously unstable, unexpected and are commonly accompanied with not only significant property and environmental damage but also pose a serious threat to human lives.

Since Karst occur in many parts of the world which makes it a worldwide threat that should be taken seriously, the study of this worldwide phenomenon is very important as it helps in understanding the events that lead to it and aids in the design to prevent or at least minimize the outcomes of future collapses.

The aim of this research was to apply Synthetic Aperture Radar (SAR) techniques (Zebker and Goldstein, 1986) to determine the surface deformation in Karstic regions and demonstrates the utility of SAR interferometry in investigating the phenomenon.

Synthetic Aperture Radar (SAR), an imaging radar system, is one of the most advanced engineering inventions of the twentieth century (Soumekh, 1999). SAR images used in such a technique offers a large scale and fine resolution data sets making it a great tool that can be used to obtain information about the rate and extent of subsidence in a particular area.

The study was divided into three different tasks. The first task was to construct a database of selected sinkhole case histories, from all around the world, and determine whether these sinkhole dimensions meets the minimum radar resolution requirements.

The second task involved determining the minimum extent of deformation area that InSAR can detect by conducting a feasibility study that investigates the affects of an underground circular cavity on the ground surface. This study was used to determine both the minimum cavity diameter and depth below ground surface causing a settlement trough that can be distinguished by radars.

The final task was to use differential interferometry techniques to produce interferograms of subsidence, a task that involved processing of raw SAR data provided by the European Space Agency to generate Single Look Complex (SLC) SAR images, which are later, used to generate an interferogram that is analyzed to determine surface deformations.

In this last task ROI_PAC, an interferometric software developed by JPL/Caltech, was used to generate a Synthetic Aperture Radar (SAR) interferogram of an area, were a sinkhole has occurred, to assess the effectiveness of the technique in detecting very small ground surface fluctuations.

The temporal coverage of SAR images (1992-1997), used in this study, provided a great tool to monitor and accurately measure the rates of subsidence in the Devil's Throat area, Nevada, where sinkholes exist.

8.2.Conclusion

The case histories of the developed database, presented in chapter 3 of this dissertation, were compared to the resolution of the proposed method to determine whether they could have been detected if such method would have been used to study them. Only 51.2% of the collected case histories provided sinkhole width and depth information and thus could be used in such a comparison.

Since SAR interferometry has been reported to be able to detect ground surface fluctuations in the order of centimeters with good resolution (10m) over large swaths (50km) (Gabriel et al., 1989), only individual objects that are around 10m wide or large could be discern by this technique. Given that, 54.7% of the collected case histories with width and depth information could have been detected. This technique could not have been used to detect the other 45.23% of the case histories included in the developed database, as their widths were way below the technique's resolution.

From the results of the preliminary parametric study, presented in chapter 5 of this dissertation, it may be concluded that the ground subsidence due to the existence of subsurface cavities can be sufficiently large to be detected using SAR interferometry, provided that the cavity has a radius larger than 2.4 meters and located 4 meters below ground surface in clay.

In sand, the minimum tunnel radius and depth below surface to tunnel axis should be 2.6 and 7 meters respectively. The magnitude and width of subsidence trough caused by such sized cavities are close to the present resolution limits of SAR systems.

It can also be concluded that as depth below surface to tunnel axis increases, the tunnel radius required to cause a measurable settlement magnitude and width of trough decreases.

Using InSAR in the Devil's Throat sinkhole area, we were able to observe subsidence of about 0.3-0.5 cm/year with steep gradient in displacement rates on the eastern part of the constructed profile where the Devil's Throat Sinkhole occurs.

Deformation rates generated from adding up the 1992-1995 interferogram with the 1995-1997 interferogram agreed very well with those generated from the 1992-1997 interferogram. These results along with the dry weather conditions reported during data acquisition periods indicate to some extent that almost no atmospheric errors were introduced in the generated interferograms. However, more interferograms of the Devil's Throat area should be analyzed and carefully compared to be certain that no such errors are present.

Since all deformation values determined were left in terms of slant range deformation, processing additional sets of SLC images of an ascending orbit along with assumptions of the ground surface motion based on other studies conducted in the area is necessary to aid in the decomposition of the three dimensional displacement vector.

From all the above, it can be concluded that deformations across the Devil's Throat area as observed using InSAR coincide well with the expected surface motion direction in the area.

8.3.Future research

For the future research within the framework of using the present technique, several factors, which may contribute to the improvements of the produced results, could be taken into consideration. Such factors involved the following suggestions: .

1- Analyze and validate InSAR interferograms against existing subsidence monitoring methods to determine if InSAR interferograms can be used as a viable option for subsidence monitoring.
2- Process additional sets of SLC images with short temporal baselines.
3- Process additional sets of SLC images of an ascending orbit to help in the decomposition of the displacement vector.
4- Compare interferometry results with deformation model developed on GPS data if available.
5- Generate interferograms using data acquired by the new European Space Agency Satellite "ENVISAT" to produce more accurate results.

References

Al-Mutairi N., Eid, W., Abdullah, W., Misak, R., Mollah, M., Awny, R., Al-Fahad, F., 1998, "Evaluation and treatment of underground cavities at Al-Dhahar area", EB001K, Vol.1, Kuwait institute for scientific research.

Al-Refaiy I., 1990, "Land subsidence in the Al-Dahr residential area in Kuwait: a case history study", *Quarterly journal of engineering geology*, London, Vol.23, pp.337-346.

Amelung, F., Galloway, D., Bell, J., Zebker, H., and Laczniak, R., 1999, "Sensing the ups and downs of Las Vegas: InSAR reveals structural control of land subsidence and aquifer-system deformation", *Geology*, Vol. 27, No.6, pp.483-486.

Attewell, P., and Farmer, I., 1976, *Principles of engineering geology*, John Wiley and Sons, INC. NY, 1045p.

Attewell, P., 1995, *Tunneling contracts and site investigation*, E and FN SPON. UK. 378p.

Avallone, A., Zollo, A., Briole, P., Delacoourt, C., and Beauducel, F., 1999, "Subsidence of Campi Flegrei (Italy) detected by SAR interferometry", *Geophysical Research Letters*, Vol. 26, No. 15, pp. 2303-2306.

Baer, G., Sandwell, D., Williams, S., Bock, Y., and Shamir, G., 1999, "Coseismic deformation associated with the November 1995, M_W= 7.1 Nuweiba earthquake, Gulf of Elat (Aqaba), detected by synthetic aperture radar interferometry, *Journal of Geophysical Research*, Vol. 104, No. B11, pp. 25221-25232.

Barbieri, M., Lichtenegger, J., and Calabresi, G., 1999, "The Izmit Earthquake: A Quick Post-Seismic Analysis with Satellite Observations", *ESA Bulletin*, No. 100, pp107-110.

Bardet, J.P., 1997, *Experimental soil mechanics*, Prentice-Hall, Inc., Upper River, New Jersey, 583p.

Beck B., 1984, "Sinkhole terminology", *proceedings of the first multidisciplinary conference on sinkholes*, Orlando, Florida, 15-17 October 1984, pp. ix-x.

Benson R. and La Fountain L., 1984, "Evaluation of subsidence or collapse potential due to subsurface cavities", *Proceedings of the first multidisciplinary conference on sinkholes*, Orlando, Florida, pp. 201-214.

Bickel, J., Kuesel, T., and King, E., 1996, *Tunnel engineering handbook*, Chapman and Hall, second edition, 544p.

Brink A., 1984, "A brief review of the South African sinkhole problem", *Proceedings of the first multidisciplinary conference on sinkholes*, Orlando, Florida, pp. 123-127.

van Bree, R., Gens, R. Groot, J., van Halsem, D., Hanssen, R., van den Hout, P., Klees, R., de Min ans E J O Schrama, E., and Usai, S., 2000, " Deformation measurements with SAR", Vol. USP-2, 99-16, Beleidscommissie Remote Sensing, Delft.

Briole, P., Massonnet, D., and Delacourt, C., 1997, "Post-eruptive deformation associated with the 1986-87 and 1989 lava flows of Etna detected by radar interferometry", *Geophysical Research Letters*, Vol. 24, pp. 37-40.

Buckley, S., 2000, *Radar Interferometry Measurement of Land Subsidence*, PhD dissertation, The University of Texas at Austin, 229p.

Burgmann, R., Rosen, P., Fielding, E., 2000, "Synthetic aperture radar interferometry to measure earth's surface topography and its deformations", *Annual review of earth planetary*, Vol. 28, pp. 169-209.

Burgmann, R., Schmidr, D., Nadeau, R., d'Alessio, M., Fielding, E., Manaker, D., McEvilly, T., and Murray, M., 2000b, "Earthquake potential along the Northern Hayward Fault, California", *Science*, Vol. 289, pp. 1178-1182.

Carnec, C., and Fabriol, H., 1999, "Monitoring and modeling land subsidence at the Cerro Prieto geothermal field, Baja California, Mexico, using SAR interferometry", *Geophysical Research Letters*, Vol. 26, No. 9, pp. 1211-1215.

Carnec, C., Massonnet, D., and King, C., 1996, "Two examples of the use of SAR interferometry on displacement fields of small spatial extent". *Geophysical Research Letters*, Vol. 23, No., 24, pp. 3579-3582.

Chillingarian, G., Yen, T., and Donaldson, E., 1995, *Subsidence due to fluid withdrawal*. Elsevier Health Sciences, 516p.

Chilingarian, G., and Endres, B., 1997, " Land subsidence due to fluid withdrawal". Second Annual Symposium on Groundwater Resources and Groundwater Quality Protection, Jan 9-10, Cheng Kung University, Tainan, Taiwan, pp. 1-13.

Codd, E., 1970, "A relational model for large shared data banks", *CACM*, Vol. 13, No. 6.

Coltelli, M., Fornaro, G., Franceschetti, G., Lanari, R., Migliaccio, M., ao R Moreira, J., Papatanassiou, K., Puglisi, G., Riccio, D., and Schwabisch, M., 1996, "SIR-C/X SAR multifrequency multipass interferometry: A new tool for geological interpretation", *Journal of Geophysical Research*, Vol.101, No.E10, pp. 23127-23148.

Clarke, P., Paradissi, D., Briole, P., England, P., Parsons, B., Billiris, H, Veis, G, and Ruegg, J., 1996, "Geodetic investigation of the 13 May 1995 Kozani-Grevena (Greece) earthquake" *Geophysical Research Letters*, Vol.. 24, pp. 707-710.

Cording, E. and Hansmire, W., 1975, "Displacements around soft ground tunnels", *Proceedings of the 5th Pan American congress on soil mechanics and foundation engineering*, Buenos Aires. pp. 571-633.

Culander, J.C., and McDonough, R.N., 1991, *Synthetic Aperture Radar: System and Signal Processing*. John Wiley & Sons, New York, 647p.

Delacourt, C., Briole, P., Achache, J., Fruneau, B., and Carnec, C., 1997, "Correction of the topospheric delay in SAR interferometry and application to 1991-93 eruption of Etna volcano, Italy" in: *AGU Fall meeting,* December 8-12, San Francisco, USA.

Elachi, C., Bicknell, T., Jordan, R., and Wu, C., 1982, "Spaceborne Synthetic Aperture imaging radar: Applications, techniques and technology", *Proceedings of the IEEE*, Vol.70, No.10, pp. 1174-1209.

Elmasri, R., and Navathe, S., 2000, *fundamentals of database systems*, 3rd edition, Addison Wesley Longman, Inc.

Eschbach, P., 1981, "Winter Park history and archives collection, the Phil Eschbach collection."<http://www.wppl.org/wphistory/PhilEschbach/WinterParkSinkhole10May1981.jpg>.

Evans, J., and Hagfors, T., 1968, *Radar astronomy*, McGraw-Hill, New York.

Feigl, K., Sergent , A., and Jjacq, D., 1995, " Estimation of an earthquake focal mechanism from a satellite radar interferogram: Application to the December 4, 1992 Landers aftershock", *Geophysical Research Letters*, Vol. 22, No., 9, pp.1037-1040.

Ferretti, A., Prati, C., and Rocca, F., 2000, "Nonlinear subsidence rate estimation using permanent scatterers in differential SAR interferometry", *IEEE Transactions on Geoscience and Remote Sensing*, Vol. 38, No. 5, pp. 2202-2212.

Fialko, Y., and Simons, M., 2000, "Deformation and seismicity in the Coso geothermal area, Inyo County, California: Observations and modeling using satellite radar interferometry", *Journal of Geophysical Research*, Vol. 105, No., B9, pp. 21781-21794.

Fischer, J., Graham, T., Greene, R., Canace, R., and Fischer, J., 1989, "Practical concerns of Cambro-Ordovician karst sites", *Proceedings of the third multidisciplinary conference on sinkholes*, Orlando, Florida.

Franceschetti, G., Lanari, R., 1999, "Synthetic Aperture Radar Processing", *Electronic engineering systems series*, CRC Press.

Freeman, T., 2000, *What is imaging radar*, Jet Propulsion Laboratory.

Fruneau, B., Rudant, J., Obert, D., and Raymond, D., 1998, "Small displacements detected by SAR interferometry on the city of Paris, France", In: *Second Int. Workshop on Retrieval of Bio- and Geophysical Parameters from SAR data from Land Applications,* 21-23 Oct., Noordwijk, The Netherlands, ESTEC.

Fujiwara, S., Yarai, H., Ozawa, S., Tobita, M., Murakami, M., Nakagawa, H., Nitta, K., Rosen, P., and Werner C., 1998, "Surface displacement of the March 26, 1997 Kagoshima-kenhokuseibu earthquake in Japan from synthetic aperture radar interferometry", *Geophysical Research Letters,* Vol. 25, No., 24, pp. 4541-4544.

Fuliwara, S., Rosen, P., Tobita, M., and Murakami, M., 1998, "Crustal deformation measurements using repeat-pass JERS-1 synthetic aperture radar interferometry near the Izu Peninsula, Japan", *journal of Geophysical Research,* Vol. 103, No., B2, pp. 2411-2426.

Gabriel, A., and Goldstein, R., 1988, "Crossed orbit interferometry: theory and experimental results from SIR-B", *International Journal on Remote Sensing*, Vol 9, No. 5, pp. 857-872.

Gabriel, A., Goldstein, R., and Zebker, H. A., 1989, "Mapping small elevation changes over large areas: Differential radar interferometry", *Journal of Geophysical Research*, Vol. 94, No. B7. pp9183-9191.

Galloway, D., Hudnut, K., Ingebritsen, S., Phillips, S., Peltzer, G., Rogez, F., and Rosen, P., 1998, "Detection of aquifer system compaction and land subsidence using interferometric synthetic aperture radar, Antelope Valley, Mojave Desert, California", *Water Resources Research,* Vol. 34, No. 10, pp. 2573-2585.

Gatelli, F., Guarnieri, A.M., Parizzi, F., Pasquali, P., Prati, C., and Rocca, F., 1994, "The Wavenumber Shift in SAR Interferometry", *IEEE Transaction on Geoscience and remote Sensing,* Vol.32 No.4, pp. 855-865.

Ghaboussi, J., Ranken, R., and Karshenas, M., 1978, "Analysis of subsidence over soft-ground tunnels", *International conference on evaluation and prediction of subsidence*, Pensacola Beach, Florida, pp. 182-196.

Gilluly, J., Waters, A., and Woodford, A., 1959, *Principles of geology*, 2nd ed.: W.H. freeman and Co., San Francisco, 534p.

Goldstein, R.M., Howard, A., Zebker, A., Werner, C.L., 1988, "satellite radar interferometry: Two-dimensional phase unwrapping", *Radio Science*, Vol. 23, No. 4, pp. 713-720.

Goldstein, R., Engelhardt, H., Kamp, B., and Frolich, R., 1993. "Satellite radar interferometry for monitoring ice sheet motion: Application to an Antarctic ice stream", *Science,* Vol. 262, pp. 1525-1530.

Goldstein, R.M., and Werner, C.L., 1998, "Radar Interferogram filtering for geophysical applications", *Geophysical Research Letters*, Vol. 25, No. 21, pp. 4035-4038.

Hagberg, J.O., Ulander, L.M. and Askne, J., 1995, "Repeat-Pass SAR Interferometry over Forested Terrain", *IEEE Transactions on Geoscience and Remote Sensing*, Vol. 33, pp. 331-340.

Hanssen, R., and Usai, S., 1997, "Interferometric phase analysis for monitoring slow deformation processes", In: *Third ERS Symposium-Space at the service of our environment,* Florence, Italy, 17-21 March 1997, ESA SP-414, pp.487-491.

Hanssen, R., Amelung, F., and Zebker, H., 1998a, "Geodetic interpretation of land subsidence measurements at the Cerro Prieto geothermal field monitored by radar interferometry, *EOS Transactions, AGU,* Vol. 79, No., 45, pp. F37.

Hanssen, R., Vermeersen, B., Scharroo, R., Kampes, B., Usai, S., Gens, R., and Klees, R., 2000a, "Deformatiepatroon van de aardbeving van 17 augustus 1999 in Turkije gemeten met satellite radar interferometry", *Remote Sensing Nieuwsbrief,* Vol. 90, pp. 42-44, In Dutch.

Hanssen, R. F., 2001, *Radar Interferometry- Data interpretation and error analysis, Remote sensing and digital image processing*, Kluwer Academic Publishers, Dordrecht, Netherlands, 308p.

Hartl, P., Thiel, K., and Wu, X., 1994a, "Information extraction from ERS-1 SAR data by means of INSAR and D-INSAR techniques in Antarctic research", In: *Second ERS-1 Symposium-Space at the Serice of our environment,* Hamburg, Germany, 11-14 October 1993, ESA SP-361, pp. 697-701.

Henderson, F., and Lewis, A., 1998, "Principles and Applications of Imaging Radar", *Manual of Remote Sensing*, 3rd Edition, Vol. 2. American Society for Photogrammetry and Remote Sensing, Wiley, New York.

Hernandez, B., Cotton, F., Campillo, M., and Massonet, D., 1997, "A comparison between short term (co-seismic) and long term (one year) slip for the Landers earthquake: Measurements from strong motion and SAR interferometry", *Geophysical Research Letters,* Vol. 24, No. 13, pp. 1579-1582.

Hoen, E., and Zebker, H., 2000, "Penetration depths inferred from interferometric volume decorrelation observed over the Greenland ice sheet", *IEEE Transaction on Geoscience and Remote Sensing,* Vol. 38, No., 6, pp. 2571-2583.

Hollingshead J., 1984, "A contour map, volume estimate, and description of Teague's sinkhole", *Proceedings of the first multidisciplinary conference on sinkholes*, Orlando, Florida. PP. 105-109.

Jackson, D., 1982, *Underground Worlds: time-life books*, Inc., Alexandria, VA, 176p.

Jammal S., 1984, "Maturation of the Winter Park sinkhole", *Proceedings of the first multidisciplinary conference on sinkholes*, Orlando, Florida. pp. 363-369.

Jennings, J.N., 1971, *KARST: An introduction to systematic geomorphology*, The M.I.T. Press, London, England, V.7, 252 p.

Jónsson, S., Zebker, H., Cervelli, P., Segall, P., Garbeil, H., Mouginis-Mark, P., and Rowland, S., 1999, " A shallow-dipping dike fed the 1995 flank eruption at Fernandina volcano, Galápagos, observed by satellite radar interferometry", *Geophysical Research Letters,* Vol. 26, No.8, pp. 1077-1080.

Joughin, I., Gray, L., Bindschadler, R., Price, S., Morse, D., Hulbe, C., Mattar, K., and Werner, C., 1999, "Tributaries of west Antarctic ice streams revealed by RADARSAT interferometry", *Science,* Vol. 286, No., 5438, pp. 263-286.

Joughin, I, 1995, "Estimation of ice-sheet topography and motion using interferometric synthetic aperture radar", Ph.D. thesis, University of Washington.

Joughin, I., Fahnestock, M., Ekholm, S., and Kwok, R., 1997, " Balance velocities of the Greenland ice sheet", *geophysical Research Letters,* Vol. 24, No. 23, pp. 3045-3048.

Joughin, I., Kwok, R., and Fahnestock, M., 1998, "Interferometric estimation of three-dimensional ice-flow using ascending and descending passes", *IEEE Transactions on Geoscience and Remote Sensing,* Vol. 36, No. 1, pp. 25-37.

Kastning, E., 1989, "Surficial karst patterns: Recognition and interpretation", *Proceedings of the third multidisciplinary conference on sinkholes*, Orlando, Florida.

Kawai, S., and Shimada, M., 1994, " Detections of earth surface deformation change by means of INSAR technique", In: *paper presented at the 1st workshop on SAR interferometry,* Tokyo, Japan, December 1994, NASDA.

Klinger, Y., Michel, R., and Avouac, J, 2000, "Co-seismic deformation during the Mw 7.3 Aqaba earthquake (1995) from ERS-SAR interferometry", *Geophysical Research Letters,* Vol. 27, No. 22, pp. 3651-3655.

Kwok, R., and Fahnestock, M., 1996, "Ice sheet motion and topography from radar interferometry", *IEEE Transactions on Geoscience and Remote Sensing,* Vol. 34, No. 1, pp. 189-200.

Lamoreaux P., 1984, "Catastrophic subsidence, Shelby County, Alabama", *Proceedings of the first multidisciplinary conference on sinkholes*, Orlando, Florida. PP. 131-136.

Lanari, R., Fornaro, G., Riccio, D., Migliaccio, M., Papathanassiou, K., ao R Moreira, J., Schwabisch, M., Dutra, L., Puglisi, G., Franceschetti, G., and Coltelli, M., 1996, "Generation of Digital Elevation Models by usin SIR-C/X-SAR multifrequency two-pass interferometry: The Etna case study", *IEEE transactions on Geoscience and remote sensing*, Vol. 34 (5), P. 1097-1114.

Lanari, R., Lundgren, P., and Sansosti, E., 1998, "Dynamic deformation of Etna volcano observed by satellite radar interferometry", *Geophysical Research Letters,* Vol. 25, pp. 1541-1544.

Lane E., 1986, *Karst in Florida*, The bureau of geology, special publication No. 29.

Lee, C., Wu, B., and Chiou, S., 1999, "Soil movements around a tunnel in soft soils", *Proceedings of the national councel,* Vol. 23, No., 2, pp. 235-247.

Littlefield J., Culbreth M., Upchurch S. & Stewart M., 1984, "Relationship of modern sinkhole development to large scale-photolinear features", *Proceedings of the first multidisciplinary conference on sinkholes*, Orlando, Florida. pp. 189-195.

Lu, Z., Fatland, R., Wyss, M., Li, S., Eichelberger, J., Dean, K., and Freymueller, J., 1997, "Deformation of New Trident volcano measured by ERS 1 SAR interferometry, Katmi National Park, Alaska", *Geophysical Research Letters,* Vol. 24, No. 6, pp. 695-698.

Lu, Z., and Freymueller, J., 1999, " Synthetic aperture radar interferometry coherence analysis over Katmai volcano group, Alaska", *Journal of Geophysical Research,* Vol. 103, No. B12, pp. 29887-2894.

Madsen, S., 1989, "Estimating the Doppler Centroid of SAR Data", *IEEE Transactions on Aerospace and Electronic Systems*, Vol. AES-25, March. pp. 134-140.

Madsen, S.N., and Zebker, H.A., 1992, "Automated absolute phase retrieval in cross-track interferometry", *Proceedings of the 1992 International geoscience and remote sensing symposium*, Houston, TX, pp 1582-1584.

Madsen, S.N., Martin, J.M., and Zebker, H.A., 1993, "Topographic mapping using radar interferometry: processing techniques", *IEEE transactions of geoscience and remote sensing*, Vol. 31, pp. 246-256.

Madsen, S.N., Martin, J.M., and Zebker, H.A., 1995, "Analysis and evaluation of the NASA/JPL TOPSAR across-track interferometric SAR system", *IEEE transactions on geoscience and remote sensing*, Vol. 33, No. 2, pp. 383-391.

Mair, R., Taylor, R., and Bracegirdle, A., 1993, "Subsurface settlement profiles above tunnels in clays", *Geotechnique,* Vol. 43, No., 2, pp.315-320.

Massonnet, D., and Adranga, F., 1993, " A full-scale validation of Radar Interferometry with ERS-1: the Landers earthquake", *Earth Observation Quarterly,* Vol. 41.

Massonnet, D., Rossi, M., Carmona, C. Adragna, Pletzer, F. G. Feigl, K. and Rabaute, T., 1993, "The displacements field of the Landers earthquake mapped by radar interferometry", *Nature*, Vol. 364, pp. 138-142.

Massonnet, D., Feigl K., Rossi, M. and Adragna, F., 1994, "Radar interferometric mapping of deformation in the year after the Landers Earthquake", *Nature*, Vol. 369, pp. 227-230.

Massonnet, D., Briole, P., and Arnaud, A., 1995, " Deflation of Mount Etna monitored by spaceborne radar interferometry", *Nature,* Vol. 375, pp. 567-570.

Massonet, D. and Feigl, K., 1995b, "Discrimination of geophysical phenomenon in satellite radar interferograms", *Geophysical Research Letters*, Vol. 22, No. 12, pp. 1537-1540.

Massonnet, D., Feigl, K., Vadon, H., and Rossi, M., 1996a, " Coseismic deformation field of the M=6.7 Northridge, California earthquake of January 17, 1994 recorded by two radar satellites using interferometry", *Geophysical Research Letters,* Vol. 23, No. 9, pp. 969-972.

Massonnet, D., Holzer, T., and Vadon, H., 1997, " Land subsidence caused by the East Mesa geothermal field, California, observed using SAR interferometry", *Geophysical Research Letters,* Vol. 24, No., 8, pp. 901-904, Correction in *GRL* Vol . 25, No. 16, pp.3213, 1998.

Massonet, D. and Feigl, K., 1998, "Radar interferometry and its application to changes in the Earth's surface", *Reviews in Geophysics*, v. 36, pp. 441-500.

Meyer, B., Armijo., R., Massonnet, D., de Chablier, J., Delacourt, C., Ruegg, J., Achache, J., Briole, P., and Panastassiou, D., 1996, "The 1995 Grevena (North Greece) earthquake: fault model constrained with tectonic observations and SAR interferometry", *Geophysical Research Letters,* Vol. 23, pp. 2677-2680.

Mayer, L., Lu, Z., 2001, "Elastic rebound following the Kocaeli earthquake, Turkey, recorded using synthetic aperture radar interferometry", *Geology*, Vol. 29, pp. 495-498.

Mellet, J., and Maccarillo, B., 1995, "A model for sinkhole formation on interstate and limited access highways, with suggestions on remediation", *Proceedings of the fifth multidisciplinary conference on sinkholes*, Gatlinburg, Tennessee.

Michel, R., Avouac, J., and Taboury, J., 1999, " Masurin ground displacement from SAR amplitude images: applicationto the Landers earthquake, *Geophysical Research Letters,* Vol. 26, No. 7, pp. 875-878.

Mohr, J. J., Madsen, S. N., 1995, "Application of Interferometry to studies of glacier dynamics",<http://www.emi.dtu.dk/research/DCRS/Science/Landice/Data/glac.pdf>.

Mohr, J., 1997, " Repeat track SAR interferometry. An investigation of its utility for studies of glacier dynamics", *Ph.D. thesis*, Technical University of Denmark, Copenhagen.

Murakami, M., Tobita, M., Fujiwara, S., and Saito, T., 1996, "Coseismic crustal deformation of 1994 Northridge, California, earthquake detected by interferometric JERS-1 synthetic aperture radar", *Journal of Geophysical Research,* Vol. 101, No. B4, pp. 8605-8614.

Newton J. 1984, "Review of induced sinkhole development", *Proceedings of the first multidisciplinary conference on sinkholes*, Orlando, Florida. pp. 3-9.

Newton J. 1987, *Development of sinkholes resulting from man's activities in the Eastern United States*, U.S. Geological survey, circular 968.

Ogden, A.E. ,1984, "Methods for describing and predicting the occurrence of sinkholes", *Proceedings of the first multidisciplinary conference on sinkholes*, Orlando, Florida. pp. 177-182.

Ohkura, H., 1998, "Applications of SAR data to monitoring earth surface changes and displacements", *Advances I Space Research,* Vol. 21, No. 3, pp. 485-492.

Oppenheim, A. V., and R. W. Schafer, 1989, *Discrete-Time Signal Processing*, Prentice Hall. 879 p.

Ozawa, S., Murakami, M., Fujiwara, S., and Tobita, M., 1997, "Synthetic aperture radar interferogram of the 1995 Kobe earthquake and its geodetic inversion", *Geophysical Research Letters,* Vol. 24, No. 18, pp. 2327-2330.

Peck, R., 1969, "Deep excavations and tunneling in soft ground", *Proceedings of the 7th international conference on soil mechanics and foundation engineering*, pp.225-290.

Peltzer, G., Crampé, F., and King, G., 1999, "evidence of the nonlinear elasticity of the crust from Mw 7.6 Manyi (Tibet) earthquake", *Science,* Vol. 286, No. 5438, pp. 272-276.

Peltzer, G., Hudnut, K., and Feigl, K., 1994, "Analysis of coseismic surface displacement gradients using radar interferometry: New insights into the Landers earthquake", *Journal of Geophysical Research,* Vol. 99, No. B11, pp. 21971-21981.

Peltzer, G., and Rosen, P., 1995, "Surface displacement of the 17 May 1993 Eureka Valley, California earthquake observed by SAR interferometry", *Science,* Vol. 268, pp. 1333-1336.

Peltzer, G., Rosen, P., Rogez, F., and Hudnut, K., 1996, "Postseismic rebound in fault step-over caused by pore fluid flow", *Science*, Vol. 273, pp. 1202-1204.

Price, E., and Sandwell, D., 1998, " Small-scale deformations associated with the 1992 Landers, California, earthquake mapped by synthetic aperture radar interferometry phase gradients", *Journal of Geophysical Research,* Vol. 103, No. B11, pp. 27001-27016.

Reeves, R. G., 1975, *Manual of remote sensing, American society of photogrammetry*, Vol. 1, 1st edition, 2144p.

Reilinger, R., Ergintav, S., Burgmann, R., McClusky, S., Lenk, O., Barka, A., Gurkan, O., Hearn, l., Feigl, K., Cakmak, R., Aktug, B., Ozener, H., and Toksoz, M., 2000, "Coseismic and postseismic fault slip for the 17 August 1999, M= 7.5, Izmit, Turkey earthquake", *Science,* Vol. 289, No. 5484, pp. 1519-1524.

Richman, D., 1982, "Three-dimensional azimuth correcting mapping radar", *United States Patent*, No. 4321601, Originally filed in 1971.

Rignot, E., Gogineni, S., Krabill, W., and Ekholm, S., 1997, " North and northeast Greenland ice discharges from satellite radar interferometry", *Science,* Vol. 276, pp. 934-937.

Rosen P., Hensley, S., Zebker, H., Webb, F., and Fielding, E., 1996, " Surface deformation and coherence measurements of Kilauea volcano, Hawaii, from SIR-C radar interferometry", *Journal of Geophysical Research,* Vol. 101, No., E10, pp. 23109-23125.

Rosen P., Werner, C., Fielding, E., Hensley, S., and Vincent, S., 1998, " Aseismic creep along the San Andreas fault northwest of Parkfield, CA measured by radar interferometry", *Geophysical Research Letters,* Vol. 25, No. 6, pp. 825-828.

Rosen, P.A., Hensley, S., Joughin, I.R., Madsen, S.N., and Goldstein, R.M., 2000, "Synthetic aperture radar interferometry", *Proceedings of the IEEE*, Vol. 88, No.3, pp. 333-381.

Rosen, P. and Persaud, P., 2000, "ROI_PAC document", Abridged version of Chapter 3 of a Ph.D. thesis written by Sean Buckley CSR, UT Austin. 63 p.

Rosen, P., 2003, "Repeat Orbit Interferometry PACkage", ROI_PAC, Caltech/JPL <https://www.openchannelfoundation.org/projects/ROI_PAC/>.

Roth, A., Adam, N., Schwabisch, M., Muschen, B., Bohm, C., and Land, O., 1997, "Observation of the effects of the subglacial volcano eruption underneath the Vatnajokull glacier in Iceland with ERS-SAR data", In: *Proceedings of the third ERS symposium,* Florence, Italy, 17-20 March 1997.

Rott, H., and Siegel, A., 1997, "Glaciological studies in the Alps and Antarctica using ERS interferometric SAR", In: *'FRINGE 96' workshop on ERS SAR interferometry,* Zurich, Switzerland, 30 Sep. – 2 Oct. 1996, pp. 149-159, ESA SP-406, Vol . II.

Rott, H., Stuefer, M., Siegel, A., Skvarca, P., and Eckstaller, A., 1998, " mass fluxes and dynamics of Moreno Glacier, Southern Patagonia Icefield", *Geophysical Research Letters,* Vol. 29, No. 9, pp. 1407-1410.

Sagaseta, C., 1987, "Analysis of undrained soil deformation due to ground loss", *Geotechnique*, Vol. 37, No. 4. pp. 647-649.

Sandwell, D., and Sichoix, L., 2000, "Topographic phase recovery from stacked ERS interferometry and a low resolution Digital Elevation Model", *Journal of Geophysical Research,* Vol. 105, No., B12, pp. 28211-28222.

Schimdt, W., and Scott, T., 1984, "Florida karst- its relationship to geologic structure and stratigraphy", *Proceedings of the first multidisciplinary conference on sinkholes, Orlando*, Florida. pp. 11-16.

Shields, J., 1997, *SAR interferometry: An overview*, (updated 1997), <http://www.emporia.edu/earthsci/student/shields/sar2.htm>.

Shouyue, Z., 1984, "Karst and subsidence in China", *Proceedings of the first multidisciplinary conference on sinkholes*, Orlando, Florida. pp. 97-104.

Sigmundsson, F., Vadon, H., and Massonnet, D., 1997, "Readjustment of the Krafla spreading segment to crustal riftin measured by satellite radar interferometry", *Geophysical Research Letter,* Vol. 24, No. 15, pp. 1843-1846.

Silberschatz, A., Korth, H., and Sudarshan, S., 2002, *Database system concepts*, 4th edition, Mc Graw Hill.

Soumekh, M., 1999, *Synthetic Aperture Radar signal processing with MATLAB algorithms*, John Wiley & Sons, Inc.

Sowers, G., 1996, *Building on sinkholes, design and construction of foundations in karst terrain*, ASCE Press. 202p.

Steiner, R., 1975, "Reinforced earth bridge highway sinkhole", *Civil Engineering ASCE*, Vol. 45, No. 7, July, pp. 54-56.

Stramondo, S., Tesauro, M., Briole, P., Sansosti, E., Salvi, S., Lanari, R., Anzidei, M., Baldi, P., Fornaro, G., Avallone, A., Buongiorno, M., and Boschi, G., 1999, " The September 26, 1997, Colfiorito, Italy, earthquake: modeled coseismic surface displacement from SAR interferometry and GPS", *Geophysical Research Letters,* Vol. 26, No., 7, pp. 883-886.

Swanson, P. & Larson, T., 2000, "Case Closed", *Civil Engineering- ASCE*, Vol. 70, No. 6, pp. 42-45.

Sweeting, M., 1973, *Karst landforms*, New York, N.Y., Columbia U. Press, 362p.

Tesauro, M., Berardino, P., Lanari, R., Sansosti, E., Fornaro, G., and Franceschetti, G., 2000, " Urban subsidence inside the city of Napoli (Italy) observed by satellite radar interferometry", *Geophysical Research Letters,* Vol. 27, No. 13, pp. 1961.

Tubbs, B., 1997, "Astronomical optical interferometry, A literature review", (Updated 2000), <http://www.cus.cam.ac.uk/~rnt20/interferometry/ast_opt_int/page1.html>.

Travel Books USA, 2002, "America's Scenic Drives", Gold Butte, Roundabout Publications, < http://www.travelbooksusa.com/nv04.htm >

Usai, S., Gaudio, C., Borgstrom, S., and Achilli, V., 1999, " Monitoring terrain deformations at Phlegrean fields with SAR interferometry", In: *Second International Workshop on ERS SAR Interferometry, 'FRINGE 99',* liege, Belgium, 10-12 Nov. 1999, pp. 1-5, ESA.

Wadge, G., Scheuchl, B., and Stevens, N., 1999, " Spaceborne radar measurements of the eruption of Soufrier Hills volcano, Montserrat during 1996-1999", *Submitted to Journal of Volcanology and Geothermal Research.*

Wagener, F. and Day, P., 1984, "Construction on dolmite in South Africa", *Proceedings of the first multidisciplinary conference on sinkholes*, Orlando, Florida, pp. 403-411.

Werner, E., 1984, "Sinkhole prediction—Review of electrical resistivity methods", *Proceedings of the first multidisciplinary conference on sinkholes*, Orlando, Florida.

Whitman, D. & Gubbels, T., 1999, "Applications of GIS to the triggering phenomena of sinkholes in Central Florida, Hydrology and engineering geology of sinkholes and karst", *Proceedings of the seventh multidisciplinary conference on sinkholes*, Harrisburg, Pennsylvania, pp. 67-73.

Whittaker, B., and Frith, R., 1990, "Tunneling design, stability, and construction", *The institution of mining and metallurgy*, UK, 460p.

Wicks, Jr, C., Thatcher, W., and Dzurisin, D., 1998, " Migration of fluids beneath Yellowstone Caldera inferred from satellite radar interferometry", *Science,* Vol. 282, pp. 458-462.

Wiik, N., 2003, EO help, The ESA Earth Observation Missions Helpdesk Team. European Space Agency. Personal communication. October 3, 2003.

Williams, C., and Wadge, G., 1998, " The effects of topography on magma chamber deformation models: Application to Mt. Etna and radar interferometry", *Geophysical Research Letters,* Vol. 25, No. 10, pp. 1549-1552.

Wu, X., 1996, "Anwendung der radarinterferometrie zur Bestimmung der topographie und der Geschwindigkeitsfelder der Eisoberflachen antarkischer Gebiete, *Ph.D. thesis,* Universitat Stuttgart.

Yang, J. and Wang, M., 2002, *Evaluation of tunneling-induced downdrag on end-bearing piles*, (updated 2002), <http://www.ejge.com/2002/Ppr0214/Ppr0214.htm>

Zebker, H. A. and Goldstein, R. M., 1986, "Topographic mapping derived from Synthetic Aperture Radar measurements", *Journal of Geophysical Research*, Vol. 91, pp. 4993-4999.

Zebker, H. A., Rosen, P. A., Goldstein, R. M., Warner, C., and Gabriel, A., 1994, "On the derivation of coseismic displacement fields using differential radar interferometry", *Journal of Geophysical Research- solid earth,* Vol. 99, No. 10, pp. 19617-19634.

Zebker, H., Rosen, P., Hensley, S., and Mouginis-Mark, P., 1996, "Analysis of active lava flows on Kilauea volcano, Hawaii, using SIR-C radar correlation measurements", *Geology,* Vol. 24, pp. 495-498.

Zebker, H., Rosen, P., and Hensley, S., 1997, " Atmospheric effects in interferometric synthetic aperture radar surface deformation and topographic maps", *journal of Geophysical Research,* Vol. 102, No. B4, pp.7547-7563.

Zebker, H.A., and Lu, Y., 1998, "Phase unwrapping algorithms for radar interferometry: residue-cut, least squares, and synthesis algorithms", *Journal of optical society of America*, Vol. 15, No. 3, pp. 586-598.

Ziemer, R.E. and Tranter, W.H., 1995, *Principles of communications: Modulation, systems and noise*, 4th edition. John Willey and Sons. 802p.

Zisk, S., 1972, "Lunar topography: First radar-interferometer measurements of the Alphonsus-Arzachel region", *Science*, Vol. 178, No. 4064, pp. 977-980.

Appendix A

Scene Date (yyyymmdd)	ESA Satellite
19920611	ERS-1
19920802	ERS-1
19920924	ERS-1
19930422	ERS-1
19930701	ERS-1
19930909	ERS-1
19950415	ERS-1
19950520	ERS-1
19950902	ERS-1
19951007	ERS-1
19951111	ERS-1
19951216	ERS-1
19960120	ERS-1
19960330	ERS-1
19951008	ERS-2
19951112	ERS-2
19960121	ERS-2
19960331	ERS-2
19960505	ERS-2
19960714	ERS-2
19960818	ERS-2
19961027	ERS-2
19961201	ERS-2
19970105	ERS-2
19970209	ERS-2
19970316	ERS-2
19970525	ERS-2
19970629	ERS-2
19970803	ERS-2

Table A1: Available ESA archive scene of track 84 frame 2871

Scene Date (yyyymmdd)	ESA Satellite
19970907	ERS-2
19980125	ERS-2
19980301	ERS-2
19980510	ERS-2
19981206	ERS-2
19990808	ERS-2
19991226	ERS-2
20000305	ERS-2
20000409	ERS-2
20000618	ERS-2
20000827	ERS-2
20011125	ERS-2
20020414	ERS-2

Table A2: Available ESA archive scene of track 84 frame 2871

Scene 1 Date (yyyymmdd)	Scene 2 Date (yyyymmdd)	Perpendicular Baseline (meters)
19951007	19920611	89
19951111	19920611	79
19960714	19920611	57
19970209	19920611	34
19970907	19920611	1
19991226	19920611	75
19950415	19920820	28
19951112	19920820	20
19960121	19920820	85
19970316	19920820	11
19970525	19920820	81
19970803	19920820	98
19950902	19920924	30
19960818	19920924	45
19980125	19920924	4
20000305	19920924	59
19930909	19930422	55
19951216	19930422	32
19960505	19930422	80
19980510	19930422	62
20000827	19930422	45
19950902	19930701	77
19960330	19930701	26
19960818	19930701	62
19970629	19930701	94
19981206	19930701	3
19951216	19930909	23
19960505	19930909	25
19961201	19930909	98

Table A3: InSAR pairs with perpendicular baseline $\leq$ 100 meters

Scene 1 Date (yyyymmdd)	Scene 2 Date (yyyymmdd)	Perpendicular Baseline (meters)
19990808	19930909	49
20000827	19930909	10
19951112	19950415	48
19960121	19950415	57
19970105	19950415	89
19970316	19950415	17
19970525	19950415	53
19970803	19950415	70
19960120	19950520	4
19960121	19950520	95
19970105	19950520	63
19970525	19950520	99
19970803	19950520	82
20000305	19950520	44
19960818	19950902	15
19970629	19950902	17
19980125	19950902	26
19981206	19950902	80
20000305	19950902	89
19970907	19951007	88
19991226	19951007	14
19960714	19951111	22
19970209	19951111	45
19970907	19951111	80
20011125	19951111	53
19960505	19951216	48
19980510	19951216	94
19990808	19951216	72
20000827	19951216	13

Table A4: InSAR pairs with perpendicular baseline $\leq$ 100 meters

Scene 1 Date (yyyymmdd)	Scene 2 Date (yyyymmdd)	Perpendicular Baseline (meters)
19960121	19960120	91
19970105	19960120	59
19970525	19960120	95
19970803	19960120	78
20000305	19960120	48
20000618	19960120	33
19960818	19960330	88
19981206	19960330	23
19960505	19960504	98
19961201	19960504	25
19990808	19960504	74
19961027	19951008	48
19970316	19951112	31
19970105	19960121	32
19970525	19960121	4
19970803	19960121	13
20000618	19960121	58
19961201	19960505	73
19990808	19960505	24
2000827	19960505	35
19970209	19960714	23
19970907	19960714	58
20011125	19960714	75
19970629	19960818	32
19980125	19960818	41
19981206	19960818	65
19990808	19961201	49
19970525	19970105	36
19970803	19970105	19

Table A5: InSAR pairs with perpendicular baseline $\leq$ 100 meters

Scene 1 Date (yyyymmdd)	Scene 2 Date (yyyymmdd)	Perpendicular Baseline (meters)
20000618	19970105	26
19970907	19970209	35
20011125	19970209	98
19970525	19970316	70
19970803	19970316	87
19970803	19970525	17
20000618	19970525	62
19980125	19970629	9
19981206	19970629	97
20000305	19970629	72
20000618	19970803	45
19991226	19970907	74
20000305	19980125	63
20000827	19990808	59
20000618	20000305	81
19960714	19920611	57
19970907	19920611	1
19950415	19920820	28
19970525	19920820	81
19970803	19920820	98
19950902	19920924	30
19960818	19920924	45
19970629	19920924	13
19960505	19930422	80
19980510	19930422	62
20000827	19930422	45
19950902	19930701	77
19960818	19930701	62
19970629	19930701	94
19951216	19930909	23

Table A6: InSAR pairs with perpendicular baseline $\leq$ 100 meters

Scene 1 Date (yyyymmdd)	Scene 2 Date (yyyymmdd)	Perpendicular Baseline (meters)
19961201	19930909	98
19990808	19930909	49
20000827	19930909	10
19960121	19950415	57
19970105	19950415	89
19970316	19950415	17
19970525	19950415	53
19970803	19950415	70
19970525	19950520	99
19970803	19950520	82
20000305	19950520	44
20000618	19950520	37
19960818	19950902	15
19970629	19950902	17
19970907	19951007	88
19991226	19951007	14
19970209	19951111	45
19970907	19951111	80
20011125	19951111	53
19960121	19960120	91
19970105	19960120	59
20000305	19960120	48
19960505	19960504	98
19990808	19960504	74
19961027	19951008	48
19970105	19960121	32
19970316	19960121	74
19990808	19960505	24
2000827	19960505	35

Table A7: Similar season InSAR pairs with perpendicular baseline $\leq$ 100 meters

Scene 1 Date (yyyymmdd)	Scene 2 Date (yyyymmdd)	Perpendicular Baseline (meters)
19970907	19960714	58
19970629	19960818	32
20011125	19970209	98
19970525	19970316	70
19970803	19970525	17
20000618	19970525	62
20000305	19970629	72
20000618	19970803	45
19991226	19970907	74
20000305	19980125	63
20000827	19990808	59
20000618	20000305	81

Table A8: Similar season InSAR pairs with perpendicular baseline $\leq$ 100 meters

Scene 1 Date (yyyymmdd)	Scene 2 Date (yyyymmdd)	Perpendicular Baseline (meters)
19960714	19920611	57
19970907	19920611	1
19950415	19920820	28
19970525	19920820	81
19970803	19920820	98
19960505	19930422	80
19980510	19930422	62
20000827	19930422	45
19960818	19930701	62
19970629	19930701	94
19970525	19950415	53
19970803	19950415	70
19970525	19950520	99
19970803	19950520	82
19960505	19960504	98
19990808	19960504	74
19990808	19960505	24
2000827	19960505	35
19970629	19960818	32
19970803	19970525	17
20000618	19970525	62
20000618	19970803	45
20000827	19990808	59

Table A9: Dry season InSAR pairs with perpendicular baseline ≤ 100 meters